

MULTIMESSENGER ASTRONOMY
AND TESTING GENERAL RELATIVITY WITH
GRAVITATIONAL WAVES

by

Naresh Adhikari

A Dissertation Submitted in
Partial Fulfillment of the
Requirements for the Degree of

Doctor of Philosophy
in Physics

at
The University of Wisconsin-Milwaukee
August 2024

ABSTRACT

MULTIMESSENGER ASTRONOMY AND TESTING GENERAL RELATIVITY WITH GRAVITATIONAL WAVES

by

Naresh Adhikari

The University of Wisconsin-Milwaukee, 2024
Under the Supervision of Professor Patrick Brady

The detection of gravitational waves (GW) from compact binary coalescence events has revolutionized our ability to study extreme gravity using neutron stars and stellar-mass black holes. This dissertation presents techniques to accelerate parameterized tests of general relativity and to understand astrophysical sources that generate both electromagnetic and gravitational-wave emission. First, I show how to use a multiband decomposition of the likelihood to test General Relativity in the strong-field regime. The multiband decomposition significantly reduces the computational cost of parameterized tests. Our method speeds up the analysis of binary neutron star signals by a factor of $\mathcal{O}(10)$ for a low-frequency cutoff of 20 Hz, verified through both simulated and real data. This approach improves the efficiency and feasibility of long-duration signal analysis, essential for probing the deviations from general relativity with gravitational waves measured by ground and space-based interferometric gravitational-wave detectors. Next, I present a Bayesian framework to jointly analyze gravitational-wave and electromagnetic triggers and report their significance for rapid follow-up observations. I use this framework to motivate the RAVEN software that is used by the LIGO-Virgo-KAGRA Collaboration to search multimessenger sources. I present tests and preliminary results from the first part of the fourth observing run (O4a). Finally, I demonstrate how joint inference of gravitational-wave and gamma-ray data breaks degeneracies between source parameters and allows improved understanding

of the progenitors. This work highlights the potential of combining gravitational-wave and electromagnetic observations to advance our understanding of the universe through astronomical observations.

© Copyright by Naresh Adhikari, 2024
All Rights Reserved

To my parents, my late grandmother,
my spouse, and my child.

TABLE OF CONTENTS

1	Introduction	1
1.0.1	General Relativity and its deviations	1
1.0.2	A brief history of multi-messenger sources	3
1.0.3	Organization of the dissertation	7
2	Tests of GR using gravitational waves	8
2.1	Basics	10
2.1.1	Parameterized tests of GR	11
2.1.2	Multiband decomposition	14
2.2	Extension to parameterized tests	16
2.2.1	Modified time to merger	16
2.2.2	Speed-up gains	19
2.3	Validation	20
2.3.1	Simulation study	20
2.3.2	Likelihood errors for GW190814	23
2.4	Conclusion	26
3	Searching for multi-messenger events with LIGO-Virgo-KAGRA	30
3.1	Basics	32
3.1.1	Elements of gravitational-wave detection	32
3.1.2	Elements of electromagnetic detection	34
3.1.3	Joint statistical method for analyzing gravitational-wave and electromagnetic data	37
3.1.3.1	Filtering of the data	40
3.1.3.2	Multimessenger triggers ranking in the high coincidence probability limit	42
3.2	The RAVEN pipeline	46
3.2.1	Pipeline description including recent improvements	48
3.2.2	Implementation for multiple EM detectors	53
3.2.3	Validation and testing using a Mock-Data-Challenge	54
3.3	Results from O4a	58
4	Combining GW and GRB afterglow observations	65
4.1	Joint inference basics	67
4.1.1	GW source model	68

4.1.2	GRB afterglow model	68
4.1.3	Joint likelihood	71
4.1.3.1	Relative binning likelihood technique	71
4.2	Simulation study	72
4.3	Results & Conclusions	76
5	Future Directions	80
5.1	Comprehensive O4 multi-messenger study with RAVEN	81
5.2	Forward modeling of gravitational-wave observations	81
	Bibliography	81
	Curriculum Vitae	92

LIST OF FIGURES

1.1	The waveform of the gravitational wave event GW150914 detected by LIGO. This plot shows the strain data from the detectors, displaying the characteristic chirp signal produced by the inspiral and merger of two black holes. The x-axis represents time, while the y-axis represents the strain amplitude. The data have been processed to highlight the signal amidst the noise. Credit: S. Perkins, reproduced with permission.	4
1.2	Schematic illustration of a gamma-ray burst engine. The central engine produces a jet of material that moves outward after the collision of neutron stars or a neutron star and a black hole. As faster shells of material collide with slower ones, low-energy gamma rays are emitted due to internal shock waves. When the jet collides with the surrounding medium, it generates an external shock wave, producing high-energy gamma rays, X-rays, visible light, and radio waves. The prompt emission phase involves the initial gamma-ray emission, while the afterglow phase encompasses multi-wavelength emission following the initial burst. Credit: NASA/Goddard Space Flight Center/ICRAR.	5
2.1	Time-domain gravitational waveforms of non-spinning $1.4M_{\odot}$ - $1.4M_{\odot}$ BNS starting from 20 Hz with various values of $\delta\hat{\varphi}_0$ (left) or $\delta\hat{\varphi}_{-2}$ (right). Vertical lines represent durations calculated by the up-to-0PN time-to-merger formula Eq. (2.21).	19
2.2	One- and two-dimensional marginal posterior distributions of chirp mass \mathcal{M} , mass ratio q , and 0PN relative deviation $\delta\hat{\varphi}_0$ from runs without (blue) and with (orange) the multiband decomposition technique. Diagonal panels show one-dimensional marginal posterior distributions, and vertical dashed lines indicate the 90% credible intervals. Off-diagonal panels show two-dimensional marginal posterior distributions, and solid lines indicate the 50% and 90% credible regions. Red lines indicate the injection values. . . .	23
2.3	One- and two-dimensional marginal posterior distributions of chirp mass \mathcal{M} , mass ratio q , and -1PN absolute deviation $\delta\hat{\varphi}_{-2}$ from runs without (blue) and with (orange) the multiband decomposition technique. Diagonal panels show one-dimensional marginal posterior distributions, and vertical dashed lines indicate the 90% credible intervals. Off-diagonal panels show two-dimensional marginal posterior distributions, and solid lines indicate the 50% and 90% credible regions. Red lines indicate the injection values. .	24

2.4	Log-likelihood errors $ \Delta \ln \mathcal{L} $ of the multiband approximation calculated on posterior samples from GW190814. The left plot shows the errors for tests of inspiral non-GR parameters and the right for tests of post-inspiral non-GR parameters. Each label shows the median value of these errors.	26
2.5	One- and two-dimensional marginal posterior distributions of all the inferred parameters for the 0PN simulation from runs without (blue) and with (orange) the multiband decomposition technique. Diagonal panels show one-dimensional marginal posterior distributions, and vertical dashed lines indicate the 90% credible intervals. Off-diagonal panels show two-dimensional marginal posterior distributions, and solid lines indicate the 50% and 90% credible regions. Red lines indicate the injection values.	28
2.6	One- and two-dimensional marginal posterior distributions of all the inferred parameters for the -1 PN simulation from runs without (blue) and with (orange) the multiband decomposition technique. Diagonal panels show one-dimensional marginal posterior distributions, and vertical dashed lines indicate the 90% credible intervals. Off-diagonal panels show two-dimensional marginal posterior distributions, and solid lines indicate the 50% and 90% credible regions. Red lines indicate the injection values.	29
3.1	Workflow of the Multi-Messenger Signals Detection and Alert System Used by the LIGO-Virgo-KAGRA Collaboration: Both the GW candidate and EM counterpart information are uploaded/ingested to the database, GraceDB. A few tasks are set up to listen and parse information every time a new detection is reported. This allows the RAVEN software to successfully query for neighbors correlating in time and skymap.	48
3.2	Current Implementation of the RAVEN Pipeline with Multiple GW and EM Searches. The flowchart illustrates various GW searches, including All-Sky, Early Warning, and Binary Black Hole GW candidates, as well as EM searches for significant and low-significance GRBs and neutrinos. As shown in the flowchart, the coincident workflow remains consistent once a coincidence is identified. However, specific details involving skymaps are not depicted here because, among multiple external coincidences with a GW Superevent , one event with improved skymap information may be preferred.	55
3.3	Sky distribution of simulated gravitational wave events from different types of compact binary coalescences: binary black hole (BBH) mergers, neutron star-black hole (NSBH) mergers, and binary neutron star (BNS) mergers. The map shows the positions of 50,000 simulated events uniformly distributed across the sky, with BBH events marked by black dots, NSBH events marked by blue dots, and BNS events marked by orange dots. Credit: S. Ghosh, reproduced with permission.	57
3.4	Representative GW candidate from O3 Replay MDC data testing for the RAVEN pipeline. The timeline shows various stages (T1 to T8) involved in the process for candidate S230328br. Each bar represents a different task. The x-axis represents time in seconds, highlighting the cumulative duration of each task after the GW Superevent creation.	58

3.5	Summary of O4a RAVEN Search Results. This bar chart shows the distribution of GW superevent counts across various search outcome categories and summarizes the EM follow-up efforts and results for GW candidates during the O4a observing run.	59
3.6	Scatter plot showing the ranking of significant GRBs detected in the O4a RAVEN search. The horizontal axis displays the false alarm rate for gravitational waves (FAR_{gw}), while the vertical axis shows the false alarm rate for coincident events (FAR_c) computed using spatio-temporal information as per Eq. (3.30). Blue markers represent GRBs vetoed by the EM instruments, and orange markers represent non-vetoed GRBs. GRB vetoing can happen due to classification and source location changes with the update notices or the satellite’s technical failures.	62
3.7	SubGRBTargeted Results displaying the relationship between FAR_{em} and FAR_{gw} . Blue and orange points represent positive and negative FAR_c values, respectively, with the Fermi-limit shown as a dashed line. FAR_c is calculated using Eq. (3.31), and negative FAR_c values can be completely disregarded. We used the highest GW FAR (10 per day) and the GRB FAR threshold (8.6 per day), aiding in evaluating potential correlations between low-significance GW and GRB events. We discovered that the highly significant GWs are associated with low-significance GRBs from a Fermi search pipeline that didn’t pass $\text{FAR}_{em,th}$	63
3.8	SubGRBTargeted Results: FAR Analysis (Zoomed). Green points mark the joint coincidences that consist of low-significance GRBs passing the Fermi-limit, as shown with the yellow dotted line and discussed in detail in Table 3.4. The magenta solid line represents a threshold using the max FAR_{gw} and FAR_{em} values as in Eq. (3.31). Both axes use a logarithmic scale. . . .	64
4.1	Simulated GRB afterglow lightcurve using the tophat model for a period of $\mathcal{O}(10^2)$ days.	73
4.2	Corner plot showing one- and two-dimensional marginal posterior distributions of selected inferred parameters (q , \mathcal{M} , $\theta_{observer}$, d_L , Λ_1 , Λ_2) for the GW simulation using the relative binning technique. Diagonal panels show one-dimensional marginal posterior distributions, with vertical dashed blue lines indicating the 90% credible intervals. Off-diagonal panels show two-dimensional marginal posterior distributions, with solid blue contours indicating the 50% and 90% credible regions. Orange lines indicate the injection values. Above each diagonal plot, the median value and 90% credible interval for each parameter are displayed numerically.	77

4.3	<p>Corner plots showing one- and two-dimensional marginal posterior distributions of selected inferred parameters (q, \mathcal{M}, $\theta_{observer}$, d_L, Λ_1, Λ_2) for the GW-GRB afterglow simulation from runs with the relative binning technique using only GW data (blue contours) and combined GW-GRB afterglow data (orange contours). Diagonal panels show one-dimensional marginal posterior distributions, with vertical dashed lines indicating the median and 90% credible intervals for both cases. Off-diagonal panels show two-dimensional marginal posterior distributions, with solid lines indicating the 50% and 90% credible regions. Red lines or points indicate the true (injection) values of the parameters.</p>	78
4.4	<p>Corner plot showing one- and two-dimensional marginal posterior distributions of all inferred parameters for the GW-GRB afterglow simulation analyzed with the relative binning technique using combined GW and GRB data. Diagonal panels show one-dimensional marginal posterior distributions, with vertical dashed lines indicating the 90% credible intervals. Off-diagonal panels show two-dimensional marginal posterior distributions, with solid contours indicating the 50% and 90% credible regions. Orange lines indicate the injection values. For q and \mathcal{M}, orange lines are not shown since the simulations were performed using the values of the primary and secondary masses. Parameter labels are shown on the axes.</p>	79

LIST OF TABLES

1.1	Summary of supernova types and their progenitor masses and characteristics. (Maggiore, 2018; Graur, 2022)	6
2.1	The numbers of original frequency points K_{orig} , the numbers of multi-banded frequency points K_{MB} , and speed-up gains $K_{\text{orig}}/K_{\text{MB}}$ for a $1.4M_{\odot}$ – $1.4M_{\odot}$ BNS signal with several choices of data duration T and a non-GR parameter value $\delta\hat{\varphi}_i$ used for calculating time to merger. The total frequency range is 20–2048 Hz, and divided into frequency bands with $\{T^{(b)}\}_{b=0}^{B-1} = \{T, T/2, T/4, \dots, 4\text{s}\}$	20
2.2	The injection values, prior, and explored range of GR parameters: Chirp mass \mathcal{M} , mass ratio $q \leq 1$, luminosity distance D_L , right ascension RA and declination DEC, orbital inclination angle θ_{JN} , polarization angle ψ , constant phase ϕ_c , and coalescence time t_c . The prior uniform in cosine, sine, and comoving volume are denoted by “Cosine”, “Sine” and “Comoving” respectively. $t_{c,\text{inj}}$ denotes the injection value of t_c , and is set to the GPS time of 1187008882 (17 Aug 2017, 12:41:04 UTC).	21
3.1	The current implementation of the low-latency multi-messenger search pipeline uses coincident time windows, measured in seconds, chosen based on the search and pipeline parameters, and centered on the GW merger/burst time.	53
3.2	The component masses (m) and spins (a) distribution of binary systems were used in the injection sample for the O3 Replay MDC (Chaudhary et al., 2024). However, the LVK collaboration performs searches in higher mass ranges, up to $3 M_{\odot}$ for neutron stars (Ewing et al., 2024).	56
3.3	Summary of O4a Significant GRB Coincidences. Here, FAR_c is computed using spatio-temporal information as defined in Eq. (3.30) and has a unit of Hz. A time window of $\Delta t = 660$ seconds is used, and a GRB rate (R_{grb}) of 310 per year is assumed. “Alert threshold not met” signifies that these joint coincidences didn’t pass a threshold of 1 per year, i.e., 3.17×10^{-8} Hz.	62

3.4	Summary of O4a Low-Significant GRB Coincidences. Here, FAR_c is computed using spatio-temporal information as defined in Eq. (3.31) and has a unit of Hz. A time window of $\Delta t = 12$ seconds is used for Fermi and 30 seconds for Swift in processing low-significance GRBs. “Alert threshold not met” signifies that these joint coincidences did not pass a threshold of 1 per year, i.e., 3.17×10^{-8} Hz for Burst. <code>RAVEN_ALERT</code> for joint coincidences where the GW belongs to the CBC searches did not pass a threshold of 1 per month, i.e., 3.86×10^{-7} Hz.	63
4.1	Probes and Techniques for GRB Afterglow Emission with X-ray and Radio Wavelengths (Carroll & Ostlie, 2017; Rhodes et al., 2020; Ronchini et al., 2022; Gianfagna et al., 2023).	70
4.2	The injection and prior values for each parameter of the EM and GW signals are listed below. θ_{observer} and θ_{JN} are related and are treated as a single parameter.	75

ACKNOWLEDGEMENTS

I would like to express my deepest gratitude to my advisor, Professor Patrick Brady, for his invaluable guidance, advice, and the numerous opportunities he has provided. I am also grateful to my committee members, Professors Alan Wiseman, David Kaplan, Jolien Creighton, and John Friedman, for dedicating their invaluable time to guiding me and for their suggestions. I have taken a few courses with each professor and learned a great deal.

I am highly indebted for the travel and research funding support provided to attend various conferences, which gave me a platform to discuss ideas and meet collaborators within the LVK Collaboration. I am also indebted to the UWM Graduate School for providing the Chancellor's Student Success Fund during the time of uncertainty and the travel fund. I am thankful to the UWM Library services and personnel and also to the Interlibrary Loan service.

I am grateful to Soichiro Morisaki, Brandon Piotrkowski, Kendall Ackley, V. Gayathri, and Nikhil Sarin, with whom I had extended discussions on the problems I have solved during the undertaking of this dissertation. Together, we have produced scientific results and published a paper or are in the manuscript stage. Additionally, I received advice on navigating graduate school and exploring post-graduation career options.

I am thankful to the physics department and CGCA's administrative support, and to Professors Daniel Agterberg, Dawn Erb, and Philip Chang for the rigorous graduate and elective course curriculum. I am grateful for the supervision during my TA duties, especially to Dr. Joseph O'Halloran, Dr. Debashis Dasgupta, and Mr. James Maillis. I am highly indebted to my colleagues who joined the graduate program with me in the fall of 2019, providing support in discussing problem sets and spending time together.

In addition, I acknowledge the support I received to attend the EMIT School at Vanderbilt University, where I participated in the program on multi-messenger astronomy for two weeks, along with personal and professional development discourses. I am thankful to the organizers and the friends I met there.

I am very thankful to the late Professor Lewis P. Fulcher at Bowling Green State University for his support and guidance during my graduate studies, for allowing me to undertake graduate-level analysis and algebra courses in the mathematics department with financial support from the physics department, and for his effective teaching of graduate-level electrodynamics. I am also thankful to Professor Farida Selim, who believed in me, always listened to me, and allowed me to work on research with freedom. I want to express my gratitude to Professors Alexey Zayak and Haowen Xi for their approach to teaching physics pedagogy.

The desire to gain a deeper understanding of the workings of nature was enhanced during my studies at the Central Department of Physics, Tribhuvan University. I would like to thank Professor Binil Aryal, the department chair, and Professor Narayan Prasad Adhikari for their encouragement in emphasizing critical thinking. I also thank Professor Udayaraj Khanal, my master's thesis advisor, who introduced me to the beauty of mathematical physics and the theory of general relativity. My fellow colleagues and I often conversed with Udaya Sir on topics related to theoretical physics. He always responded to our queries with enthusiasm and inspired us.

I am very fortunate to be able to dedicate most of my time to undertaking 13 graduate-level courses, mostly in theoretical physics, and a few research projects during my graduate studies, thanks to the support of my spouse, Radhika. Also, many thanks to my son, Advait, who inspired me to look at everything from a fresh perspective.

I dedicate this work to my parents, family, friends, and the giants whose work inspired me.

Last, but not least, I felt humbled while watching and listening to the ripples on the shore of Lake Michigan and contemplating my research on gravitational waves. These quiet moments of reflection often provided insights into my work.

Young man, in mathematics you don't understand things.
You just get used to them.

John von Neumann's reply to a physicist friend.

प्राप्तिभन्दा ध्येय ठूलो हो, पुग्नुभन्दा आशा र खोज महत्वपूर्ण हो ।
(The goal is greater than the achievement, hope and
exploration are more important than reaching the
destination.)

नेपाली महाकवि लक्ष्मीप्रसाद देवकोटा

(Nepali "Great Poet" Laxmi Prasad Devkota)

To ask a question is not to find an answer, but to discover
and find out for oneself.

Jiddu Krishnamurti

Chapter 1

Introduction

1.0.1 General Relativity and its deviations

Einstein's field equations ([Einstein, 1915](#)), formulated in 1915, describe how spacetime responds to mass and energy, explaining the fundamental interaction of gravitation. The equations are expressed as:

$$\mathcal{G}_{\mu\nu} = \frac{8\pi G}{c^4} \mathcal{T}_{\mu\nu}, \quad (1.1)$$

where

$$\mathcal{G}_{\mu\nu} = \mathcal{R}_{\mu\nu} - \frac{1}{2} g_{\mu\nu} \mathcal{R}, \quad (1.2)$$

is the Einstein tensor that incorporates information how spacetime is curved via the Ricci tensor $\mathcal{R}_{\mu\nu}$. Here, G is Newton's gravitational constant, c is the speed of light, and $\mathcal{T}_{\mu\nu}$ is the stress-energy tensor ([Misner et al., 1973](#)). The linear, weak-field approximation ([Einstein, 1916](#)) is obtained from Eq. (1.1) by perturbing around Minkowski spacetime $g_{\mu\nu} = \eta_{\mu\nu} + h_{\mu\nu}$ and can be written in the Lorenz gauge as

$$\square \bar{h}_{\mu\nu} = -\frac{16\pi G}{c^4} \mathcal{T}_{\mu\nu}. \quad (1.3)$$

Here $\square = -\frac{1}{c^2} \frac{\partial^2}{\partial t^2} + \nabla^2$ is the d'Alembertian operator, and $\bar{h}_{\mu\nu}$ is the trace-reversed metric perturbation

$$\bar{h}_{\mu\nu} = h_{\mu\nu} - \frac{1}{2} \eta_{\mu\nu} h, \quad (1.4)$$

with $h_{\mu\nu}$ being the metric perturbation, $\eta_{\mu\nu}$ the Minkowski metric, and $h = \eta^{\mu\nu} h_{\mu\nu}$ the trace of $h_{\mu\nu}$. The Lorenz gauge condition is given by:

$$\partial^\mu \bar{h}_{\mu\nu} = 0. \quad (1.5)$$

In general relativity (GR), gravitational waves have two independent polarization modes, commonly referred to as “plus” (+) and “cross” (×) polarizations. These modes are transverse and traceless (Schutz, 2022). The radiative solution (Einstein, 1918) of Eq. (1.3) in the transverse-traceless (TT) gauge is given by:

$$h_{ij}^{TT}(t, \mathbf{x}) = \frac{4G}{c^4} \frac{1}{r} \int d^3x' \Lambda_{ij,kl}(\mathbf{n}) \mathcal{T}_{kl}(t - r/c, \mathbf{x}'). \quad (1.6)$$

$\Lambda_{ij,kl}(\mathbf{n})$ is the TT projection operator. In the context of gravitational waves, for weak fields and slow-moving sources (Maggiore, 2007), the leading-order solution to Eq. (1.6) is given by the quadrupole formula

$$h_{ij}^{TT}(t, \mathbf{x}) = \frac{2G}{c^4 r} \ddot{Q}_{ij}^{TT}(t - r/c), \quad (1.7)$$

where h_{ij}^{TT} is the spatial part of the metric perturbation in the TT gauge, r is the distance from the source to the observer, $Q_{ij}^{TT}(t - r/c)$ is the transverse-traceless quadrupole moment tensor of the source evaluated at the retarded time, and \ddot{Q}_{ij}^{TT} represents its second time derivative. This solution is valid in the far-field, where the distance to the observer is much larger than the size of the source and the wavelength of the gravitational radiation.

The general-relativistic equations of motion of the source can be similarly expanded in the weak-field, slow-motion approximation. By accounting for the back-action of the

radiated waves on the source, assuming only gravitational interactions are important, one finds the motion of the matter imprints a specific functional form on the gravitational waves within general relativity.

Deviations from general relativity

Local Motion in the Near-Field Zone: In the near-field zone of a compact object, where gravity is strong, non-linear, and non-Newtonian, any deviations from GR are enhanced. Such deviations modify the equations of motion, and hence the gravitational waveform, and can be probed during the dynamical evolution of compact objects such as neutron stars and black holes (Blanchet, 2014). Figure 1.1 shows the detected gravitational waveform of the binary-black-hole merger GW150914 along with the fitting of the waveform from numerical relativity.

Power Radiated: The power radiated by gravitational waves at leading order in GR is given by the quadrupole formula. Any deviations from this prediction would imply modifications to gravity or the presence of additional fields (Will, 2014). Such effects would also be imprinted on the gravitational waveform and can be quantified using the parameterized post-Newtonian framework or similar parameterizations of deviations from GR (Yunes & Pretorius, 2009; Abbott et al., 2019b,a). These parameterizations allow for systematic tests of GR using gravitational wave observations, potentially revealing new physics beyond Einstein’s theory.

1.0.2 A brief history of multi-messenger sources

The first multi-messenger extrasolar system astronomical transient was the supernova SN 1987A, which was detected via its optical light on 24 February 1987. Neutrinos produced in the core-collapse of the stellar progenitor were also observed. They were identified retrospectively in three different neutrino detectors, having arrived the day before the supernova

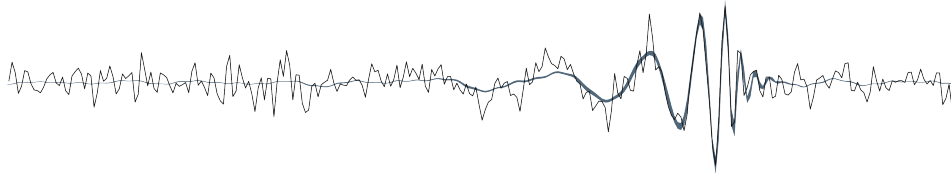


Figure 1.1: The waveform of the gravitational wave event GW150914 detected by LIGO. This plot shows the strain data from the detectors, displaying the characteristic chirp signal produced by the inspiral and merger of two black holes. The x-axis represents time, while the y-axis represents the strain amplitude. The data have been processed to highlight the signal amidst the noise. Credit: S. Perkins, reproduced with permission.

was identified optically. This source provided the most detailed observations of a supernova explosion ever recorded. Observations validated our understanding of supernovae as the end stage of massive stellar evolution. Based on the properties of the progenitor star and the supernova explosion, SN 1987A is also thought to have left behind a neutron star. The most massive stars are expected to produce black holes at the end of their lifetimes when they run out of nuclear fuel.

Most stars are in binary systems. While the detailed evolution of the individual stars may be modified by the presence of their companions, these binary star systems may eventually evolve to binary systems containing neutron stars and/or black holes (Mapelli, 2020; Tauris & van den Heuvel, 2023).

Mergers of compact binaries involving neutron stars and stellar-mass black holes are strong sources of gravitational waves in the frequency band relevant to ground-based, interferometric detectors. The components of these binaries are sufficiently compact that they can orbit each other closely. These binaries tighten as they lose their orbital energy and angular momentum through gravitational-wave emission. This loss of energy intensifies as their separation decreases, and the compact objects coalesce in a finite time. These mergers may also produce electromagnetic radiation by the following scenarios:

- (i) Binary neutron stars collide with very high velocity, producing ejecta traveling at

speeds of thousands of kilometers per second and resulting in the remnant system's accretion of neutron-rich material.

- (ii) In a neutron star-black hole system with low black-hole mass, the black hole tidally disrupts the neutron star, causing baryonic matter to be funneled along the orbital angular momentum axis of the binary (Ruiz et al., 2018).

Both of these scenarios produce signals in gravitational waves and electromagnetic waves across the electromagnetic spectrum, as depicted in Figure 1.2.

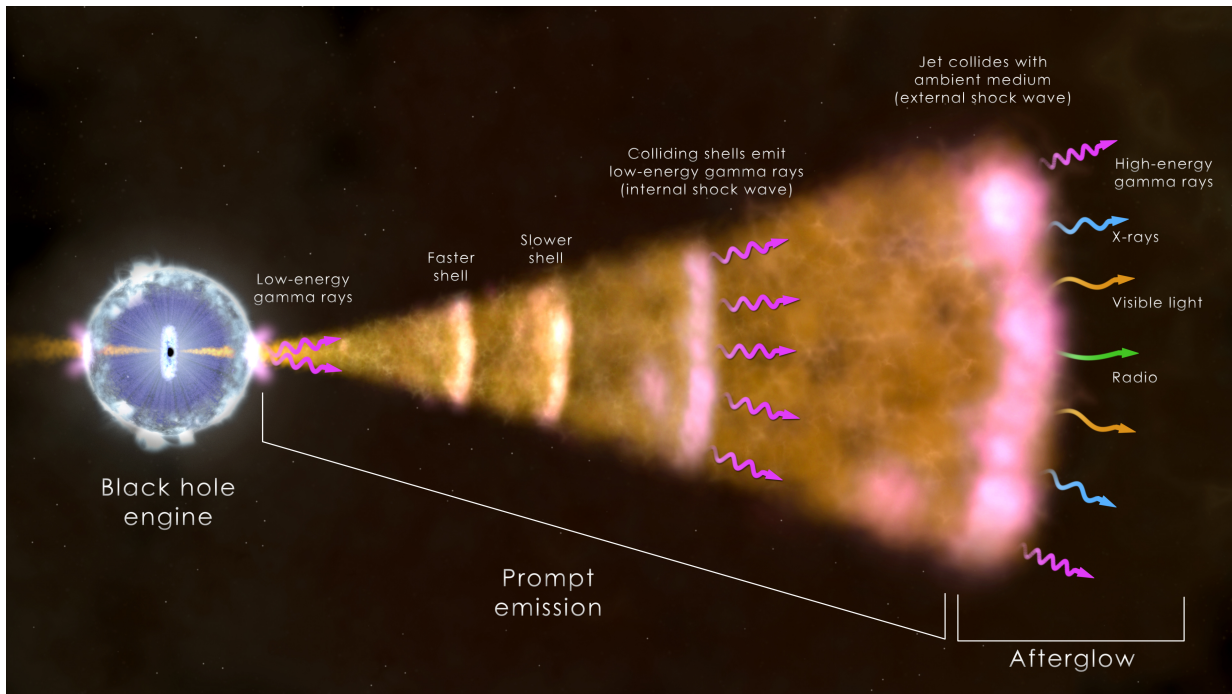


Figure 1.2: Schematic illustration of a gamma-ray burst engine. The central engine produces a jet of material that moves outward after the collision of neutron stars or a neutron star and a black hole. As faster shells of material collide with slower ones, low-energy gamma rays are emitted due to internal shock waves. When the jet collides with the surrounding medium, it generates an external shock wave, producing high-energy gamma rays, X-rays, visible light, and radio waves. The prompt emission phase involves the initial gamma-ray emission, while the afterglow phase encompasses multi-wavelength emission following the initial burst. Credit: NASA/Goddard Space Flight Center/ICRAR.

The formation process of singular neutron stars or black holes occurs through the evolution of single high-mass stars with a mass of $\geq 8M_{\odot}$. Such massive stars burn their

nuclear fuel much more rapidly than lower-mass stars, leading to faster evolution and shorter lifespans. As they exhaust their fuel, they undergo a series of nuclear fusion stages, eventually developing an iron core.

When the core reaches the Chandrasekhar limit, it collapses, triggering a supernova explosion that produces multi-messenger signals, including neutrinos, gravitational waves, and electromagnetic waves¹. The fate of the stellar remnant depends on the initial mass of the star. Stars with initial masses between about 8 and 20 M_{\odot} typically form neutron stars. Stars with initial masses above about 20 M_{\odot} generally form black holes, either directly or through fallback accretion after the supernova (Timmes et al., 1995; Schaffner-Bielich, 2020). Supernova characteristics by mass range are summarized in Table 1.1.

Supernova Type	Progenitor Mass (M_{\odot})	Progenitor Characteristics
Ia	$\sim 1-8$	Thermonuclear explosion of a white dwarf in a binary system
Ib	> 8	Massive star, hydrogen envelope lost
Ic	> 8	Massive star, hydrogen and helium envelopes lost
Ic-BL	> 30	Very massive star, associated with GRBs, broad lines associated with very high ejecta velocities
II-P	$\sim 8-25$	Massive red supergiant, extended hydrogen envelope, plateau in light curve after a few months
II-L	$\sim 8-25$	Massive star, less extended hydrogen envelope, linear light curve emission dissipation
II _n	$\sim 8-25$	Massive star, dense circumstellar material, narrow lines in spectrum
II _b	$\sim 8-25$	Massive star, partially lost hydrogen envelope

Table 1.1: Summary of supernova types and their progenitor masses and characteristics. (Maggiore, 2018; Graur, 2022)

Many physical processes can enhance the formation channels of such binary systems. Recently, the effects of binary source parameters (Rosswog et al., 2024; Karakas et al.,

¹See <https://www.youtube.com/watch?v=Yt-SBT7nNfU> and references within.

2024), interstellar medium (Ghodla, 2024), and astrophysical backgrounds (Dhurkunde & Nitz, 2023) have been explored.

1.0.3 Organization of the dissertation

This dissertation is organized as follows: In Chapter 2, I present a technique to test for deviations in the phase evolution of binary-neutron-star waveforms that could arise in alternate theories of gravity. I demonstrate the robustness of the proposed algorithm using both simulated and real data. In Chapter 3, I outline a method for ranking triggers that are observed in both gravitational waves and gamma rays, assuming binary star mergers produce both, using a Bayesian technique. I use this to motivate the currently implemented frequentist technique for ranking multi-messenger signals employed by the LIGO-Virgo-KAGRA (LVK) Collaboration. I present tests of the implemented framework and provide preliminary results from the first part of the LVK Collaboration’s fourth observing run. In Chapter 4, I outline the technique I contributed to the Redback software package for performing joint inference of simulated gravitational wave (GW) and gamma-ray burst (GRB) afterglow signals, using a rapid likelihood approach. Finally, in Chapter 5, I describe the conclusions of this dissertation and possible future research directions.

Chapter 2

Tests of GR using gravitational waves

This chapter is reproduced from [Adhikari & Morisaki \(2022\)](#), which has been published in Physical Review D. An online record can be found at <https://doi.org/10.1103/PhysRevD.106.104053>.

The gravitational-wave era started with the discovery of the gravitational wave signal from the binary black hole merger, GW150914 ([Abbott et al., 2016a](#)), by the advanced LIGO detectors ([Aasi et al., 2015](#); [Buikema et al., 2020](#); [Tse et al., 2019](#)). The binary neutron star (BNS) signal, GW170817 ([Abbott et al., 2017c](#)), was observed two years later by the advanced LIGO and advanced Virgo ([Acernese et al., 2015, 2019](#)) detectors. It became the first example of multi-messenger observations involving gravitational waves ([Abbott et al., 2017d,b](#)). Recently, the first-ever observations of mergers of two distinct compact objects, i.e., a neutron star and a black hole, were also achieved ([Abbott et al., 2021b](#)), completing the search for a gravitational-wave signal originating from all three distinct classes of compact mergers. The detected CBC signals enabled us to test General Relativity (GR) in the strong-field regime. Various tests have been proposed and applied to the detected signals by the LIGO–Virgo–KAGRA Collaboration (LVK) ([Abbott et al.,](#)

2016b, 2019b,c, 2021c,d) and others (Isi et al., 2019; Takeda et al., 2021; Shoom et al., 2023).

Among various tests performed by LVK are the parameterized tests (Arun et al., 2006; Li et al., 2012; Mishra et al., 2010; Agathos et al., 2014). In the parameterized tests, parameterized non-GR modifications are introduced to GR waveforms, and the parameters governing the modifications are constrained. The non-GR parameters consist of inspiral parameters and post-inspiral parameters. The inspiral parameters parameterize relative or absolute shifts of the inspiral post-Newtonian coefficients, while the post-inspiral parameters parameterize relative shifts of the post-inspiral phenomenological parameters. For informative constraints to be obtained efficiently, typically only one of those non-GR parameters is allowed to deviate and constrained in a single analysis (Sampson et al., 2013; Abbott et al., 2016b). Such a single-parameter test is known to be robust to ignorance of higher-order corrections (Perkins & Yunes, 2022). Recent works (Shoom et al., 2023; Saleem et al., 2022) also showed that multiple parameters can be investigated simultaneously using principal component analysis. Those parameterized modifications can incorporate modifications predicted by various alternative theories of gravity, and we can map those constraints to filter such non-GR theories as a post-processing step (Yunes et al., 2016).

The parameterized tests typically employ stochastic sampling and require more than millions of likelihood evaluations. Each likelihood evaluation requires the evaluations of waveform values at all the frequency points considered, which is the dominant cost. Since the frequency points are sampled with an interval of $1/T$, where T is the duration of data, more waveform evaluations are required for a longer signal. For a $1.4M_{\odot}$ – $1.4M_{\odot}$ BNS signal, current analyses take weeks–years without any approximate methods. This is going to be a serious problem when the sensitivities of detectors are improved and BNS signals are detected more frequently. The same problem arises for parameter estimation analyses of CBCs assuming GR, and various techniques have been proposed to reduce

the computational cost of waveform generation (Canizares et al., 2015; Smith et al., 2016; Morisaki & Raymond, 2020; Vinciguerra et al., 2017; Morisaki, 2021; Zackay et al., 2018; Cornish, 2021).

Among the various rapid parameter estimation techniques, a recent work considers a multiband decomposition of the gravitational-wave likelihood (Morisaki, 2021), which exploits the chirping nature of the CBC signals and speeds up the parameter estimation of a BNS signal by more than an order of magnitude. Since the signal frequency increases with time, the time to merger, $\tau(f)$, decreases with frequency f . This implies that the likelihood can be approximated into a form that can be computed with waveform values at frequency points sampled with a variable interval proportional to $1/\tau(f)$. This approximation drastically reduces the number of waveform evaluations at high frequency. A similar idea has been utilized for speeding up the matched-filter analysis for detection of CBC signals (Marion, 2003; Buskulic, 2010; Cannon et al., 2012).

In this paper, we apply the multiband decomposition technique to parameterized tests of GR. In Sec. 2.1, we briefly explain parameterized tests of GR and the multiband decomposition method for a GR signal. To extend the multiband decomposition method to parameterized tests, we need to consider modifications of $\tau(f)$ caused by non-GR modifications in waveforms. In Sec. 2.2, we derive the modified $\tau(f)$ and investigate the speed-up gains of our technique for a BNS signal. In Sec. 2.3 we study the accuracy of our technique using simulated BNS signals and real data. Finally, we conclude our work in Sec. 2.4.

2.1 Basics

In this section, we explain the parameterized tests of GR and the multiband decomposition technique for rapid parameter estimation.

2.1.1 Parameterized tests of GR

The dominant quadrupole moment of gravitational waves is of the following form in the frequency domain,

$$\tilde{h}(f) = A(f)e^{i\Phi(f)}, \quad (2.1)$$

where $A(f)$ and $\Phi(f)$ denote signal amplitude and phase respectively. The phase evolution of the early-inspiral part is calculated via the Post-Newtonian (PN) expansion (Will, 2011; Blanchet, 2014), which is an expansion with respect to a small orbital velocity v/c . A term with the order of $\mathcal{O}((v/c)^n)$ relative to the leading order is referred to as $(n/2)$ PN. In GR, the phase up to the 3.5PN order is given by (Buonanno et al., 2009; Sathyaprakash & Dhurandhar, 1991; Blanchet & Sathyaprakash, 1995),

$$\begin{aligned} \Phi^{\text{GR}}(f) = \\ 2\pi f t_c - \phi_c - \frac{\pi}{4} + \sum_{j=0}^7 \left[\varphi_j^{\text{GR}} + \varphi_j^{\text{GR}(l)} \ln f \right] f^{(j-5)/3}, \end{aligned} \quad (2.2)$$

where t_c and ϕ_c denote the coalescence time and phase respectively, and φ_j^{GR} and $\varphi_j^{\text{GR}(l)}$ are $(j/2)$ PN coefficients depending on component masses m_1, m_2 and spins \vec{S}_1, \vec{S}_2 . φ_j^{GR} is vanishing for $j = 1$ and $\varphi_j^{\text{GR}(l)}$ is vanishing except for $j = 5, 6$.

In the parameterized tests, parameterized deformations of non-zero PN coefficients are introduced by (Arun et al., 2006; Li et al., 2012; Mishra et al., 2010; Agathos et al., 2014),

$$\varphi_j^{\text{GR}} \rightarrow [1 + \delta\hat{\varphi}_j] \varphi_j^{\text{GR}}, \quad \varphi_j^{\text{GR}(l)} \rightarrow [1 + \delta\hat{\varphi}_j^{(l)}] \varphi_j^{\text{GR}(l)},$$

where $\delta\hat{\varphi}_j$ and $\delta\hat{\varphi}_j^{(l)}$ are non-GR parameters quantifying relative shifts of GR inspiral phasing. In addition to the relative shifts, absolute shifts are introduced to the -1 PN,

$$\varphi_{-2} f^{-7/3} = \frac{3\delta\hat{\varphi}_{-2}}{128} \eta^{2/5} \left(\frac{\pi G M f}{c^3} \right)^{-7/3}, \quad (2.3)$$

and 0.5PN,

$$\varphi_1 f^{-4/3} = \frac{3\delta\hat{\varphi}_1}{128\eta^{1/5}} \left(\frac{\pi G \mathcal{M} f}{c^3} \right)^{-4/3}, \quad (2.4)$$

where \mathcal{M} and η are chirp mass and symmetric mass ratio respectively,

$$\mathcal{M} = \frac{(m_1 m_2)^{3/5}}{(m_1 + m_2)^{1/5}}, \quad \eta = \frac{m_1 m_2}{(m_1 + m_2)^2}. \quad (2.5)$$

The -1 PN term is to model gravitational dipole radiation predicted by alternative theories of gravity (Eardley, 1975). The full list of inspiral non-GR parameters is,

$$\{\delta\hat{\varphi}_{-2}, \delta\hat{\varphi}_0, \delta\hat{\varphi}_1, \delta\hat{\varphi}_2, \delta\hat{\varphi}_3, \delta\hat{\varphi}_4, \delta\hat{\varphi}_5^{(l)}, \delta\hat{\varphi}_6, \delta\hat{\varphi}_6^{(l)}, \delta\hat{\varphi}_7\}.$$

The 2.5PN parameter $\delta\hat{\varphi}_5$ is not included since it is completely degenerate with ϕ_c .

In addition to the deformations of inspiral phase, parameterized deformations of post-inspiral phase are also considered. The IMRPhenom waveform model (Ajith et al., 2008; Husa et al., 2016; Khan et al., 2016) employs phase ansatz parameterized by β_i ($i = 0, 1, 2, 3$) for intermediate stage and by α_i ($i = 0, 1, 2, 3, 4$) for merger-ringdown stage. Relative shifts to those parameters are introduced in a similar way, which are parameterized by $\delta\hat{\beta}_i$ and $\delta\hat{\alpha}_i$. The full list of post-inspiral non-GR parameters as considered in (Abbott et al., 2016b, 2019c, 2021c,d) is,

$$\{\delta\hat{\alpha}_2, \delta\hat{\alpha}_3, \delta\hat{\alpha}_4, \delta\hat{\beta}_2, \delta\hat{\beta}_3\}.$$

For meaningful constraints to be obtained efficiently, typically only one of those 15 non-GR parameter is allowed to deviate and constrained in a single analysis. Parameterized deformations of amplitude can also be considered, but they are difficult to be measured with the current generation of detectors (Van Den Broeck & Sengupta, 2007b,a; O’Shaughnessy et al., 2014).

The non-GR parameters are estimated or constrained via Bayesian inference. In the

Bayesian inference, posterior distribution $p(\boldsymbol{\theta}|\{\mathbf{d}_i\})$ is calculated via the Bayes theorem:

$$p(\boldsymbol{\theta}|\{\mathbf{d}_i\}) \propto \mathcal{L}(\{\mathbf{d}_i\}|\boldsymbol{\theta}) \pi(\boldsymbol{\theta}), \quad (2.6)$$

where \mathbf{d}_i denotes the data taken from the i -th detector, $\boldsymbol{\theta}$ the set of model parameters consisting of one of the non-GR parameters and GR parameters, $\pi(\boldsymbol{\theta})$ the prior distribution function determined from our belief or prior knowledge on $\boldsymbol{\theta}$, and $\mathcal{L}(\mathbf{d}|\boldsymbol{\theta})$ the likelihood function. For the likelihood, the Gaussian-noise likelihood function is typically used (Thrane & Talbot, 2019; Christensen & Meyer, 2022),

$$\mathcal{L}(\{\mathbf{d}_i\}|\boldsymbol{\theta}) \propto \exp \left[-\frac{1}{2} \sum_i \|\mathbf{d}_i - \mathbf{h}_i(\boldsymbol{\theta})\|_i^2 \right], \quad (2.7)$$

where \mathbf{h}_i is a model signal observed at the i -th detector. $\|\cdot\|^2 = (\cdot, \cdot)$ is the norm induced by the inner product,

$$(\mathbf{a}, \mathbf{b})_i = \frac{4}{T} \Re \left[\sum_{k=f_{\text{low}}T}^{f_{\text{high}}T} \frac{\tilde{a}^*(f_k) \tilde{b}(f_k)}{S_i(f_k)} \right], \quad (2.8)$$

where f_{low} and f_{high} are the low- and high-frequency cutoffs of the analysis respectively, T is the duration of data, $S_i(f)$ is the noise power spectral density of the i -th detector, and $f_k \equiv k/T$ is the k th frequency bin. The logarithm of likelihood can be written as

$$\begin{aligned} \ln \mathcal{L}(\mathbf{d}|\boldsymbol{\theta}) &= \sum_i \left[(\mathbf{d}_i, \mathbf{h}_i(\boldsymbol{\theta}))_i - \frac{1}{2} (\mathbf{h}_i(\boldsymbol{\theta}), \mathbf{h}_i(\boldsymbol{\theta}))_i \right] \\ &+ \text{const.}, \end{aligned} \quad (2.9)$$

where the constant part does not depend on $\boldsymbol{\theta}$ and is irrelevant for stochastic sampling.

The inference is typically done via stochastic sampling methods, such as Markov-Chain Monte Carlo (MCMC) (Metropolis et al., 1953; Hastings, 1970) and nested sampling (Skilling, 2006). The non-constant term is computed millions of times during stochastic sampling. As is evident from Eq. (2.9) and Eq. (2.8), each likelihood evaluation requires

evaluations of waveform values at all the frequency points from f_{low} to f_{high} . Those waveform evaluations are typically the dominant cost of analysis. The cost is proportional to the number of frequency points,

$$K_{\text{orig}} = (f_{\text{high}} - f_{\text{low}})T + 1, \quad (2.10)$$

and higher for a longer signal.

2.1.2 Multiband decomposition

In the multiband decomposition method, the total frequency range is divided into B overlapping frequency bands $f_s^{(b)} \leq f \leq f_e^{(b)}$ ($b = 0, 1, \dots, B - 1$). The start and end frequencies are determined based on a user-specified sequence of durations, $T = T^{(0)} > T^{(1)} > \dots > T^{(B-1)}$. First, the following equation is solved with respect to $f^{(b)}$ for each $b \in \{1, 2, \dots, B - 1\}$,

$$\tau(f^{(b)}) + L\sqrt{-\tau'(f^{(b)})} = T^{(b)} + t_{c,\text{min}} - T, \quad (2.11)$$

where $\tau(f)$ is a reference time-to-merger from a gravitational wave frequency f . L is a user-specified constant controlling the accuracy of the approximation. A larger value of L gives more accurate likelihood values. $t_{c,\text{min}}$ is the minimum coalescence time in the prior range. $L = 5$ and $T - t_{c,\text{min}} = 2.12$ s are used throughout this paper, following (Morisaki, 2021). The start and end frequencies are determined as

$$f_s^{(b)} = \begin{cases} f_{\text{low}}, & (b = 0) \\ f^{(b)} - \frac{1}{\sqrt{\tau'(f^{(b)})}}, & (b > 0) \end{cases} \quad (2.12)$$

$$f_e^{(b)} = \begin{cases} f^{(b+1)}, & (b < B - 1) \\ f_{\text{high}} + \Delta f_{\text{high}}, & (b = B - 1) \end{cases} \quad (2.13)$$

This way of constructing frequency bands guarantees that the inverse Fourier transform of $\tilde{h}(f)$ starting from $f_s^{(b)}$ has a duration shorter than $T^{(b)}$. $\Delta f_{\text{high}} > 0$ is required to avoid the loss of accuracy caused by the abrupt termination of a waveform.

With the frequency bands constructed, $(\mathbf{d}_i, \mathbf{h}_i(\boldsymbol{\theta}))_i$ is approximated into the following form,

$$(\mathbf{d}_i, \mathbf{h}_i(\boldsymbol{\theta}))_i \simeq \sum_{b=0}^{B-1} \frac{4}{T^{(b)}} \Re \left[\sum_{k=\lfloor f_s^{(b)} T^{(b)} \rfloor}^{\lfloor f_e^{(b)} T^{(b)} \rfloor} w^{(b)}(f_k^{(b)}) \tilde{D}_{i,k}^{(b)*} \tilde{h}_i(f_k^{(b)}; \boldsymbol{\theta}) \right], \quad (2.14)$$

where $w^{(b)}(f)$ is a smooth window function extracting waveform values in the b -th frequency band, $\tilde{D}_{i,k}^{(b)}$ is a quantity calculated from data and power spectral density, and

$$f_k^{(b)} \equiv \frac{k}{T^{(b)}}. \quad (2.15)$$

The sum over a high-frequency band requires waveform values only at downsampled frequencies whose interval is $1/T^{(b)}$, and hence fewer waveform evaluations. The number of waveform evaluations required for a single evaluation of $(\mathbf{d}_i, \mathbf{h}_i(\boldsymbol{\theta}))_i$ is reduced to

$$K_{\text{MB}} = \sum_{b=0}^{B-1} (\lfloor f_e^{(b)} T^{(b)} \rfloor - \lfloor f_s^{(b)} T^{(b)} \rfloor + 1). \quad (2.16)$$

There were two approximate methods proposed to compute $(\mathbf{h}_i(\boldsymbol{\theta}), \mathbf{h}_i(\boldsymbol{\theta}))_i$ with fewer waveform evaluations. One method is referred to as *Linear Interpolation*, which approximates $|\tilde{h}_i(f; \boldsymbol{\theta})|^2$ as a linear interpolation of the squares of downsampled waveform values. This works well if the waveform model contains only dominant quadrupole moments, where $|\tilde{h}_i(f; \boldsymbol{\theta})|^2$ is a smooth function. The other method is referred to as *IFFT-FFT*, which works even if the waveform model contains multiple moments. In either case, $(\mathbf{h}_i(\boldsymbol{\theta}), \mathbf{h}_i(\boldsymbol{\theta}))_i$ is computed with waveform values at the K_{MB} frequency points, and no additional waveform evaluations are required. Thus, the cost of a single likelihood evaluation is reduced by

$K_{\text{orig}}/K_{\text{MB}}$.

2.2 Extension to parameterized tests

In the previous work (Morisaki, 2021), which applies the multiband decomposition method to the analysis of a GR signal, the 0PN formula of $\tau(f)$ in GR is used for solving Eq. (2.11). For extending the previous work to parameterized tests of GR, we need to take into account corrections of $\tau(f)$ from the parameterized modifications of inspiral phasing. In this section, we derive the modified formula of $\tau(f)$ taking them into account. We also apply it for setting up frequency bands and study the speed-up gains of our method for a typical BNS signal.

2.2.1 Modified time to merger

In order to get the modified time-to-merger formula, we use the following condition in accord to the stationary phase approximation (Sathyaprakash & Dhurandhar, 1991; Poisson & Will, 1995; Creighton & Anderson, 2011; Maggiore, 2007):

$$\Phi(f) = -\Psi(t(f)) + 2\pi f t(f) + \frac{\pi}{4}, \quad (2.17)$$

where $\Psi(t)$ is the phase of a time-domain waveform and $t(f)$ is the time at which $\Psi'(t) = 2\pi f$. Hence, we can now relate $t(f)$ to the derivative of $\Phi(f)$,

$$t(f) = \frac{\Phi'(f)}{2\pi}. \quad (2.18)$$

With the phase formula at inspiral part, we obtain the following modified time-to-merger formula,

$$\tau(f) = t_c - t(f)$$

$$\begin{aligned}
&= \frac{1}{2\pi} \left\{ \frac{7\varphi_{-2}}{3f^{10/3}} + \frac{5(1 + \delta\hat{\varphi}_0)\varphi_0^{\text{GR}}}{3f^{8/3}} + \frac{4\varphi_1}{3f^{7/3}} \right. \\
&+ \frac{(1 + \delta\hat{\varphi}_2)\varphi_2^{\text{GR}}}{f^2} + \frac{2(1 + \delta\hat{\varphi}_3)\varphi_3^{\text{GR}}}{3f^{5/3}} + \frac{(1 + \delta\hat{\varphi}_4)\varphi_4^{\text{GR}}}{3f^{4/3}} \\
&- \frac{(1 + \delta\hat{\varphi}_5^{(l)})\varphi_5^{(l)\text{GR}}}{f} \\
&- \frac{(1 + \delta\hat{\varphi}_6)\varphi_6^{\text{GR}} + (1 + \delta\hat{\varphi}_6^{(l)})\varphi_6^{(l)\text{GR}}(\ln f + 3)}{3f^{2/3}} \\
&\left. - \frac{2(1 + \delta\hat{\varphi}_7)\varphi_7^{\text{GR}}}{3f^{1/3}} \right\}. \tag{2.19}
\end{aligned}$$

Since the time-to-merger is predominantly determined by the terms up to 0PN, we ignore terms higher than that order, and employ the following formula,

$$\tau(f) = \frac{7\varphi_{-2}}{6\pi f^{10/3}} + \frac{5(1 + \delta\hat{\varphi}_0)\varphi_0^{\text{GR}}}{6\pi f^{8/3}} \tag{2.20}$$

$$\begin{aligned}
&= \frac{7\delta\hat{\varphi}_{-2}}{256\pi} \eta^{2/5} \left(\frac{\pi G\mathcal{M}}{c^3} \right)^{-7/3} f^{-10/3} \\
&+ \frac{5(1 + \delta\hat{\varphi}_0)}{256\pi} \left(\frac{\pi G\mathcal{M}}{c^3} \right)^{-5/3} f^{-8/3}. \tag{2.21}
\end{aligned}$$

If higher-order multiple moments are present, the same formula with the frequency rescaling, $f \rightarrow 2f/m$, is used, where m is the maximum magnetic number of the moments.

For validating our approximate time-to-merger formula, we numerically calculate time-domain waveforms incorporating higher-order PN terms and compare their durations with predictions from our formula. Figure 2.1 shows time-domain waveforms for non-spinning $1.4M_\odot$ - $1.4M_\odot$ BNS with various values of $\delta\hat{\varphi}_0$ or $\delta\hat{\varphi}_{-2}$. They are calculated as the inverse Fourier transforms of frequency-domain waveforms from 20 Hz to 1024 Hz that include terms up to the 3.5PN order in phase and the leading-order term in amplitude. The GR phase coefficients have been calculated with `SimInspiralTaylorF2AlignedPhasing` implemented in the LIGO Algorithmic Library (LAL) (LIGO Scientific Collaboration, 2018). The vertical lines represent predictions from our approximate time-to-merger formula with

$f = 20$ Hz. As seen in the figure, vertical lines accurately locate the time when waveforms start, demonstrating that our approximate time-to-merger is accurate enough.

Evaluating Eq. (2.21) demands a choice on the values of \mathcal{M} , η , $\delta\hat{\varphi}_0$, and $\delta\hat{\varphi}_{-2}$. To guarantee that the duration of each frequency band is long enough for any template waveform generated during stochastic sampling, their values are chosen to maximize $\tau(f)$. Hence, the minimum value of \mathcal{M} and the maximum values of η , $\delta\hat{\varphi}_0$, and $\delta\hat{\varphi}_{-2}$ within the explored parameter space are chosen. The maximum value of η is typically 1/4, which corresponds to $m_1 = m_2$.

From Eq. (2.21), it is clear that $\tau(f)$ becomes negative for $\delta\hat{\varphi}_0 < -1$ or $\delta\varphi_{-2} < 0$ unless the other terms are significant enough to compensate it. In this case, the template waveform is an inverse-chirp waveform, which starts from $t = t_c$ and whose frequency simply decreases. The multiband approximation clearly breaks down for this type of waveform since it assumes that the signal frequency simply increases. Even without the multiband approximation, the inverse-chirp signal is not properly analyzed in analysis with the standard data conditioning (Veitch et al., 2015), where only data up to ~ 2 seconds after t_c are analyzed.

Since the higher-order terms are ignored in Eq. (2.21), the huge deviations from GR in one or more of the higher-order terms can make the approximate time-to-merger formula inaccurate. In a typical analysis, the explored range of \mathcal{M} is much wider than the width of its marginal posterior distribution, and the time to merger computed with the minimum \mathcal{M} in the explored range is large enough to construct conservative frequency bands. The same argument can be made for hidden modifications with non-PN frequency dependences considered in (Li et al., 2012). Also, it is straightforward to take into account higher-order terms from Eq. (2.19) when huge deviations of higher-order terms are considered.

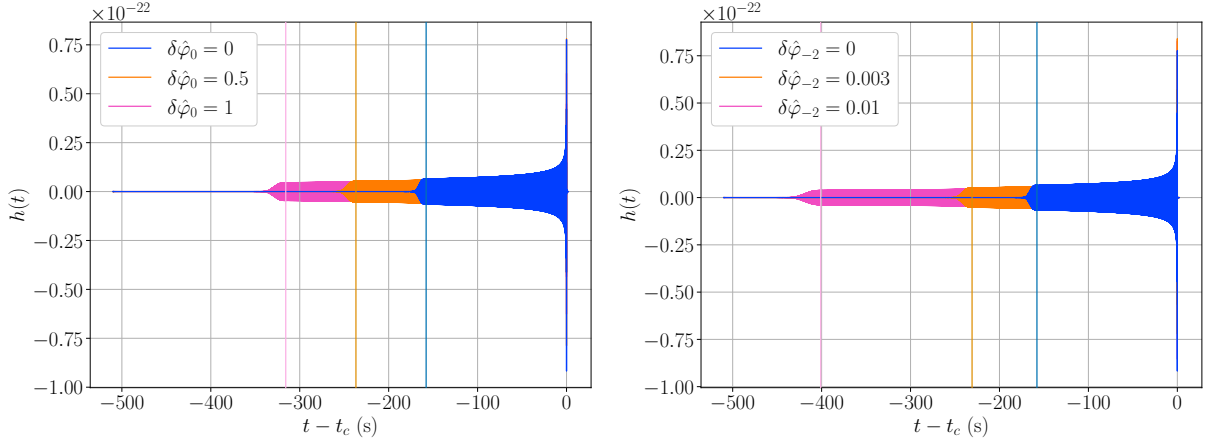


Figure 2.1: Time-domain gravitational waveforms of non-spinning $1.4M_{\odot}$ – $1.4M_{\odot}$ BNS starting from 20 Hz with various values of $\delta\hat{\varphi}_0$ (left) or $\delta\hat{\varphi}_{-2}$ (right). Vertical lines represent durations calculated by the up-to-0PN time-to-merger formula Eq. (2.21).

2.2.2 Speed-up gains

Table 2.1 shows speed-up gains of our multiband technique for a $1.4M_{\odot}$ – $1.4M_{\odot}$ BNS signal with several choices of T and $\delta\hat{\varphi}_i$ used for calculating $\tau(f)$. For each case in the table, frequency bands were set up with the algorithm described in Sec. 2.1.2 and Eq. (2.21) calculated with $m_1 = m_2 = 1.4M_{\odot}$ and $\delta\hat{\varphi}_i$ of the row. The total frequency range is 20–2048 Hz, and the durations of bands are powers of two, $\{T^{(b)}\}_{b=0}^{B-1} = \{T, T/2, T/4, \dots, 4\text{ s}\}$. The speed-up gain is estimated by the reduction of frequency points, $K_{\text{orig}}/K_{\text{MB}}$. For setting up frequency bands, we utilized the existing implementation of the multiband decomposition method, `MBGravitationalWaveTransient`, available in the `bilby` (Ashton et al., 2019; Romero-Shaw et al., 2020) software.

For this study, we consider the 3 choices of $\delta\hat{\varphi}_i$: GR ($\delta\hat{\varphi}_0 = \delta\hat{\varphi}_{-2} = 0$) for reference, 0PN ($\delta\hat{\varphi}_0 = 20$, $\delta\hat{\varphi}_{-2} = 0$), and -1 PN ($\delta\hat{\varphi}_0 = 0$, $\delta\hat{\varphi}_{-2} = 1$). $\delta\hat{\varphi}_0 = 20$ or $\delta\hat{\varphi}_{-2} = 1$ is the maximum of its range explored by LVK analyses, which we have found in configuration files available at (tgr, 2020). In a standard LVK parameterized test, the duration of analyzed data is the same as that used for GR parameter estimation regardless of the explored range of a non-GR parameter. For a $1.4M_{\odot}$ – $1.4M_{\odot}$ BNS signal, $T = 256$ s. In either case with $T = 256$ s in the table, the speed-up gain is $\mathcal{O}(10)$. The speed-up gain for 0PN or -1 PN

Table 2.1: The numbers of original frequency points K_{orig} , the numbers of multibanded frequency points K_{MB} , and speed-up gains $K_{\text{orig}}/K_{\text{MB}}$ for a $1.4M_{\odot}$ - $1.4M_{\odot}$ BNS signal with several choices of data duration T and a non-GR parameter value $\delta\hat{\varphi}_i$ used for calculating time to merger. The total frequency range is 20–2048 Hz, and divided into frequency bands with $\{T^{(b)}\}_{b=0}^{B-1} = \{T, T/2, T/4, \dots, 4\text{ s}\}$.

	$\delta\hat{\varphi}_i$	T (s)	K_{orig}	K_{MB}	Speed up
GR	0	256	5.2×10^5	1.2×10^4	4.5×10^1
0PN ($i = 0$)	20	256	5.2×10^5	2.8×10^4	1.8×10^1
	20	4096	8.3×10^6	6.8×10^4	1.2×10^2
-1PN ($i = -2$)	1	256	5.2×10^5	3.6×10^4	1.4×10^1
	1	32768	6.6×10^7	3.2×10^5	2.1×10^2

is smaller than that for GR because $\tau(f)$ gets larger due to the non-GR modification.

To properly analyze any waveform within the explored range of a non-GR parameter, the data duration should be longer than the longest duration of the waveform with the allowed non-GR modifications. If data durations are determined in that conservative way, $T = 4096$ s and $T = 32768$ s for 0PN and -1 PN respectively. With that conservative choice of T , the speed-up gain gets larger and is $\mathcal{O}(10^2)$ for either case.

2.3 Validation

In this section, we study the accuracy of our technique using simulated BNS signals and real data.

2.3.1 Simulation study

To verify that the multiband approximation does not bias the inference, we simulated BNS signals with non-zero $\delta\hat{\varphi}_i$, and performed parameterized tests on them with and without the multiband decomposition method. The injection values, prior, and explored range of GR parameters are common among simulations, and outlined in Table 2.2. The effects of spin angular momenta and tidal deformation of colliding objects were not taken into account

Table 2.2: The injection values, prior, and explored range of GR parameters: Chirp mass \mathcal{M} , mass ratio $q \leq 1$, luminosity distance D_L , right ascension RA and declination DEC, orbital inclination angle θ_{JN} , polarization angle ψ , constant phase ϕ_c , and coalescence time t_c . The prior uniform in cosine, sine, and comoving volume are denoted by ‘‘Cosine’’, ‘‘Sine’’ and ‘‘Comoving’’ respectively. $t_{c,\text{inj}}$ denotes the injection value of t_c , and is set to the GPS time of 1187008882 (17 Aug 2017, 12:41:04 UTC).

Parameter	Unit	Injection value	Prior	Min.	Max.
\mathcal{M}	M_\odot	1.2	Uniform	1.15	1.25
q	-	0.8	Uniform	0.125	1
θ_{JN}	rad.	0.4	Sine	0	π
D_L	Mpc	72	Comoving	10	100
RA	rad.	3.45	Uniform	0	2π
DEC	rad.	-0.40	Cosine	$-\pi/2$	$\pi/2$
ψ	rad.	0.65	Uniform	0	π
ϕ_c	rad.	1.3	Uniform	0	2π
$t_c - t_{c,\text{inj}}$	s	0	Uniform	-0.1	+0.1

for quick runs. We considered the network of the two advanced LIGO detectors and the Virgo detector, and injected signals into Gaussian noise colored by their design sensitivities. The analyzed frequency range is 20–2048 Hz. The network signal-to-noise ratios (SNRs) of the simulated signals are ~ 50 . The simulated signals were computed with the TaylorF2 (Buonanno et al., 2009; Santamaria et al., 2010) waveform model implemented in LAL, and the same waveform model was used for parameter recovery.

In this study, we considered two simulated signals: the 0PN simulation with $\delta\hat{\varphi}_0 = 1$, $\delta\hat{\varphi}_i = 0$ ($i \neq 0$) and the -1PN simulation with $\delta\hat{\varphi}_{-2} = 0.003$, $\delta\hat{\varphi}_i = 0$ ($i \neq -2$). The duration of a signal from 20 Hz with vanishing non-GR parameters is ~ 160 s. It is doubled for the 0PN simulation or increased by $\sim 50\%$ for the -1PN simulation due to the non-zero GR parameter. The explored parameter range is $-1 \leq \delta\hat{\varphi}_0 \leq 2$ for the 0PN simulation and $-0.01 \leq \delta\hat{\varphi}_{-2} \leq 0.01$ for the -1PN simulation. For each simulation, the prior of the non-GR parameter is uniform over its explored range.

The durations of analyzed data are 512 s and 256 s for the 0PN and -1PN simulations respectively. The total frequency range is divided into 8 frequency bands with $\{T^{(b)}\}_{b=0}^7 = \{512\text{ s}, 256\text{ s}, \dots, 4\text{ s}\}$ for the multiband run of the 0PN simulation, and 7 frequency

bands with $\{T^{(b)}\}_{b=0}^6 = \{256 \text{ s}, 128 \text{ s}, \dots, 4 \text{ s}\}$ for the -1PN simulation. The speed-up gains $K_{\text{orig}}/K_{\text{MB}}$ are 58 and 37 for the 0PN and -1PN simulations respectively.

The stochastic sampling was performed with the `bilby` software and the `dynesty` (Speagle, 2020) sampler. The convergence of sampling is controlled by the number of live points n_{live} and the length of the MCMC chain in unit of its auto-correlation length n_{ACT} (Romero-Shaw et al., 2020). We used $n_{\text{live}} = 500, n_{\text{ACT}} = 10$ and $n_{\text{live}} = 1000, n_{\text{ACT}} = 10$ for the 0PN and -1PN simulations respectively. We have confirmed that increasing their values does not change the results significantly, which means the results are converged. We marginalized the posterior over constant phase ϕ_c analytically and luminosity distance D_L using the look-up table method (Singer & Price, 2016; Thrane & Talbot, 2019).

Figures 2.2 and 2.3 show marginal posterior distributions of chirp mass (\mathcal{M}), mass ratio (q), and a non-GR parameter ($\delta\hat{\varphi}_0$ or $\delta\hat{\varphi}_{-2}$) for the 0PN and -1PN simulations respectively. The runs without and with the multiband approximation are labeled “Standard” and “Multiband” respectively. As shown in the figures, the standard and multiband runs produce almost equivalent results in either simulation. More quantitatively, the differences in the lower or upper bounds of the 90% credible intervals are less than 4% of their widths. Those observations indicate that the multiband approximation is accurate enough for a relatively high SNR of ~ 50 . Since log-likelihood errors introduced by the multiband approximation are roughly proportional to the square of SNR, they are smaller for lower SNR values. Therefore, our results show that our multiband approximation can be safely used also for SNR values below 50. The full posterior distributions of all the inferred parameters are presented in Figs 2.5 and 2.6.

The standard runs took ~ 9 days and ~ 14 days to complete for the 0PN and -1PN simulations respectively. They are reduced to ~ 2 hours and ~ 7 hours respectively with the multiband approximation. The reduction of run times is more or less consistent with the speed-up gains estimated from $K_{\text{orig}}/K_{\text{MB}}$. The runs were performed with an Intel Xeon Gold 6136 CPU with a clock rate of 3.0 GHz. The stochastic sampling is parallelized

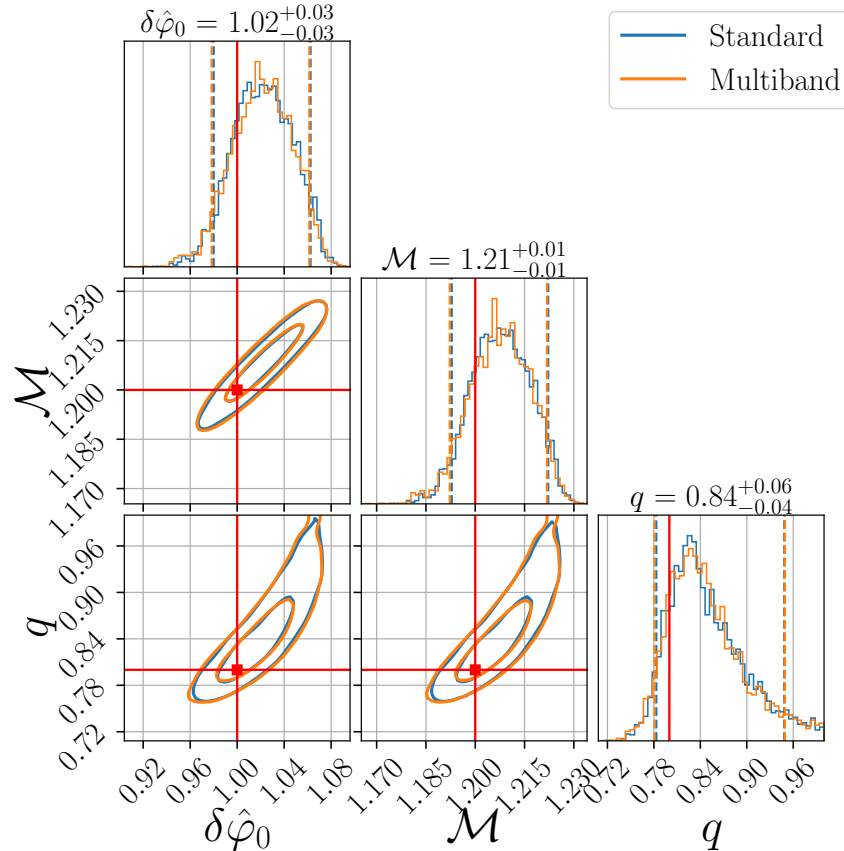


Figure 2.2: One- and two-dimensional marginal posterior distributions of chirp mass \mathcal{M} , mass ratio q , and 0PN relative deviation $\delta\hat{\varphi}_0$ from runs without (blue) and with (orange) the multiband decomposition technique. Diagonal panels show one-dimensional marginal posterior distributions, and vertical dashed lines indicate the 90% credible intervals. Off-diagonal panels show two-dimensional marginal posterior distributions, and solid lines indicate the 50% and 90% credible regions. Red lines indicate the injection values.

with 48 processes for the 0PN simulation, and 24 processes for the -1 PN simulation.

2.3.2 Likelihood errors for GW190814

For validating our approximation with more complicated signal morphology, we investigate the likelihood errors of our approximation for GW190814 (Abbott et al., 2020c). We computed $\ln \mathcal{L}$ with and without our approximation on posterior samples from LIGO-Virgo parameter estimation analysis, and computed their differences $\Delta \ln \mathcal{L}$ as errors. This signal is an appropriate test case for validating our approximation with gravitational-wave

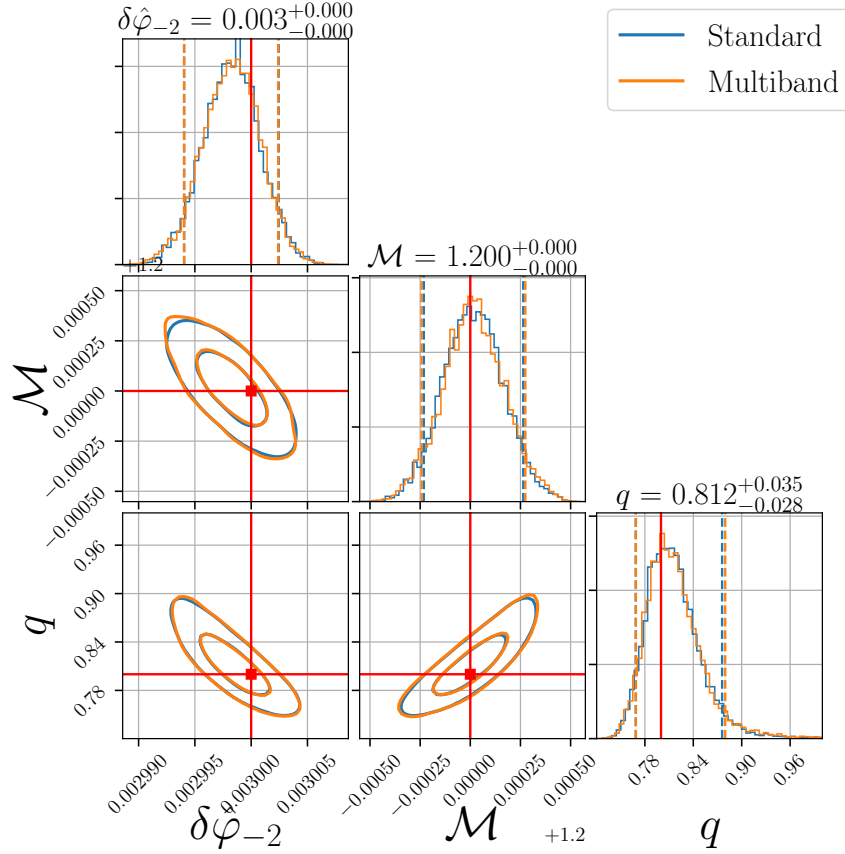


Figure 2.3: One- and two-dimensional marginal posterior distributions of chirp mass \mathcal{M} , mass ratio q , and -1PN absolute deviation $\delta\hat{\varphi}_{-2}$ from runs without (blue) and with (orange) the multiband decomposition technique. Diagonal panels show one-dimensional marginal posterior distributions, and vertical dashed lines indicate the 90% credible intervals. Off-diagonal panels show two-dimensional marginal posterior distributions, and solid lines indicate the 50% and 90% credible regions. Red lines indicate the injection values.

higher-order multiple moments since their effects are statistically significant for this signal (Abbott et al., 2020c). We also considered the calibration uncertainties of detectors for validating our approximation with signal modulation caused by them. The data were obtained from the Gravitational Wave Open Science Center (gwo, 2020), and posterior samples were from (tgr, 2020). The IMRPhenomPv3HM (Khan et al., 2019, 2020) waveform model was employed for likelihood evaluations, which is the same model used for the LVK analysis.

Figure 2.4 shows $|\Delta \ln \mathcal{L}|$ with the horizontal axis representing the non-constant part of $\ln \mathcal{L}$,

$$\ln \Lambda \equiv \sum_i \left[(\mathbf{d}_i, \mathbf{h}_i)_i - \frac{1}{2} (\mathbf{h}_i, \mathbf{h}_i)_i \right]. \quad (2.22)$$

The left plot shows the errors for tests of inspiral parameters and the right for tests of post-merger parameters. The total frequency range of 20–1024 Hz was divided into 3 frequency bands with $\{T^{(b)}\}_{b=0}^2 = \{16 \text{ s}, 8 \text{ s}, 4 \text{ s}\}$. The frequency bands were determined based on the time-to-merger of the $m = 4$ mode, and with the following reference values of \mathcal{M} , η , $\delta\hat{\varphi}_0$, and $\delta\hat{\varphi}_{-2}$,

$$\begin{aligned} \mathcal{M} &= 5.5M_\odot, \quad \eta = 0.25, \\ \delta\hat{\varphi}_0 &= \begin{cases} 20, & \text{(test of } \delta\hat{\varphi}_0) \\ 0, & \text{(otherwise)} \end{cases} \\ \delta\hat{\varphi}_{-2} &= \begin{cases} 1, & \text{(test of } \delta\hat{\varphi}_{-2}) \\ 0. & \text{(otherwise)} \end{cases} \end{aligned} \quad (2.23)$$

Those reference values were determined based on the parameter range explored by the LVK analysis. The speed-up gain is 2.42 for the test of $\delta\hat{\varphi}_0$, 2.44 for the test of $\delta\hat{\varphi}_{-2}$, and 3.28 for the other cases. The *IFFT-FFT* algorithm was employed for computing $(\mathbf{h}, \mathbf{h})_i$ due to significant higher-order multiple moments.

Each plot label shows the median value of $|\Delta \ln \mathcal{L}|$. The errors are $\lesssim 10^{-4}$ for the test of $\delta\hat{\varphi}_0$ or $\delta\hat{\varphi}_{-2}$, and $\lesssim 10^{-3}$ for the other tests. The smaller errors for the former case are

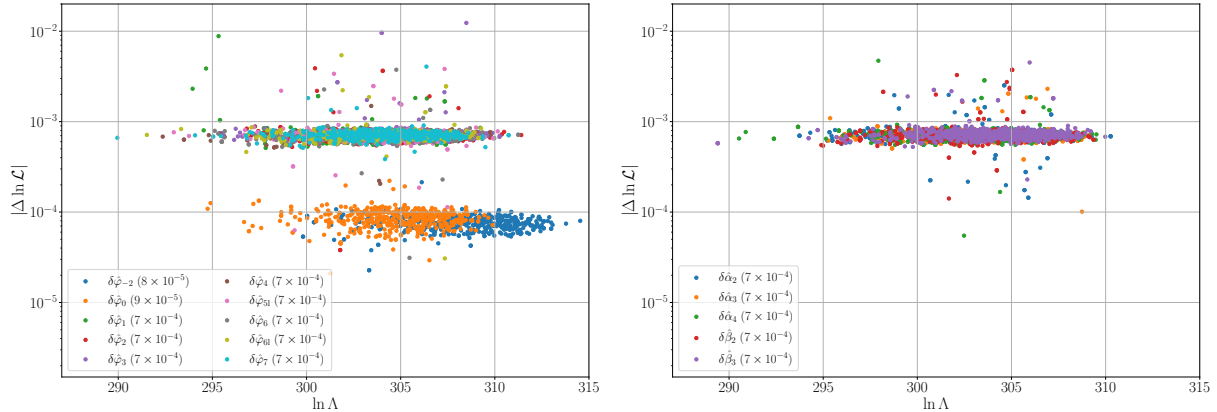


Figure 2.4: Log-likelihood errors $|\Delta \ln \mathcal{L}|$ of the multiband approximation calculated on posterior samples from GW190814. The left plot shows the errors for tests of inspiral non-GR parameters and the right for tests of post-inspiral non-GR parameters. Each label shows the median value of these errors.

because frequency bands are constructed from a longer time-to-merger due to $\delta\hat{\varphi}_0 > 0$ or $\delta\hat{\varphi}_{-2} > 0$. In either case, the errors are much smaller than the unity, which shows our approximation is accurate enough for the analysis of GW190814.

2.4 Conclusion

In this paper, we have presented a rapid inference technique for parameterized tests of GR, one of the main tests of GR using gravitational waves from CBC. Our technique is based on a multiband decomposition of the gravitational-wave likelihood, which was originally developed for speeding up parameter estimation of CBC signals under the assumption of GR. It exploits the chirping nature of a signal, and in principle is applicable to any chirp signal whose time to merger $\tau(f)$ is known. To extend this technique to parameterized tests of GR, we have derived $\tau(f)$ taking into account non-GR deformations of the waveform. Applying the multiband decomposition technique with our new formula of $\tau(f)$ to a $1.4M_\odot$ – $1.4M_\odot$ BNS signal, we have found that our technique speeds up parameterized tests of a typical BNS signal by a factor of $\mathcal{O}(10)$ for the low-frequency cutoff of 20 Hz.

For validating our approximate technique, we have simulated BNS signals with SNRs

of ~ 50 . Performing parameterized tests of them with and without our technique, we have verified that our technique produces results equivalent to those from runs without any approximate methods. We have also computed log-likelihood errors of our technique for GW190814 and confirmed that they are well below unity. Therefore, our work provides an efficient and accurate way of performing parameterized tests of GR, which is useful for dealing with more frequent detections in future observations.

We focus on single-parameter tests throughout this work. In principle, our technique can be applied to multiple-parameter tests using principal component analysis ([Shoom et al., 2023](#); [Saleem et al., 2022](#)), with a modified time-to-merger formula parameterized by parameters corresponding to principal directions. We leave that extension as a future work.

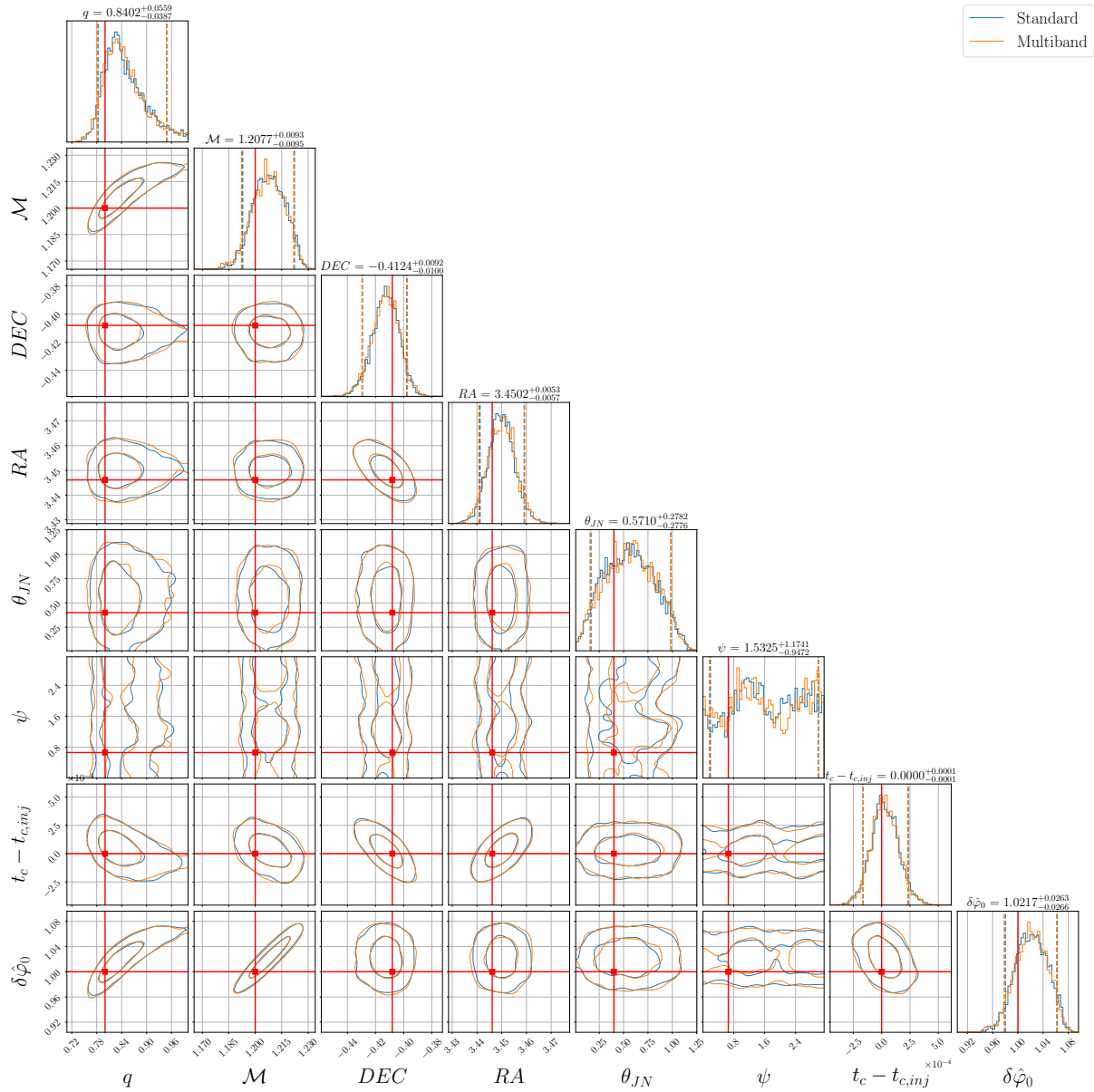


Figure 2.5: One- and two-dimensional marginal posterior distributions of all the inferred parameters for the 0PN simulation from runs without (blue) and with (orange) the multiband decomposition technique. Diagonal panels show one-dimensional marginal posterior distributions, and vertical dashed lines indicate the 90% credible intervals. Off-diagonal panels show two-dimensional marginal posterior distributions, and solid lines indicate the 50% and 90% credible regions. Red lines indicate the injection values.

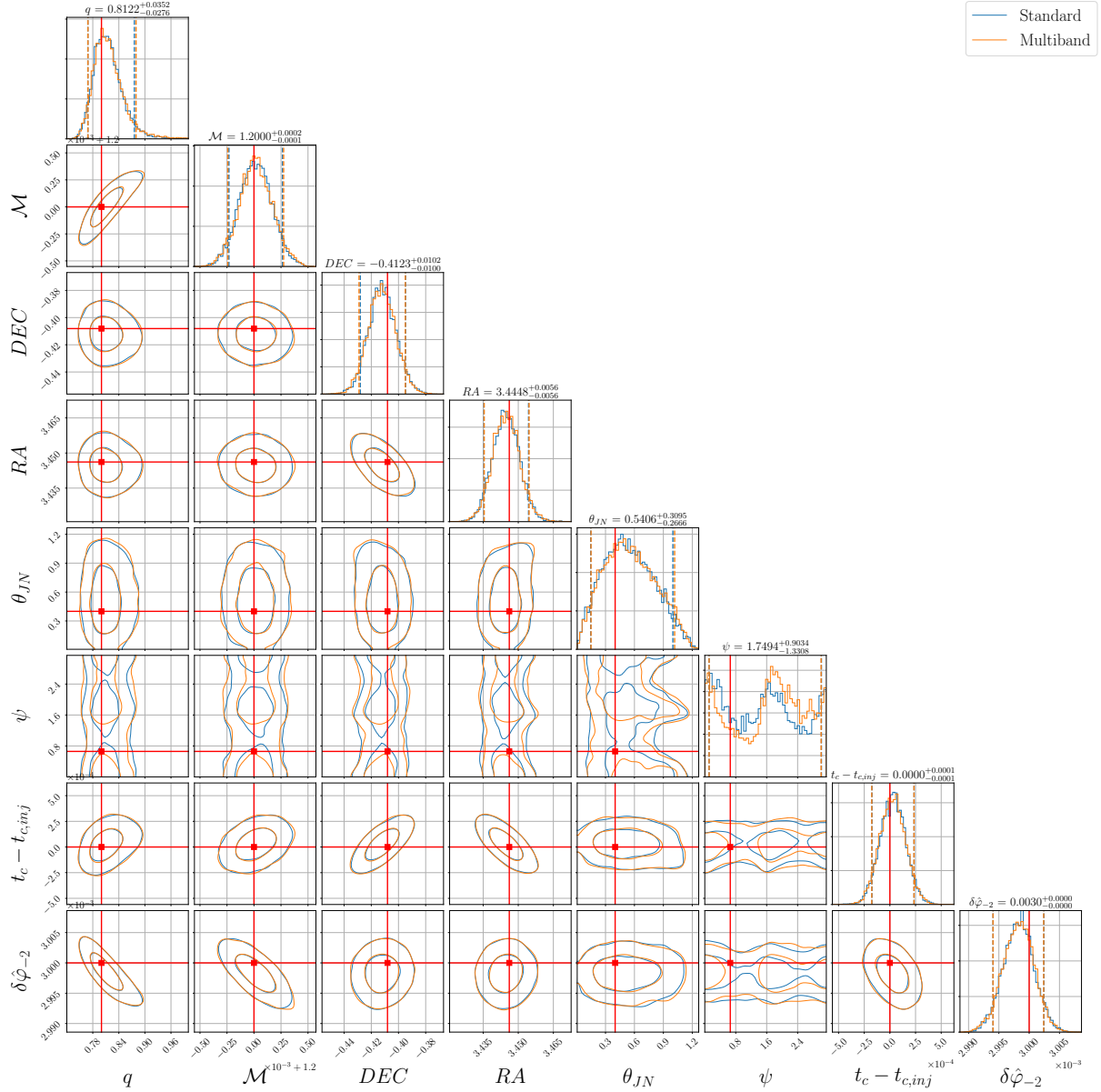


Figure 2.6: One- and two-dimensional marginal posterior distributions of all the inferred parameters for the -1PN simulation from runs without (blue) and with (orange) the multiband decomposition technique. Diagonal panels show one-dimensional marginal posterior distributions, and vertical dashed lines indicate the 90% credible intervals. Off-diagonal panels show two-dimensional marginal posterior distributions, and solid lines indicate the 50% and 90% credible regions. Red lines indicate the injection values.

Chapter 3

Searching for multi-messenger events with LIGO-Virgo-KAGRA

This chapter is partially reproduced from [Chaudhary et al. \(2024\)](#), specifically relating to [3.2.3](#), and has been published in the Proceedings of the National Academy of Sciences. An online version is available at <https://doi.org/10.1073/pnas.2316474121>.

Additionally, this chapter includes preliminary results from a manuscript currently in preparation.

Gamma-ray bursts (GRBs) are irregular and intense pulses of γ -radiation lasting from a few seconds to minutes with a non-thermal spectrum at $\sim 10 - 10^4$ keV. They are observed a few times per day and are distributed uniformly across the sky. It is widely accepted that the majority of these bursts originate from outside the Milky Way at cosmological distances ([Meegan et al., 1992](#); [Costa et al., 1997](#); [Piran, 2004](#)). Depending on the duration of these bursts, they are classified into short GRBs (with a typical duration of less than 2 seconds) and long GRBs (with a duration of more than 2 seconds). Based solely on the

burst duration, prior to any information about the distance to the source or its physical origin (Fernández et al., 2015), it was speculated that these two classes corresponded to two physically distinct progenitors (Kumar & Zhang, 2014). Additionally, short GRBs typically have hard spectra, whereas long GRBs have soft spectra (Kouveliotou et al., 1993).

Observations have now confirmed that some long GRBs are associated with the collapse of rapidly-rotating massive stars (core-collapse supernovae) (Bloom et al., 2002; Fruchter et al., 2006; Cano et al., 2017) and some short GRBs (sGRB) originate in the mergers of binary neutron stars (BNS) (Abbott et al., 2017c). It is also possible that some of them may be generated by neutron star-black hole (NSBH) mergers (Kochanek & Piran, 1993; Narayan et al., 1992; Mészáros, 2019).

Recent observations of long GRBs associated with kilonovae, i.e. binary neutron star mergers, (Troja et al., 2022; Gompertz et al., 2023; Levan et al., 2024) and short GRBs associated with supernova (SN) (Ahumada et al., 2021; Rossi et al., 2022) have brought the simple classification by duration into tension. Recent analyses of event classifications were conducted by Dimple et al. (2023). More details on the physics relating to central engines and the time-delay in high-energy radiation emission can be found in Burns (2020); Burns et al. (2023).

The observation of gravitational-wave (GW) and short gamma-ray burst signals from the binary neutron star merger GW 170817 (Abbott et al., 2017c; Savchenko et al., 2017a; Goldstein et al., 2017a) has started a new era of multi-messenger astronomy (Abbott et al., 2017d), enabling us to study fundamental physics, cosmology, and high-energy astrophysics. Joint GW-sGRB detections from the same source allowed us to constrain the speed of gravity (Abbott et al., 2017b), obtain an independent measure of the Hubble constant (Abbott et al., 2017a, 2021a), and find evidence for heavy element production via r-process nucleosynthesis in a kilonova (Chornock et al., 2017; Kasen et al., 2017; Pian et al., 2017; Watson et al., 2019).

Motivated by the wealth of science from multi-messenger observations like these, we

are interested in improving the number of joint GW-sGRB coincident detections. Other prospective types of multi-messenger events include GW-long gamma-ray bursts (Bloom et al., 2002), GW-neutrino bursts (Agostini et al., 2017), and GW-fast radio bursts (Totani, 2013; Moroianu et al., 2023). We hope to detect such joint events in the near future.

The analysis method discussed in the following subsection 3.1.3 can be generalized to any two types of multi-messenger events, assuming that each signal comes with its own statistical significance and that some correlation could exist between the two signals, such as the time of arrival and/or a common source. The distribution that describes the probability of detecting multi-messenger events, given the source parameters, can vary depending on the specific characteristics of the events and the detection process.

The probability of detection is influenced by various factors, including the source distance and localization, the strength of the signal, and the sensitivity of the detectors. The specific form of the distribution will depend on the particular scenario and modeling assumptions. In the case of comparing two different signals from multi-messenger events under null and alternative hypotheses, there are several approaches for measuring the difference or similarity between them in computing the posterior probabilities (e.g., Finn, 1997; Urban, 2016; Ashton et al., 2018; Cho, 2019; Nitz et al., 2019; Bartos et al., 2019; Stachie et al., 2020; Veske et al., 2021; Piotrkowski et al., 2022; Pillas et al., 2023; Pillas, 2023). The choice of method depends on the nature of the signals being compared and the hypothesis to be tested.

3.1 Basics

3.1.1 Elements of gravitational-wave detection

In this subsection, we briefly explore how detection statistics work for compact binary coalescence (modeled) (Messick et al., 2017; Aubin et al., 2021) and burst (unmodeled) events, and how these events are classified as gravitational wave candidates in low-latency

searches.

In modeled searches, the matched-filtering signal-to-noise ratio (SNR) ρ_{mf} is used (Cutler & Flanagan, 1994; Jaranowski & Krolak, 2009; Creighton & Anderson, 2011; Allen et al., 2012; Abbott et al., 2020a) to estimate the probability that an event has been detected. The SNR is given by

$$\rho_{\text{mf}}^2 = 4 \Re \int_0^\infty \frac{\tilde{h}^*(f)\tilde{d}(f)}{S_n(f)} df, \quad (3.1)$$

where $\tilde{d}(f)$ is the Fourier transform of the measured strain that contains both signal and noise, $\tilde{h}(f)$ is the Fourier transform of the modeled signal, and $S_n(f)$ is the power spectral density of the interferometric noise. When dealing with Gaussian noise, the matched-filter SNR is the optimal detection statistic.

For unmodeled GW signals that are short in duration and come from burst sources, such as core-collapse supernovae, we look for excess power in the detector output from multiple detectors (Klimenko et al., 2008, 2016; Drago et al., 2021).

However, the noise in interferometric detectors is rarely stationary or Gaussian, so the SNR must be supplemented with additional discriminators between gravitational-wave signals and other nuisance noise. Modern detection pipelines (Sachdev et al., 2019; Usman et al., 2016; Dal Canton et al., 2021; Adams et al., 2016; Chu et al., 2022; Klimenko et al., 2008; Robinet et al., 2020) combine these statistics together into a likelihood. Larger likelihood values are correlated with higher probability that a gravitational-wave signal is present in the data. The Neyman-Pearson criterion for detection statistics applied to the likelihood provides a framework for testing the presence of a signal in the data, requiring the likelihood to surpass a predefined threshold. We can compute how often noise causes the likelihood to exceed the threshold: this is called the False Alarm Rate (FAR) at that threshold (Zheng et al., 2021; Coleman Miller & Yunes, 2021). During an observing run, the interferometric detectors record data, which are streamed to data analysis computing machines. A variety of detection algorithms are employed on these GW data that contain both noise and/or signals. Signals with sufficiently small FAR are classified as

gravitational-wave event candidates, or **G-events**. Further investigations are carried out on these candidates which are also assigned a probability of astrophysical origin.

G-events reported by the various online search algorithms¹ that are likely related to a common gravitational-wave signal are clustered into a **Superevent**, following an SYYMMDDa-z or SYYMMDDaa-zz naming convention to allow multiple events in a single day. For a gravitational wave event to be publicly recognized as a **Superevent**, it must pass a preset FAR threshold for modeled or unmodeled searches, depending on the mode by which it was detected².

3.1.2 Elements of electromagnetic detection

In this subsection, we briefly explain how GRBs of various significance levels are detected. We also provide a concise overview of participating electromagnetic (EM) facilities, including their processes for reporting and communicating highly energetic transient detections to the external community. In Section 3.2, we discuss how the LVK Collaboration utilizes online coincident searches with these GRBs.

The Fermi Gamma-ray Burst Monitor (GBM) (Meegan et al., 2009) has a field of view (FOV) that covers approximately 8 steradians, which is equivalent to $\frac{8}{4\pi} \approx 64\%$ of the full sky. It is sensitive to gamma rays in the range of 8 keV to 40 MeV range, effectively covering the typical energy range of GRBs. The GBM generates onboard triggers for approximately 250 GRBs per year that pass the sensitivity threshold. According to the Fourth Fermi-GBM Gamma-Ray Burst Catalog (von Kienlin et al., 2020), 2356 GRBs have been identified as cosmic over a period of a decade, implying 236 GRBs per year.

The Swift Burst Alert Telescope (BAT) (Barthelmy et al., 2005) has a FOV of around 1.4 steradians (partially-coded), or about 12% of the full sky. The BAT is sensitive to gamma rays in the 15-150 keV energy range. Based on observations, the rate of GRBs

¹See <https://emfollow.docs.ligo.org/userguide/analysis/searches.html> for more background information on GW search pipelines.

²See <https://emfollow.docs.ligo.org/userguide/analysis/index.html> for more information on implemented public alert thresholds.

beaming towards Earth with fluxes above the BAT detection threshold in this energy band is around 700 per full sky per year. Accounting for the BAT's FOV, this suggests the BAT could detect up to around $700 \times 0.12 = 84$ GRBs per year (Lien et al., 2016). However, the BAT does not spend 100 % of the time looking for GRBs. Taking into account time spent following up GRB detections, slewing, and other observational duties, the BAT has an active duty cycle around 80-85 %. Accounting for this, an upper bound on the BAT GRB detection rate is: $84 \times 0.85 \approx 71$ GRBs per year.

The InternatIonal Gamma-Ray Astrophysics Laboratory (INTEGRAL) (Winkler et al., 2003) has a FOV of approximately 0.02 steradians. This limited FOV enables detailed observation and high-resolution imaging of gamma-ray sources. INTEGRAL is equipped with instruments such as the Imager on Board the INTEGRAL Satellite (IBIS), which is sensitive from approximately 15 keV to 10 MeV, and the Spectrometer on INTEGRAL (SPI), which is sensitive from 20 keV to 8 MeV. These instruments are designed to detect and study high-energy phenomena, including GRBs. INTEGRAL detects a GRB every other month.

The Astro rivelatore Gamma a Immagini Leggero (AGILE) was an X-ray and gamma-ray astronomical satellite launched in 2007, and it deorbited in Feb 2024³. The AGILE MiniCalorimeter (MCAL) (Tavani et al., 2009) had an all-sky non-imaging detector, sensitive in the 400 keV–100 MeV energy range. MCAL had a wide field of view, covering approximately one-sixth of the entire sky. This extensive coverage allowed for continuous monitoring of a large portion of the sky and enabled the detection of several dozen bursts per year during its operational period.

The Space Variable Objects Monitor (SVOM) (Atteia et al., 2023) ECLAIRs has a FOV of around 2 steradians, or about 16% of the full sky, and is sensitive to the 4-120 keV energy range. We can expect SVOM to detect⁴ unique additional GRBs following the logic

³<https://www.astronomerstelegram.org/?read=16450>

⁴SVOM launched on June 22, 2024, and is currently in the commissioning phase at the time of writing.

below since its energy range is similar to that of Fermi and Swift.

$$\text{ECLAIRs additional rate} \approx \left(1 - \frac{8 \text{ sr}}{4\pi \text{ sr}}\right) \times \left(1 - \frac{1.4 \text{ sr}}{4\pi \text{ sr}}\right) \times \frac{67}{\text{yr}}, \quad (3.2)$$

$$\sim \frac{22}{\text{yr}}, \quad (3.3)$$

where:

- The terms $\left(1 - \frac{8 \text{ sr}}{4\pi \text{ sr}}\right)$ and $\left(1 - \frac{1.4 \text{ sr}}{4\pi \text{ sr}}\right)$ represent the probabilities that a GRB is not within the FOV of Fermi and Swift, respectively.
- The expected rate of GRB detection by SVOM (specifically, ECLAIRs) is factored as 67/yr. ECLAIRs is expected to detect approximately 200 GRBs of all types during the nominal 3-year mission lifetime.

Significant GRBs: General Coordinates Network (GCN) notices⁵ report triggers produced by the on-board software and immediately communicated to the ground by Fermi, Swift, INTEGRAL, and AGILE-MCAL satellites. These triggers are ranked based on classification and sky location. GCN latency is typically a few seconds.

Low-significant GRBs:

- a. SubGRB: GCN Notices are generated from an analysis pipeline that runs on Fermi-GBM data, which has been downlinked to the ground. These notices have a latency of a few hours.
- b. SubGRBTargeted: Kafka JSON schemas⁶ are generated from an analysis pipeline of the Fermi and Swift Collaborations based on the reported GW candidate detection time by the LVK Collaboration. This pipeline runs on Fermi-GBM and SWIFT-BAT data, which have been downlinked to the ground. It has a latency of a few hours.

The rates of GRBs (significant and low-significant) have been described briefly earlier for each participating EM facility used in our low-latency multi-messenger searches.

⁵Real-time, machine-readable XML files for alert distribution: <https://gcn.nasa.gov/docs/notices>.

⁶<https://emfollow.docs.ligo.org/userguide/tutorial/receiving/gcn.html>

3.1.3 Joint statistical method for analyzing gravitational-wave and electromagnetic data

In this subsection, we will focus on developing a method for multi-messenger events involving gravitational waves and short gamma-ray bursts. We use Bayes's theorem to quantify the significance of joint triggers resulting from the coalescence of binary neutron stars, considering both gravitational radiation and prompt gamma-ray emission. This approach allows us to calculate the probability of these joint triggers given the available data and prior knowledge about the observed events.

Let's begin by outlining the null (noise) and alternative (signal) hypotheses:

- a. \mathcal{H}_0 : No BNS coalescence (null hypothesis).
- b. \mathcal{H}_1 : BNS coalescence and prompt gamma-ray emission (alternative hypothesis).

Now, according to Bayes's theorem, we can calculate the posterior probability of the null hypothesis given the joint triggers, we write:

$$p(\mathcal{H}_0|\mathcal{D}) = \frac{p(\mathcal{D}|\mathcal{H}_0) \cdot p(\mathcal{H}_0)}{p(\mathcal{D})}. \quad (3.4)$$

Here, $\mathcal{D} = \{x_{gw}, x_\gamma\}$ represents the set of joint triggers consisting of gravitational radiation (x_{gw}) and prompt gamma-ray emission (x_γ). $p(\mathcal{D}|\mathcal{H}_0)$ represents the likelihood of observing the joint triggers under the null hypothesis, which denotes the probability of the joint triggers occurring if there is no BNS coalescence. $p(\mathcal{H}_0)$ is the prior probability of the noise hypothesis, reflecting the initial belief or knowledge about the likelihood of no BNS coalescence. The remaining term, $p(\mathcal{D})$, serves as a normalization factor, representing the overall probability of observing the joint triggers. It can be written as the sum of the likelihoods for both hypotheses, and is defined as:

$$p(\mathcal{D}) = p(\mathcal{D}|\mathcal{H}_0) \cdot p(\mathcal{H}_0) + p(\mathcal{D}|\mathcal{H}_1) \cdot p(\mathcal{H}_1), \quad (3.5)$$

taking into account the joint triggers and the prior probabilities associated with the null hypothesis (\mathcal{H}_0) and the alternative hypothesis (\mathcal{H}_1).

To evaluate the significance of the joint triggers, we compare the posterior probability of the signal hypothesis, $p(\mathcal{H}_1|\mathcal{D})$, with that of the null hypothesis, $p(\mathcal{H}_0|\mathcal{D})$. A higher posterior probability for the signal hypothesis indicates stronger evidence in favor of BNS coalescence, while a higher posterior probability for the null hypothesis suggests weaker evidence or no support for BNS coalescence. In this subsection, our objective is to derive the joint false alarm rate for such coincident events. Therefore, we start by evaluating $p(\mathcal{H}_0|\mathcal{D})$, as this closely resembles the ranking statistic widely used in gravitational wave astronomy to classify triggers. Using Eq. (3.5) into Eq. (3.4), we can write

$$p(\mathcal{H}_0|\mathcal{D}) = \frac{p(\mathcal{D}|\mathcal{H}_0) \cdot p(\mathcal{H}_0)}{p(\mathcal{D}|\mathcal{H}_0) \cdot p(\mathcal{H}_0) + p(\mathcal{D}|\mathcal{H}_1) \cdot p(\mathcal{H}_1)}. \quad (3.6)$$

Eq. (3.6) simplifies to

$$p(\mathcal{H}_0|\mathcal{D}) = \frac{1}{1 + \frac{p(\mathcal{D}|\mathcal{H}_1) \cdot p(\mathcal{H}_1)}{p(\mathcal{D}|\mathcal{H}_0) \cdot p(\mathcal{H}_0)}}. \quad (3.7)$$

We can further simplify our null hypothesis by dividing it into four sub-hypotheses:

- a. Both signals are not real and are simply noise (\mathcal{H}_{nn}).
- b. Only the gravitational-wave signal is real, while the gamma-ray burst signal is not (\mathcal{H}_{sn}).
- c. Only the gamma-ray burst signal is real, while the gravitational-wave signal is not (\mathcal{H}_{ns}).
- d. Both signals are real and originate from distinct sources (\mathcal{H}_{ss}).

In a similar manner, the alternative hypothesis can be made clearer by positing that both signals are real and originate from the same source (\mathcal{H}^c). Hence, Eq. (3.7) can be written as

$$p(\mathcal{H}_0|\mathcal{D}) = \frac{1}{1 + \frac{p(\mathcal{D}|\mathcal{H}^c) \cdot p(\mathcal{H}^c)}{p(\mathcal{D}|\mathcal{H}_{nn}) \cdot p(\mathcal{H}_{nn}) + p(\mathcal{D}|\mathcal{H}_{sn}) \cdot p(\mathcal{H}_{sn}) + p(\mathcal{D}|\mathcal{H}_{ns}) \cdot p(\mathcal{H}_{ns}) + p(\mathcal{D}|\mathcal{H}_{ss}) \cdot p(\mathcal{H}_{ss})}}. \quad (3.8)$$

In cases where the datasets x_{gw} and x_γ originate from the same source, they are dependent

on each other and share common parameters θ . Therefore, the likelihood probability of observing joint triggers in the datasets under the signal hypothesis, assuming a BNS coalescence event is given by

$$\begin{aligned} p(\mathcal{D}|\mathcal{H}^c) &\equiv p(x_{gw}, x_\gamma|\mathcal{H}^c) = \int_{\Theta} p(x_{gw}, x_\gamma, \theta|\mathcal{H}^c) d\theta \\ &= \int_{\Theta^S} p(x_{gw}, x_\gamma|\theta, \mathcal{H}^c)p(\theta|\mathcal{H}^c) d\theta, \end{aligned} \quad (3.9)$$

where the integral in the second line is limited to the prior support of \mathcal{H}^c .

Now, we define the ranking statistic as follows:

$$\frac{p(\mathcal{D}|\mathcal{H}_1) \cdot p(\mathcal{H}_1)}{p(\mathcal{D}|\mathcal{H}_0) \cdot p(\mathcal{H}_0)} \equiv \Lambda, \quad (3.10)$$

and rewrite Eq. (3.7) as

$$p(\mathcal{H}_0|\mathcal{D}) = \frac{1}{1 + \Lambda}. \quad (3.11)$$

The posterior probability of the signal hypothesis can now be expressed as follows:

$$p(\mathcal{H}_1|\mathcal{D}) = 1 - p(\mathcal{H}_0|\mathcal{D}) = \frac{\Lambda}{1 + \Lambda} = f(\Lambda). \quad (3.12)$$

It is self-evident from Eq. (3.12) that in the case of a loud BNS coalescence event, specifically when $p(\mathcal{H}_1|\mathcal{D}) = 1$, the value of Λ is significantly greater than 1. We also observe that $p(\mathcal{H}_1|\mathcal{D}) \rightarrow 0$ as $\Lambda \rightarrow 0$. Furthermore, the derivative of $f(\Lambda)$ with respect to Λ , i.e., $\frac{df(\Lambda)}{d\Lambda} = \frac{1}{(1+\Lambda)^2}$, is greater than 0. Similarly, from Eq. (3.11), we can infer that $p(\mathcal{H}_0|\mathcal{D}) \rightarrow 0$ as $\Lambda \rightarrow \infty$, and $p(\mathcal{H}_0|\mathcal{D}) \rightarrow 1$ as $\Lambda \rightarrow 0$. Hence, in the $\Lambda \gg 1$ limit,

$$p(\mathcal{H}_0|\mathcal{D}) \approx \frac{1}{\Lambda} = \frac{p(\mathcal{D}|\mathcal{H}_0) \cdot p(\mathcal{H}_0)}{p(\mathcal{D}|\mathcal{H}_1) \cdot p(\mathcal{H}_1)}. \quad (3.13)$$

In such a scenario, we can infer that the null hypothesis is less probable, leading to a significantly lower joint false alarm rate. Consequently, we can proceed with the sub-

hypotheses that there is the presence of both signal and noise, as well as the presence of noise only, in the respective datasets.

This is expressed by stating the following assumption in Eq. (3.13):

$$p(\mathcal{H}_0|\mathcal{D}) \approx \frac{p(\mathcal{D}|\mathcal{H}_{nn}) \cdot p(\mathcal{H}_{nn}) + p(\mathcal{D}|\mathcal{H}_{ns}) \cdot p(\mathcal{H}_{ns}) + p(\mathcal{D}|\mathcal{H}_{sn}) \cdot p(\mathcal{H}_{sn})}{p(\mathcal{D}|\mathcal{H}^c) \cdot p(\mathcal{H}^c)}. \quad (3.14)$$

Hence, for small $p(\mathcal{H}_0|\mathcal{D})$, the posterior probability of the signal hypothesis, as presented in Eq. (3.12), is given by:

$$p(\mathcal{H}_1|\mathcal{D}) = 1 - p(\mathcal{H}_0|\mathcal{D}). \quad (3.15)$$

3.1.3.1 Filtering of the data

In exploring the data from GW and GRB signals, the following considerations are made:

- i) Both are types of time-series data.
- ii) GRB signal arises from the merger of a binary neutron star system and is associated with a delay, denoted as Δt . This time delay is conservatively estimated for use in the multi-messenger event search process. In the astrophysical context, we classify a short gamma-ray burst signal as having a duration of $T_{90} < 2$ seconds, as described in [Abbott et al. \(2022\)](#). GRB170817A was detected with a time delay of 1.7 seconds following the GW170817 signal ([Abbott et al., 2017b,d](#)). The detailed physical process of this time delay is discussed in [Zhang \(2019\)](#).

Two distinct datasets, each consisting of noise, are independent of each other because they originate from different instruments. When detecting high-energy gamma-ray photons, photon counters assisted by photomultipliers are employed to measure the counts per second within a specific energy band during a defined time interval as they pass through the metal detectors. The measurement varies depending on the observed burst types. Conversely, in gravitational wave triggers, the goal is to identify coincident signals within multiple interferometric detectors. The coincident time shouldn't deviate by more than

the time it takes for light to travel between the detectors. Additionally, for a detected GW signal to be considered significant, it must exceed a specific signal-to-noise ratio threshold. This significance is determined using a match-filtering technique that compares the signal with predictions derived from theoretical or numerical methods while taking into account the noise in the detectors. As a result, each signal is assigned a statistical rank that classifies it as either signal or noise based on a predetermined threshold.

Filtering of the data from the pipeline is defined by a function $\mathcal{F} : x \rightarrow \mathbb{R}$. The filtered dataset is $\{x_F\} = \{x \mid \mathcal{F}(x) > \mathcal{F}^*\}$. Here, a fixed threshold value, denoted as \mathcal{F}^* , is chosen. The dataset, denoted as $\mathcal{D} = \{x_{gw}, x_\gamma\}$, will undergo individual filtering using specific threshold values, with the filtering process being carried out through specified pipelines. Now, let's consider the modified likelihood under the null hypothesis, taking into account the data processed through filtering. It is as follows:

$$p_{\mathcal{F}}(\mathcal{D}|\mathcal{H}_0) = \int_{\mathcal{F}(\mathcal{D}) > \mathcal{F}^*} p(\mathcal{D}|\mathcal{H}_0) d\mathcal{D}. \quad (3.16)$$

We can rewrite Eq. (3.16) with the introduction of unit step function as follows:

$$p_{\mathcal{F}}(\mathcal{D}|\mathcal{H}_0) = \frac{p(\mathcal{D}|\mathcal{H}_0)\Theta_F(\mathcal{D})}{\int p(\mathcal{D}'|\mathcal{H}_0)\Theta_F(\mathcal{D}') d\mathcal{D}'}, \quad (3.17)$$

where

$$\Theta_F(\mathcal{D}) = \begin{cases} 1 & \text{if } \mathcal{F}(\mathcal{D}) > \mathcal{F}^* \\ 0 & \text{if } \mathcal{F}(\mathcal{D}) \leq \mathcal{F}^*. \end{cases} \quad (3.18)$$

The denominator in the Eq. (3.17) serves as a normalization factor that accounts for the modified probability distribution after applying the filtering condition. The modified probability (or likelihood) of observing the dataset \mathcal{D} under the alternative hypothesis \mathcal{H}_1

and given a set of parameters θ , after applying a filter defined by Θ_F .

$$p_{\mathcal{F}}(\mathcal{D}|\mathcal{H}_1, \theta) = \frac{p(\mathcal{D}|\mathcal{H}_1, \theta)\Theta_F(\mathcal{D})}{P_{det}(\theta)}, \quad (3.19)$$

where

$$P_{det}(\theta) = \int p(\mathcal{D}'|\mathcal{H}_1, \theta)\Theta_F(\mathcal{D}') d\mathcal{D}'. \quad (3.20)$$

Finally, the prior probability distribution of signal parameters θ under the hypothesis \mathcal{H}_1 and the data processed through filtering is given by

$$\pi_F(\theta, \mathcal{H}_1) = \frac{\pi(\theta, \mathcal{H}_1) \cdot P_{det}(\theta)}{\mathcal{Z}}, \quad (3.21)$$

where

$$\mathcal{Z} = \int \pi(\theta', \mathcal{H}_1)P_{det}(\theta') d\theta. \quad (3.22)$$

3.1.3.2 Multimessenger triggers ranking in the high coincidence probability limit

To determine the presence of both a gravitational-wave signal and a gamma-ray burst signal, we consider the individual occurrence rates of these events. Each occurrence can be modeled using a Poisson distribution, assuming constant occurrence rates over time.

The probability of a GW event occurring, denoted by $p(\mathcal{F}(x_{gw}) > \mathcal{F}_{gw}^*)$, where \mathcal{F}_{gw}^* is a threshold, can be calculated using a Poisson distribution with a mean rate \mathcal{R}_{gw} . This mean rate represents the average rate of gravitational-wave events during the observation time \mathcal{T} . Similarly, the probability of a GRB event occurring, $p(\mathcal{F}(x_\gamma) > \mathcal{F}_\gamma^*)$, where \mathcal{F}_γ^* is a threshold, can also be calculated using a Poisson distribution with a mean rate \mathcal{R}_γ during the same observation time. To understand the correlation between GW events and GRB events, one can analyze the joint occurrence rates using their respective Poisson distributions.

The probability that both a gravitational wave event and a gamma-ray burst event are

not present within the observation time is given by, i.e., the product of the individual false alarm probabilities. We write: $p(\mathcal{F}(x_{gw}) > \mathcal{F}_{gw}^*) = \int_{\mathcal{F}_{gw}^*}^{\infty} p_{\mathcal{F}}(f|x_{gw}) df$. Here, f is a variable representing the range of possible values that $\mathcal{F}(x_{gw})$ can take.

The equality $p(\mathcal{F}(x_{gw}) > \mathcal{F}_{gw}^*) = (1 - \mathcal{P}(0, \lambda))$ holds in the limit where:

- The false alarm probability (FAP) matches the probability of at least one event occurring in a Poisson process.
- This happens when \mathcal{F}_{gw}^* is set such that the integral of the probability density function above this threshold equals the probability of one or more events in the Poisson distribution.

Mathematically, this occurs when:

$$\int_{\mathcal{F}_{gw}^*}^{\infty} p_{\mathcal{F}}(f|x_{gw}) df = 1 - e^{-\lambda}$$

where $e^{-\lambda}$ is the probability of zero events in a Poisson distribution with mean λ . Hence, the occurrence of rare events is given by the complement of the probability of having zero events.

$$\begin{aligned} p(\mathcal{D}|\mathcal{H}_{nm}) &= p(\mathcal{F}(x_{gw}) > \mathcal{F}_{gw}^* \wedge \mathcal{F}(x_{\gamma}) > \mathcal{F}_{\gamma}^* | \mathcal{H}_{nm}), \\ &= p(\mathcal{F}(x_{gw}) > \mathcal{F}_{gw}^*) \cdot p(\mathcal{F}(x_{\gamma}) > \mathcal{F}_{\gamma}^*), \\ &= (1 - e^{-\mathcal{R}_{gw} \cdot \mathcal{T}}) \cdot (1 - e^{-\mathcal{R}_{\gamma} \cdot \mathcal{T}}), \\ &\approx (\mathcal{R}_{gw} \cdot \mathcal{T}) \cdot (\mathcal{R}_{\gamma} \cdot \mathcal{T}), \end{aligned} \tag{3.23}$$

with $\mathcal{R} \cdot \mathcal{T} \ll 1$. In the third line of Eq. (3.23), we used the FAP relation given by:

$$\begin{aligned}
FAP &= 1 - \mathcal{P}(0, \lambda), \\
&= 1 - \frac{e^{-\lambda} \cdot \lambda^0}{0!}, \\
&= 1 - e^{\frac{-\mathcal{T} \cdot \mathcal{N}(\mathcal{F}^*)}{\mathcal{T}_{bkg}}}, \\
&= 1 - e^{-\mathcal{R} \cdot \mathcal{T}},
\end{aligned} \tag{3.24}$$

where $\lambda = \mathcal{R} \cdot \mathcal{T}$ is the mean rate for the Poisson distribution, defined as $\mathcal{P}(k, \lambda) = \frac{e^{-\lambda} \cdot \lambda^k}{k!}$, $\mathcal{N}(\mathcal{F}^*)$ counts the triggers passing a certain threshold value, and \mathcal{T}_{bkg} represents the duration of the noise data.

For the coincident signals, we expand Eq. (3.9) as follows (Ashton et al., 2018):

$$\begin{aligned}
p(x_{gw}, x_\gamma | \mathcal{H}^c) &= \int_{\Theta^S} p(x_{gw}, x_\gamma | \theta, \mathcal{H}^c) p(\theta | \mathcal{H}^c) d\theta, \\
&= \int_{\Theta^S} p(x_{gw} | x_\gamma, \theta, \mathcal{H}^c) p(x_\gamma | \theta, \mathcal{H}^c) p(\theta | \mathcal{H}^c) d\theta, \\
&= \int_{\Theta^S} p(x_{gw} | \theta, \mathcal{H}^c) p(x_\gamma | \theta, \mathcal{H}^c) p(\theta | \mathcal{H}^c) d\theta, \\
&= \int_{\Theta^S} \frac{p(x_{gw} | \mathcal{H}^c) p(\theta | x_{gw}, \mathcal{H}^c)}{p(\theta | \mathcal{H}^c)} \cdot \frac{p(x_\gamma | \mathcal{H}^c) p(\theta | x_\gamma, \mathcal{H}^c)}{p(\theta | \mathcal{H}^c)} \cdot p(\theta | \mathcal{H}^c) d\theta, \\
&= p(x_{gw} | \mathcal{H}^c) p(x_\gamma | \mathcal{H}^c) \int_{\Theta^S} \frac{p(\theta | x_{gw}, \mathcal{H}^c) p(\theta | x_\gamma, \mathcal{H}^c)}{p(\theta | \mathcal{H}^c)} d\theta, \\
&= p(x_{gw} | \mathcal{H}^c) p(x_\gamma | \mathcal{H}^c) \mathcal{I}_\theta(x_{gw}, x_\gamma).
\end{aligned} \tag{3.25}$$

In the second step, conditional independence between x_{gw} and x_γ given θ was applied. This allowed us to reexpress the joint probability $p(x_{gw}, x_\gamma | \theta, \mathcal{H}^c)$ as the product of the conditional probabilities $p(x_{gw} | \theta, \mathcal{H}^c)$ and $p(x_\gamma | \theta, \mathcal{H}^c)$. In the fourth step, we used Bayes' theorem to express the conditional probabilities $p(x_{gw} | \theta, \mathcal{H}^c)$ and $p(x_\gamma | \theta, \mathcal{H}^c)$ in terms of the posterior distributions $p(\theta | x_{gw}, \mathcal{H}^c)$ and $p(\theta | x_\gamma, \mathcal{H}^c)$.

Here, the posterior overlap integral $\mathcal{I}_\theta(x_{gw}, x_\gamma)$ measures the level of concurrence between the independent posterior distributions of θ . This integral accounts for the prior

distribution, establishing a reference scale for evaluating the extent of overlap. Our focus will be on identifying the spatial and temporal correlations between the datasets originating from both signals.

$$p(\mathcal{H}_0|\mathcal{D}) \approx \frac{p(\mathcal{D}|\mathcal{H}_{nn})\pi(\mathcal{H}_{nn})}{p(x_{gw}|\mathcal{H}^c)p(x_\gamma|\mathcal{H}^c)\mathcal{I}_\theta(x_{gw}, x_\gamma)\pi(\mathcal{H}^c)}, \quad (3.26)$$

ignoring contributions from (\mathcal{H}_{sn}) and (\mathcal{H}_{ns}) hypotheses probabilities. Now, we will simplify the overlap integral using the spatial and temporal correlation of the GW and GRB triggers for preliminary analysis.

Following (Ashton et al., 2018), the prior $p(\mathcal{H}_{nn}) \equiv \pi(\mathcal{H}_{nn})$ can be expanded into $\mathcal{R}_{gw}\mathcal{R}_\gamma\mathcal{T}^2$ and $p(\mathcal{H}^c) \equiv \pi(\mathcal{H}^c) = \mathcal{R}_{gw,\gamma}\mathcal{T}$. Also, $\mathcal{I}_{t_c} = \frac{\mathcal{T}}{\Delta t}$. Hence, using Eq. (3.25) and Eq. (3.26) in Eq. (3.13), we write:

$$\begin{aligned} p(\mathcal{H}_0|\mathcal{D}) &= \frac{p(\mathcal{D}|\mathcal{H}_{nn})\mathcal{R}_{gw}\mathcal{R}_\gamma\mathcal{T}^2}{p(x_{gw}|\mathcal{H}^c)p(x_\gamma|\mathcal{H}^c)\mathcal{I}_\Omega(x_{gw}, x_\gamma)\mathcal{I}_{t_c}\mathcal{R}_{gw,\gamma}\mathcal{T}}, \\ &= \frac{p(\mathcal{D}|\mathcal{H}_{nn})\mathcal{R}_{gw}\mathcal{R}_\gamma\Delta t}{p(x_{gw}|\mathcal{H}^c)p(x_\gamma|\mathcal{H}^c)\mathcal{I}_\Omega(x_{gw}, x_\gamma)\mathcal{R}_{gw,\gamma}}. \end{aligned} \quad (3.27)$$

Here, $\Omega = (RA, DEC)$. Eq. (3.27) with the filtering can be written as:

$$p_{\mathcal{F}}(\mathcal{H}_0|\mathcal{D}) = \frac{\int p(\mathcal{D}|\mathcal{H}_{nn})\Theta_{\mathcal{F}}(\mathcal{D})}{\int p(\mathcal{D}'|\mathcal{H}_{nn})\Theta_{\mathcal{F}}(\mathcal{D}')d\mathcal{D}'} \cdot \mathcal{R}_{gw}\mathcal{R}_\gamma\mathcal{T}^2}{\int p(\mathcal{D}'|\mathcal{H}^c)\Theta_{\mathcal{F}}(\mathcal{D}')}{\int p(\mathcal{D}'|\mathcal{H}^c)\Theta_{\mathcal{F}}(\mathcal{D}')d\mathcal{D}'} \cdot \mathcal{R}_{gw,\gamma}\mathcal{T}}. \quad (3.28)$$

Finally, we are left with the simplified relation:

$$p_{\mathcal{F}}(\mathcal{H}_0|\mathcal{D}) \approx \frac{p(\mathcal{D}|\mathcal{H}_{nn})\mathcal{R}_{gw}\mathcal{R}_\gamma\Delta t}{p(x_{gw}|\mathcal{H}^c)p(x_\gamma|\mathcal{H}^c)\mathcal{I}_\Omega(x_{gw}, x_\gamma)\mathcal{R}_{gw,\gamma}}. \quad (3.29)$$

\mathcal{R}_{gw} depends on the sensitivity of the detectors and observation time. \mathcal{R}_γ is the unique GRB detection rate per year by participating EM facilities, i.e., approximately 310 GRBs per year. $\mathcal{R}_{gw,\gamma}$ up to 1 yr^{-1} has been explored with existing and future GW and EM facilities by Bhattacharjee et al. (2024). This rate was also investigated following the joint

detections GW170817-GRB170817A (Howell et al., 2019). Δt is described in detail in Table 3.1, and \mathcal{I}_Ω is introduced from Bayesian analysis. Now, we can conduct a comprehensive analysis to determine the posterior probability of the null hypothesis, considering both threshold and sub-threshold limits using Eq. (3.29). In addition, the signal posterior probability can be feasibly calculated by subtracting the null posterior probability from 1. We can explore variations by adjusting the threshold values when ranking the triggers from each dataset, both increasing and decreasing them. Once we have derived the null posterior probability, we can use it to calculate the false alarm probability. The false alarm probability represents the likelihood of claiming a detection when there is no actual signal present.

We have presented the formalism for ranking joint triggers and testing various hypotheses using Bayesian analysis. While operating in low-latency multi-messenger analysis, such calculations incur higher computational costs and latency but would provide a more robust measure to classify multi-messenger signals. This will be explored in detail in future work.

In the upcoming section, we will present the frequentist method of ranking joint triggers in real-time using FAR statistics. If the events being considered are independent and occur at a constant average rate, the number of coincidences within a given time interval Δt will generally follow a Poisson distribution. The Poisson distribution is characterized by its parameter λ , which is the average number of events in the interval Δt .

3.2 The RAVEN pipeline

Since there are several algorithms to classify a GW candidate once it is detected—whether it is simply noise or an astrophysical candidate, and furthermore, if it is astrophysical, whether the signal is from the coalescence of neutron star binaries, neutron star-black hole binaries or black hole binaries (Fong, 2018; Kapadia et al., 2020; Banagiri et al., 2023; Ewing et al., 2024). In addition, there are algorithms to quantify the probability of remnant

properties (Chatterjee et al., 2020; Berbel et al., 2024), suggesting that gravitational wave transients have a probability of producing EM signals. All these are useful for making a more informed decision on whether to follow up such a GW candidate using electromagnetic observations, but they suffer from uncertainty in the skymap location provided in the GW candidate’s detection alert information since GW transients usually have large skymap area (Abbott et al., 2020b, 2021b; Abac et al., 2024).

Similarly, if high-energy astrophysical transients could be detected by EM observations and/or if preliminary source classification and skymap location were estimated, it would be possible to correlate such electromagnetic transients with GW transients to make more informed decisions for rapid follow-up. This is because the collapse of massive stars and compact binary coalescences involving neutron stars produce multi-messenger signals and a plethora of physical processes that are yet to be understood. Higher confidence would result from a reduced skymap area to search, thanks to signal triangulation by participating EM facilities (Connaughton et al., 2017; Goldstein et al., 2017b; Savchenko et al., 2017b; Svinkin et al., 2017), motivating joint association considerations.

Such a multi-messenger signals’ correlation significance is to be analyzed using the aid of notices provided by astronomers all over the world and with the gravitational wave candidate database. A search pipeline called RAVEN, derived from Rapid On-Source VOEvent Coincident Monitor, is a multi-messenger data analysis pipeline operating in low-latency to search for gamma-ray bursts and neutrinos coincident with gravitational-wave signals. The design of RAVEN, described in Urban (2016), was implemented prior to the second observing run of the LIGO-Virgo Collaboration. RAVEN identified the coincidence between GW170817 and GRB170817A within a few seconds, alerting LVK scientists⁷. This marked the beginning of multi-messenger astronomy involving gravitational waves and gamma-ray bursts (Collaboration et al., 2017; Abbott et al., 2017d).

Several enhancements were made to the analysis involving skymaps, workflow, and

⁷<https://gracedb.ligo.org/events/view/G298048>

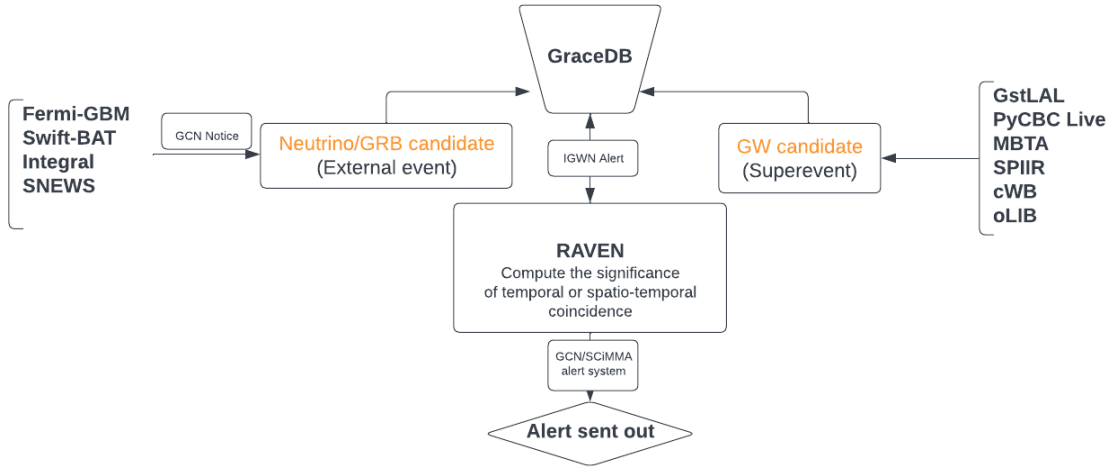


Figure 3.1: Workflow of the Multi-Messenger Signals Detection and Alert System Used by the LIGO-Virgo-KAGRA Collaboration: Both the GW candidate and EM counterpart information are uploaded/ingested to the database, GraceDB. A few tasks are set up to listen and parse information every time a new detection is reported. This allows the RAVEN software to successfully query for neighbors correlating in time and skymap.

the addition of new EM instruments in the searches was reported in Cho (2019) and Piotrkowski (2022) respectively to increase the joint detection. All these changes were made in preparation of the LVK Collaboration’ third observing run (O3).

In preparation for O4, as reported in Piotrkowski (2022), improvements were implemented including searches involving low-significance GRBs and GWs, latency reduction in computing joint trigger significance (incorporating multi-ordered coverage skymaps), and enhanced significance ranking of joint triggers using simulations.

3.2.1 Pipeline description including recent improvements

This subsection describes the pipeline and analysis for a single EM-GW search.

The diagram shown in 3.1 illustrates the workflow for detecting and analyzing gravitational wave and external astrophysical events, such as neutrino or gamma-ray bursts. GW candidates are uploaded to the Gravitational-wave Candidate Event Database (GraceDB)⁸. Concurrently, external events are monitored by instruments such as Fermi-GBM, Swift-

⁸<https://dcc.ligo.org/LIGO-T1400365/public>

BAT, and the Supernova Early Warning System (SNEWS)⁹ (Antonioli et al., 2004), which report detections via GCN.

The RAVEN pipeline first queries GraceDB using the International Gravitational-Wave Observatory Network (IGWN) alert listener¹⁰ to check if coincident candidates are available as soon as a GW candidate or external event candidate is uploaded or created in the database and assigned an event ID starting with ‘E’. For example, E965514 as shown in Fig. 3.4. It then computes the significance of temporal coincidences between these events. If skymap localization information is available for joint association, spatio-temporal significance is computed. Upon validation, alerts are disseminated through the GCN and the Scalable Cyberinfrastructure to support Multi-Messenger Astrophysics (SCiMMA) alert producer system. All these tasks are queued and clustered, utilizing annotation, orchestration, and dissemination of public alerts concerning LVK detections of GW and associated data products. These tasks are performed using the `GWcelery`¹¹ software application built on open-source tools. Refer to the documentation¹² for more details.

For real-time ranking of GW candidates and their associated EM counterparts, we consider the ranking statistic, coincident false alarm rate (FAR_c), based on the significance of the signals. We consider independent GW and EM candidates, such as GRBs, with higher statistical significance. However, GWs can be of very low significance. The following equation is used, motivated by the derivation presented in subsection 3.1.3:

$$FAR_c = FAR_{gw} \frac{R_{grb} \Delta t}{I_\Omega}, \quad (3.30)$$

where FAR_{gw} is the FAR of the GW candidate detected by low-latency CBC or Burst algorithms, R_{grb} is the cumulative rate of unique GRB candidates from participating EM signal detectors detected in a year, Δt is the coincident time window of the GW-GRB

⁹<https://snews.bnl.gov>

¹⁰<https://igwn-alert.readthedocs.io/en/latest/>

¹¹<https://git.ligo.org/emfollow/gwcelery>

¹²<https://rtd.igwn.org/projects/gwcelery/en/latest/>

signal based on the astrophysical time delays between the two signals' emission, and I_Ω is the sky map overlap integral introduced in subsection 3.1.3.

For low-significance GRBs, we respond to processed data from GRB detection algorithms, provided the search is around any (low or high-significance GW) detection time. As a result, the joint coincident FAR for the low-significance search method, accounting for higher false alarms due to noise-noise coincidences, is calculated as:

$$FAR_c = \frac{Z}{I_\Omega} \left(1 + \ln \left(\frac{Z_{max}}{Z} \right) \right), \quad (3.31)$$

where Z is the joint ranking statistic defined as:

$$Z = FAR_{gw} FAR_{grb} \Delta t. \quad (3.32)$$

The max Z value is calculated using the maximum GW and GRB FAR thresholds. These values are discussed in Section 3.3 and are also listed here¹³.

For the skymap overlap integral computation, as derived in Eq. (3.25), we use the following relation:

$$I_\Omega(x_{gw}, x_\gamma) = \int \frac{p(\Omega|x_{gw}, \mathcal{H}_{gw}^s) p(\Omega|x_\gamma, \mathcal{H}_\gamma^s)}{p(\Omega|\mathcal{H}^s)} d\Omega. \quad (3.33)$$

We have two methods to incorporate the skymap in calculating the skymap overlap integral (I_Ω):

In the Hierarchical Equal Area isoLatitude Pixelization (HEALPix) method, the sky map overlap integral is calculated as:

$$I_\Omega(x_{gw}, x_{grb}) = N_{pix} \sum_{i=0}^{N_{pix}} P(i|x_{gw}, \mathcal{H}_{gw}^s) \cdot P(i|x_\gamma, \mathcal{H}_\gamma^s), \quad (3.34)$$

¹³https://git.ligo.org/emfollow/gwcelery/-/blob/7282c415bb64f94c76758de65a64e3fc9835588d/gwcelery/conf/__init__.py#L449-458

where N_{pix} is the number of pixels in a skymap.

In the Multi-Ordered Coverage (MOC) method, we use the RA and DEC of the given pixel Ω_i to match pixels of MOC skymaps and calculate the overlap integral as:

$$I_{\Omega}(x_1, x_2) = 4\pi \sum_{i_1}^{N_{pix}} p(\Omega_1(i_1)|x_1, \mathcal{H}^s) \cdot p(\Omega_1(i_1)|x_2, \mathcal{H}^s) \cdot \Delta A(i_1), \quad (3.35)$$

where $p(\Omega_1(i)|x_a, \mathcal{H}^s)$ is the normalized probability density such that $\sum_i p(\Omega_1(i)|x_a, \mathcal{H}^s) \Delta A = 1$.

The UNIQ ordering system has an advantage over the standard HEALPix system, where equal-area pixels are used. MOC skymaps¹⁴ can increase resolution around the higher probability regions and vice versa, reducing file size. Moreover, we find that using MOC skymaps gives the same result as the HEALPix method but with much lower latency (Piotrkowski, 2022).

Additionally, we evaluate the significance of joint triggers to determine if they meet the alert threshold for public notice. This evaluation primarily considers the significance threshold of the GW candidate, whether it is a CBC or Burst event.

My contributions to the RAVEN pipeline development and testing:

- Some of the GW **Superevents** during the third observing run of the LVK Collaboration (O3) had false alarms related to joint coincidence due to incorrectly assigned search windows. I worked on ensuring that correct filtering was applied for the standard GW-sGRB search time window for CBC candidates and the GW-IGRB search time window for Burst candidates.
- Enable the RAVEN pipeline to participate in the O3 Replay **Superevents** by creating external events to be tested in the GraceDB Playground Server¹⁵.
- Added functionality to manually establish joint coincidences, triggering `RAVEN_ALERT`

¹⁴https://emfollow.docs.ligo.org/userguide/tutorial/multiorder_skymaps.html

¹⁵<https://gracedb-playground.ligo.org>

workflow if such coincidences are missed in the immediate online searches. This feature was added to the web version¹⁶ of the `GWcelery` application.

- Developed criteria to differentiate between sub-threshold GRBs and threshold GRBs when both types coincide with `GW Superevent`.
- Corrected the miscollation of INTEGRAL events in the O3 Replay `GW Superevents`.
- Prevent external event from switching `superevents`.
- Only plot the skymap overlap with the preferred external event when `RAVEN_ALERT` label is applied.
- Prevent the repetition of the skymap comparison pipeline with secondary flattened skymaps.
- Fix the repetition of the log message indicating that `RAVEN_ALERT` publishing criteria are met.
- Add a minimum resolution requirement for external sky maps.
- Fix the bug to update external sky maps with the latest GCN information.
- Rerun the RAVEN skymap comparison whenever the preferred gravitational-wave events, or `G-events` changes.
- Move RAVEN tasks to the main worker and make GCN ingestion sequential.
- Fix the HTTP error raised while retrieving Fermi GRBs skymaps.
- Contributed to the workflow for multi-order GRB skymaps.
- Filter Burst-BBH `superevents` from SNEWS coincidence searches.

¹⁶<https://emfollow.ligo.caltech.edu/gwcelery/>

- Ingestion of SVOM ECLAIRS notices into the Low Latency Alert Infrastructure (LLAI) workflow (ongoing).

In addition, one can run the coincidence searches and ranking on a personal machine (offline) using the stand-alone software application `ligo-raven`¹⁷, to which I also contributed, as well as to the documentation¹⁸.

3.2.2 Implementation for multiple EM detectors

Search	Pipeline(s)	Significant GRB	Low-significant GRB
CBC-GRB	Fermi/GBM	[-1 s, +5 s]	[-1 s, +11 s]
	<i>Swift</i> /BAT	[-1 s, +5 s]	[-10 s, +20 s]
	INTEGRAL	[-1 s, +5 s]	N/A
GW Burst-GRB	Fermi/GBM	[-60 s, +600 s]	[-1 s, +11 s]
	<i>Swift</i> /BAT	[-60 s, +600 s]	[-10 s, +20 s]
	INTEGRAL	[-60 s, +600 s]	N/A
GW Burst-Neutrino	SNEWS	[-10 s, +10 s]	N/A

Table 3.1: The current implementation of the low-latency multi-messenger search pipeline uses coincident time windows, measured in seconds, chosen based on the search and pipeline parameters, and centered on the GW merger/burst time.

The table 3.1 outlines the coincident time windows used in searches for GW and associated GRBs or neutrino signals. These time windows are based on the type of search and the instruments involved, with each window centered around the GW merger or burst time and are estimated with astrophysical processes.

In a CBC-GRB search, the time windows for significant GRBs detected by Fermi/GBM, Swift/BAT, and INTEGRAL are from -1 second to +5 seconds relative to the GW event. For low-significance GRBs, the time windows are wider: -1 second to +11 seconds for Fermi/GBM, -10 seconds to +20 seconds for Swift/BAT, and there is no window for low-significance GRBs detected by INTEGRAL as these are not processed.

¹⁷<https://pypi.org/project/ligo-raven/>

¹⁸<https://ligo-raven.readthedocs.io/en/latest/index.html>

For the GW Burst-GRB search, which targets GRBs associated with core-collapse supernovae, the time windows are broader. Significant GRB time windows for Fermi/GBM, Swift/BAT, and INTEGRAL span from -60 seconds to +600 seconds. For low-significance GRBs, the time windows are from -1 second to +11 seconds for Fermi/GBM, -10 seconds to +20 seconds for Swift/BAT, and there is no window for INTEGRAL. Here, lower time windows search with subthreshold GRBs were chosen in order to avoid noise contamination, and are arbitrary.

In the GW Burst-Neutrino search, the time window for significant neutrino signals detected by SNEWS is from -10 seconds to +10 seconds relative to the GW event. There is no window for low-significance neutrino signals in this search.

The choice of time windows reflects the expected delays between GW events and their electromagnetic or neutrino counterparts. Wider windows are used for GW bursts due to uncertainties in delay models for GRBs from supernovae and other progenitors (Zhang, 2019). Slightly wider windows for targeted searches, particularly for Swift, account for models predicting additional delays and leverage Swift’s precise localization to rule out noise events. The SNEWS window is based on the expected time delay caused by the mass of neutrinos emitted from events just outside our galaxy.

These time windows are designed to maximize the chances of detecting coincident signals across different instruments and search pipelines, enhancing the capabilities of multi-messenger astronomy, as shown in detail in flowchart 3.2.

3.2.3 Validation and testing using a Mock-Data-Challenge

Ahead of the fourth observing run (O4) of Advanced LIGO, Advanced Virgo, and KAGRA, several software and alert system enhancements were implemented since the conclusion of O3. To assess these upgrades, a Mock Data Challenge (MDC) was employed, designed to bolster the robustness of the LLAI. This infrastructure was tested on 40 days of replay data, generated with 5×10^4 injected CBC source waveforms, and included data from O3.

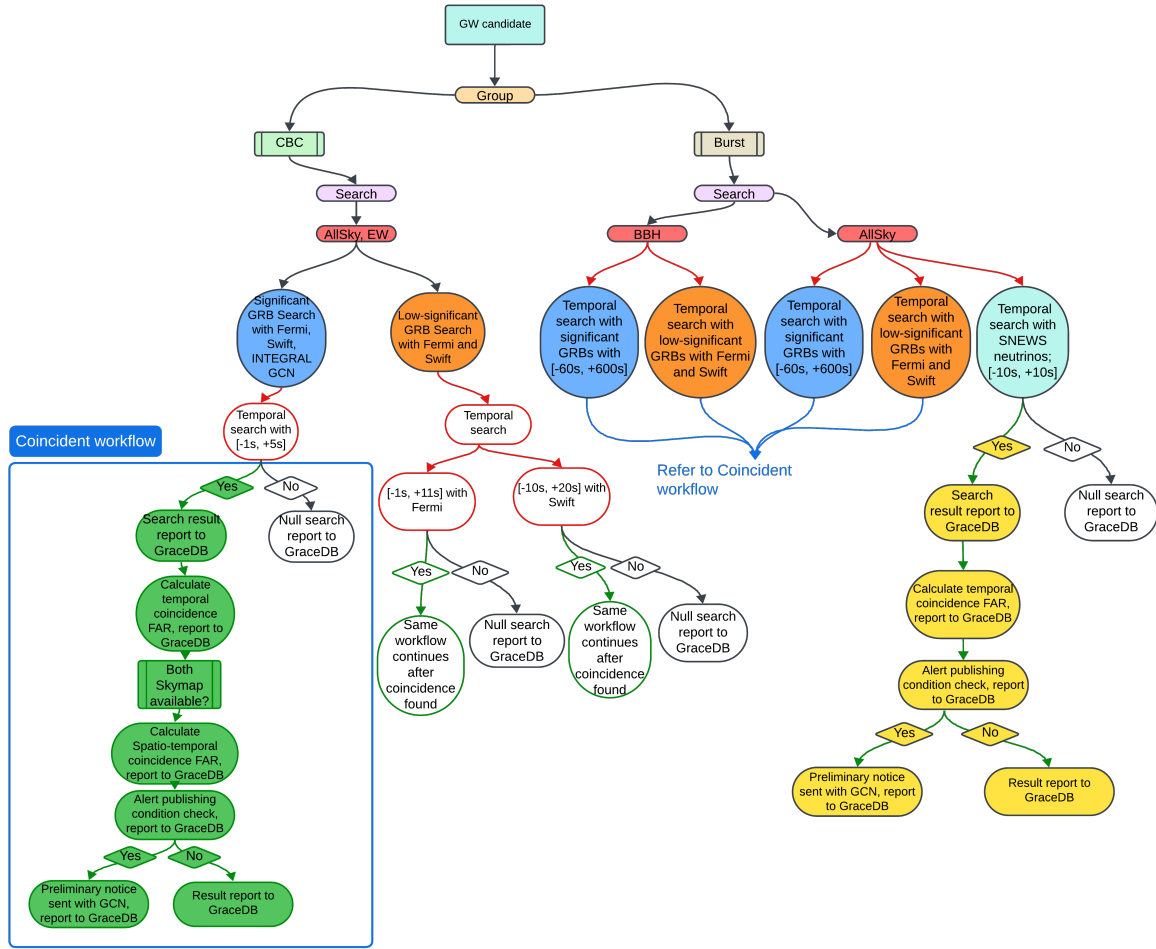


Figure 3.2: Current Implementation of the RAVEN Pipeline with Multiple GW and EM Searches. The flowchart illustrates various GW searches, including AllSky, Early Warning, and Binary Black Hole GW candidates, as well as EM searches for significant and low-significance GRBs and neutrinos. As shown in the flowchart, the coincident workflow remains consistent once a coincidence is identified. However, specific details involving skymaps are not depicted here because, among multiple external coincidences with a GW **Superevent**, one event with improved skymap information may be preferred.

Although this injection rate is greater than anticipated for O4, i.e., $\mathcal{O}(10^2)$, we intentionally designed the injection datasets with a higher rate. This was done to simulate the coincident searches, evaluate the alert system, and assess data products for coordinated follow-up.

Online GW search algorithms were running and uploading the detection candidates during the replay, as the injections were designed to mimic production settings but at a

higher frequency. Although the simulated sources had an SNR threshold ≥ 4 , three LVK detectors would report a detection when a candidate passed a combined SNR of 8.

Once GW candidates were established, we designed an algorithm to simulate the occurrence of external events coinciding with gravitational wave detections generated during the MDC. We generated mock external events, such as significant and low-significant GRBs, simulating alerts from actual observatories like Fermi, Swift, INTEGRAL, or AGILE. These events are formatted as VOEvent XML alerts or Kafka alert packets, depending on the external trigger pipeline and searches.

The tests involved examining the detection efficiency of real-time low-latency coincident searches, computing joint coincidence statistics, and determining the combined sky map localization accuracy for the RAVEN pipeline as it assisted in stress testing the pipeline.

Compact Object Properties					
Binary Type	Object	m/M_{\odot} (min/max)	m dist.	Max a	a dist.
BNS	Primary	1.0 - 2.05	Unif.	0.4	Unif. & isotropic
	Secondary	1.0 - 2.05	Unif.	0.4	Unif. & isotropic
NSBH	Primary	1.0 - 60.0	m^{-1}	0.998	Unif. & isotropic
	Secondary	1.0 - 2.05	Unif.	0.4	Unif. & isotropic
BBH	Primary	2.05 - 100	$m^{-2.35}$	0.998	Unif. & isotropic
	Secondary	2.05 - 100	m^1	0.998	Unif. & isotropic

Table 3.2: The component masses (m) and spins (a) distribution of binary systems were used in the injection sample for the O3 Replay MDC (Chaudhary et al., 2024). However, the LVK collaboration performs searches in higher mass ranges, up to $3 M_{\odot}$ for neutron stars (Ewing et al., 2024).

Out of 50,000 GW events used for our campaign as shown in Figure 3.3, 4,514 GW injections were recovered by the detection pipelines. These were 1,489 BNS, 1,105 NSBH, and 1,920 BBH events. We then designed a process to create mock GRB events from four participating EM facilities by providing time offsets using astrophysical scenarios and randomly adjusting skymap offsets. We decided to generate a GRB event using the EM facilities’ provided GCN notice template only for every 10th GW candidate. The assigned probabilities for the GRB belonging to Fermi, Swift, INTEGRAL, and AGILE were 0.5, 0.3, 0.1, and 0.1, respectively. In addition, significant (“GRB”) and low-significance GRBs

(“SubGRB” and “SubGRBTargeted”) were assigned probabilities of 0.6, 0.1, and 0.3, respectively.

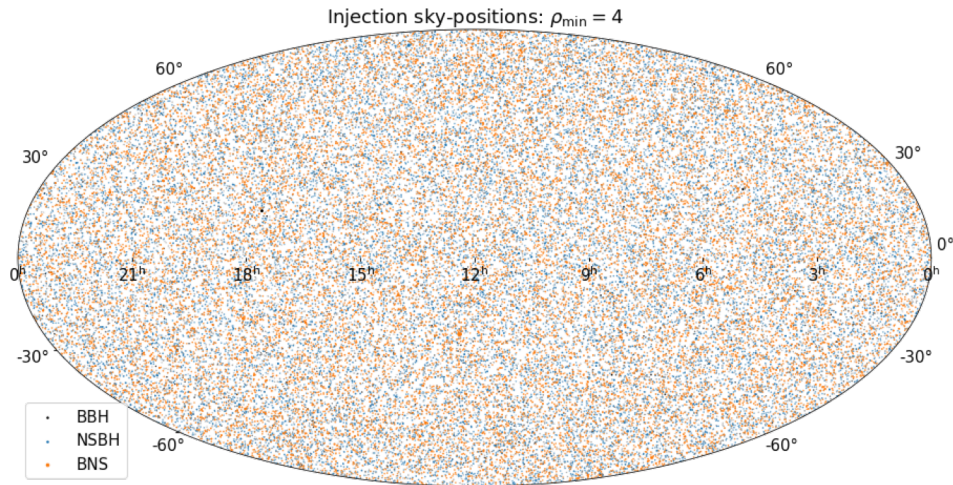


Figure 3.3: Sky distribution of simulated gravitational wave events from different types of compact binary coalescences: binary black hole (BBH) mergers, neutron star-black hole (NSBH) mergers, and binary neutron star (BNS) mergers. The map shows the positions of 50,000 simulated events uniformly distributed across the sky, with BBH events marked by black dots, NSBH events marked by blue dots, and BNS events marked by orange dots. Credit: S. Ghosh, reproduced with permission.

From low-latency analyses, we found that 469 multi-messenger coincidences were recorded in our simulation, with GRB candidates coinciding at times surrounding the GW injections. For these coincidences, an `EM_COINC` label was assigned to the GW candidate. We found that only 356 of these joint candidates passed the joint coincidence alert publishing conditions, triggering a `RAVEN_ALERT` label that surpassed the significant FAR threshold of 1 per month¹⁹.

We find that, with our simulation framework using O3 Replay GW `Superevents`, a coincidence with a mock GRB has been found, triggering an `EM_COINC` label and a `RAVEN_ALERT` for those joint coincidences passing a set FAR threshold value and publishing conditions. The latency for such joint coincidences was found to be 32.9 seconds for the 50th percentile for the time difference between the mock electromagnetic counterpart coincidence

¹⁹Refer to <https://emfollow.docs.ligo.org/userguide/analysis/index.html#alert-threshold> for more details.

and the GW `Superevent`, while the time difference for the `RAVEN_ALERT` condition is 35.3 seconds. For the median (90%), these latency measures are 44.4 seconds and 48.4 seconds, respectively.

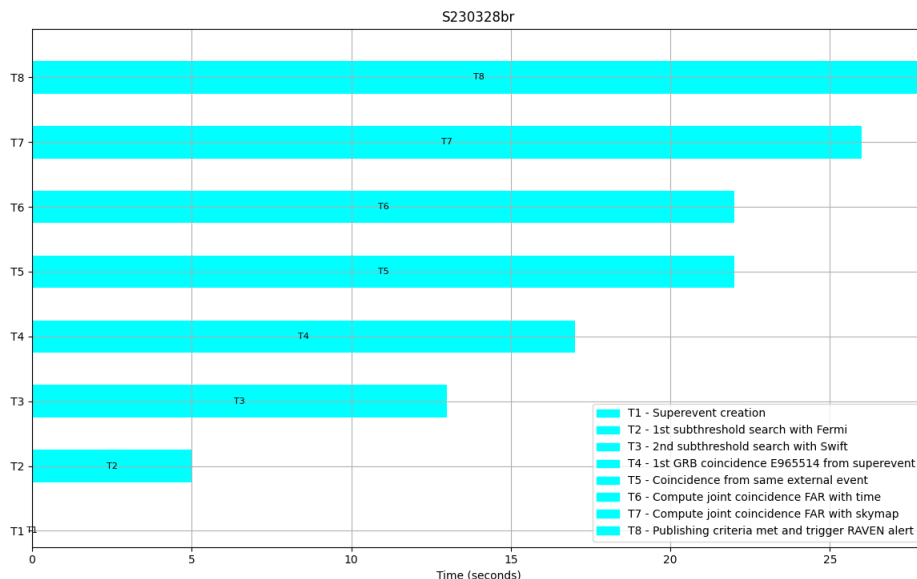


Figure 3.4: Representative GW candidate from O3 Replay MDC data testing for the RAVEN pipeline. The timeline shows various stages (T1 to T8) involved in the process for candidate S230328br. Each bar represents a different task. The x-axis represents time in seconds, highlighting the cumulative duration of each task after the GW `Superevent` creation.

3.3 Results from O4a

O4a started on May 24, 2023, following the successful completion of Engineering Run 15²⁰, and concluded on January 16, 2024. GW `Superevents` were uploaded following CBC and Burst search algorithm triggers with respective FARs of 2 per hour for CBC and 0.5 per hour for Burst²¹. Querying the GraceDB server, a total of 13,773 GW `Superevents` were processed to check the performance of the RAVEN pipeline search results. During the

²⁰<https://dcc.ligo.org/LIGO-G2300834/public>

²¹These values are used in s^{-1} while computing the joint significance.

observing run, there were **G-events** uploaded from searches other than CBC and Burst that were not assigned to **GW Superevents**. Additionally, due to the downtime of the LLAI system and/or operating sites, the number of **GW Superevents** during the observing run could be fully explained in accordance with the upload rates.

A significant number of GRBs were reported to GraceDB. There were 206 significant GRBs, with 158 detected by Fermi, 35 by Swift, 10 by INTEGRAL, and 3 by AGILE. Additionally, there were 17 SubGRB events and 2,395 SubGRBTargeted events detected by Fermi, with 22 of these exceeding the false alarm rate threshold ($FAR_{em,th}$) of Fermi, and 1 Swift SubGRBTargeted event passing the $FAR_{em,th}$ of Swift. The $FAR_{em,th}$ was set at 1×10^{-4} Hz for Fermi and 1×10^{-3} Hz for Swift, establishing the criteria for distinguishing low-significance detections from background noise.

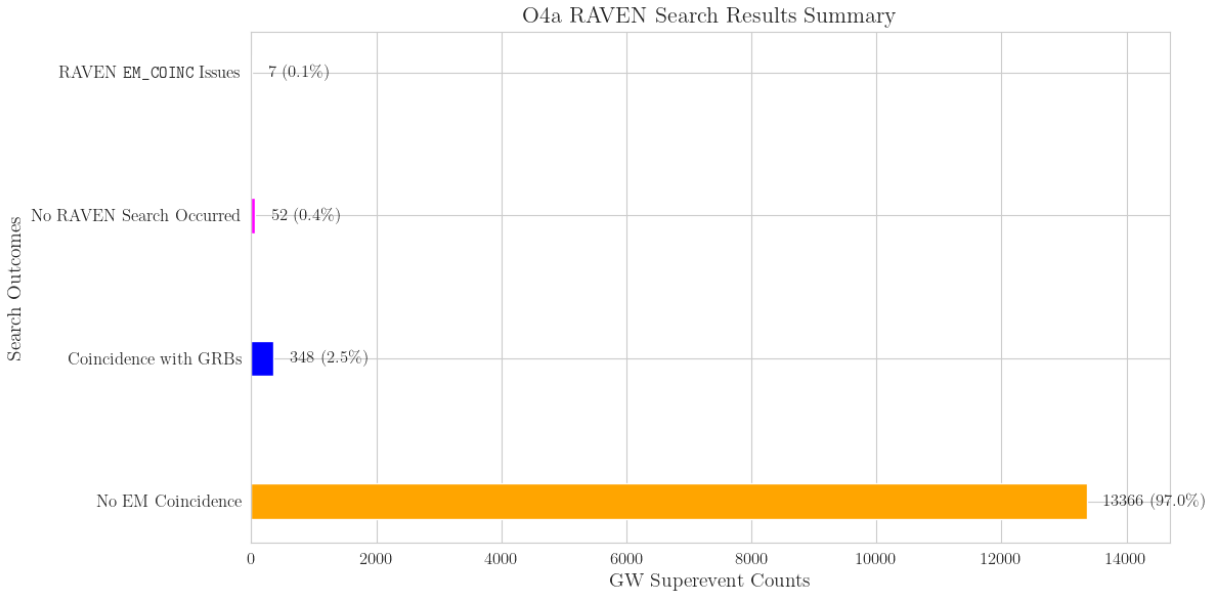


Figure 3.5: Summary of O4a RAVEN Search Results. This bar chart shows the distribution of **GW superevent** counts across various search outcome categories and summarizes the EM follow-up efforts and results for **GW candidates** during the O4a observing run.

We investigated the RAVEN pipeline search performance during the first part of O4, with a summary shown in Figure 3.5. We confirmed that 17,336 out of 17,773 **GW Superevents** (97%) were processed appropriately by the RAVEN pipeline as designed,

as illustrated in Figure 3.2. We found no coincidences reporting null search results to GraceDB corresponding to either significant or low-significance EM search time windows based on astrophysical time delays.

We found that the RAVEN pipeline did not report search results for only 52 GW **Superevents**. Through offline analyses, we accounted for this failed behavior and confirmed that no EM counterparts were observed during the creation time of these GW **Superevents** on GraceDB. These failures were primarily due to memory issues on the main server hosting the LLAI system, where the sequence of GW candidates workflow was either interrupted or didn't progress. For only 2 of the GW candidates (S230610ar and S230805s), the RAVEN pipeline didn't perform a search at all although LLAI system was working.

We also investigated RAVEN `EM_COINC` issues concerning 7 GW **Superevents**. When two GW **Superevents** are reported within search windows with low-significant GRB, the EM event is associated with the GW **Superevent** that has the lower FAR, while the other is reported as having no coincidence. This behavior is intentional, based on the RAVEN pipeline implementation within `GWCelery`, following `ligo-raven` version 3.2²², but such workflow could be changed in the future to rank each coincidence. Below, we provide more details:

- S230825l and S230825k: EM event assigned to S230825k.
- S230918bz: EM event assigned to S230918ca.
- S230811m: EM event assigned to S230811n.
- S230823bt: EM event assigned to S230823bs.
- S231007y: EM event assigned to S231007z.

²²<https://pypi.org/project/ligo-raven/3.2/>

Querying O4a `EM_COINC` on the GraceDB server revealed that out of 350 GW **Superevents**, 2 have issues as discussed below, resulting in 348 coincidences with GRBs. Most of these coincidences resulted from GRB pipeline processing of their data around the GW candidate detection time, after downlinking to the computing sites for analysis. We processed every coincidence for storage and testing of the RAVEN pipeline. We found that while ranking the joint coincidences using low-significance GWs and GRBs using Eq. (3.31), we encountered negative values, which is not meaningful. Also, we found that one of the joint coincidence analyses was incomplete due to the Swift SubGRBTargeted skymap information not being available, causing the `trigger_raven_alert` function to fail.

- S231004f has an associated EM event, E443145, initiated only by an external EM trigger.
- S231007z has an associated EM event, E444163, which is non-astrophysical.

We discovered a few issues while reviewing the O4a RAVEN pipeline search results and have already implemented fixes, as reported here²³.

We found that the GW **Superevents** coincident with significant GRB candidates occurred during a larger temporal window of $[-60\text{s}, +600\text{s}]$, belonging to the Burst group. These joint candidates did not pass the significant alert threshold of $3.17 \times 10^{-8}\text{Hz}$ (i.e., 1 per year), after accounting for the trials factor. Such coincidences occurred approximately once per month. The results summary is presented in Table 3.3 and Figure 3.6.

We also found that the GW **Superevents** coincident with low-significance GRB candidates belonged to both the CBC and Burst groups. **Superevent** S230920ap passed the significant alert threshold for the CBC group of $3.86 \times 10^{-7}\text{Hz}$ (i.e., 1 per month), after accounting for the trials factor. Upon manual checking and in private communication with the Fermi-GBM team, we found that the low-significance GRB candidate was vetoed due to its sky localization occurring in the South Atlantic Anomaly (SAA) region. The results summary is presented in Table 3.4 and Figure 3.8.

²³<https://git.ligo.org/naresh.adhikari/o4a-raven-testing>

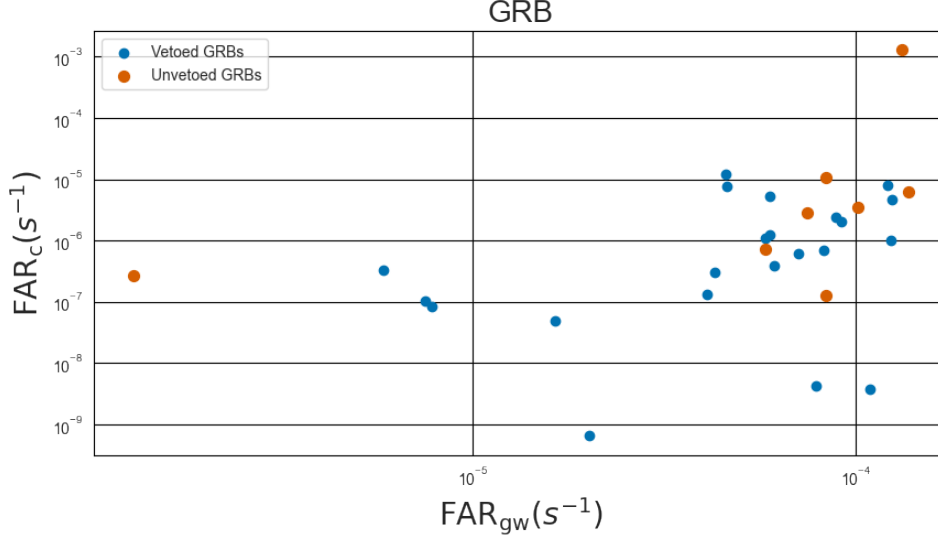


Figure 3.6: Scatter plot showing the ranking of significant GRBs detected in the O4a RAVEN search. The horizontal axis displays the false alarm rate for gravitational waves (FAR_{gw}), while the vertical axis shows the false alarm rate for coincident events (FAR_c) computed using spatio-temporal information as per Eq. (3.30). Blue markers represent GRBs vetoed by the EM instruments, and orange markers represent non-vetoed GRBs. GRB vetoing can happen due to classification and source location changes with the update notices or the satellite’s technical failures.

#	Superevent ID	EM Event ID	GW Group	EM Group	EM Pipeline	FAR_{gw}	FAR_{em}	FAR_c	Observation
1	S230710ak	E416552	Burst	External	Fermi	7.44×10^{-5}	-	3.38×10^{-5}	Alert threshold not met
2	S230805as	E421718	Burst	External	Fermi	1.30×10^{-6}	-	3.19×10^{-6}	Alert threshold not met
3	S230918cf	E439011	Burst	External	Fermi	1.37×10^{-4}	-	7.62×10^{-5}	Alert threshold not met
4	S231014n	E445667	Burst	External	Fermi	8.34×10^{-5}	-	1.26×10^{-4}	Alert threshold not met
5	S231030a	E449825	Burst	External	Fermi	1.01×10^{-4}	-	4.16×10^{-5}	Alert threshold not met
6	S231030i	E449852	Burst	External	Fermi	8.37×10^{-5}	-	1.55×10^{-6}	Alert threshold not met
7	S231123eb	E454845	Burst	External	Fermi	1.32×10^{-4}	-	1.54×10^{-2}	Alert threshold not met
8	S231222m	E460102	Burst	External	Fermi	5.81×10^{-5}	-	8.56×10^{-6}	Alert threshold not met

Table 3.3: Summary of O4a Significant GRB Coincidences. Here, FAR_c is computed using spatio-temporal information as defined in Eq. (3.30) and has a unit of Hz. A time window of $\Delta t = 660$ seconds is used, and a GRB rate (R_{grb}) of 310 per year is assumed. “Alert threshold not met” signifies that these joint coincidences didn’t pass a threshold of 1 per year, i.e., 3.17×10^{-8} Hz.

We are performing simulation studies using low-significance GW and GRB trigger information and sky maps to better understand the coincident FAR in these limits.

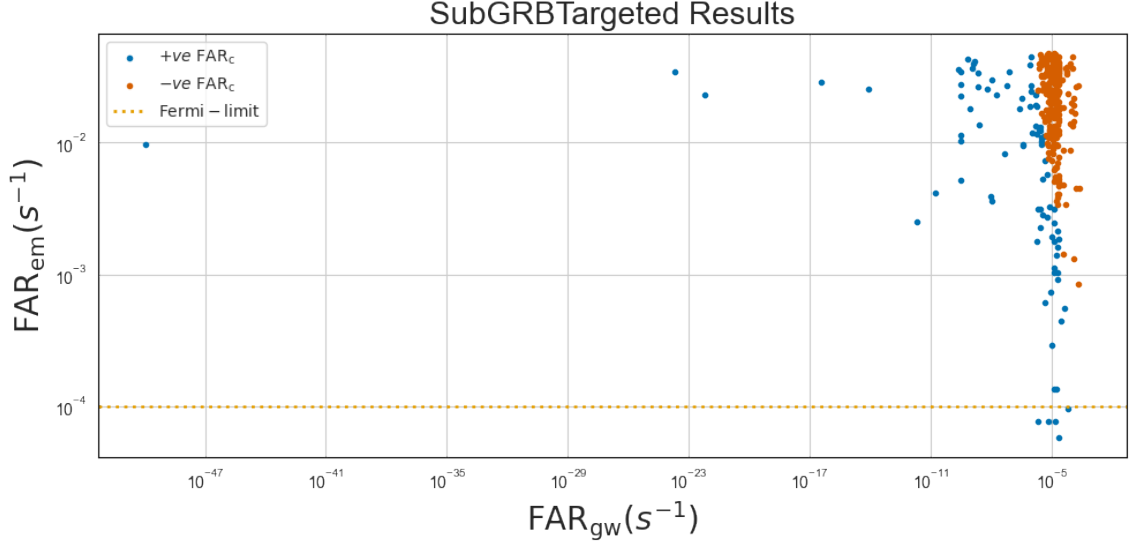


Figure 3.7: SubGRBTargeted Results displaying the relationship between FAR_{em} and FAR_{gw} . Blue and orange points represent positive and negative FAR_c values, respectively, with the Fermi-limit shown as a dashed line. FAR_c is calculated using Eq. (3.31), and negative FAR_c values can be completely disregarded. We used the highest GW FAR (10 per day) and the GRB FAR threshold (8.6 per day), aiding in evaluating potential correlations between low-significance GW and GRB events. We discovered that the highly significant GWs are associated with low-significance GRBs from a Fermi search pipeline that didn't pass $\text{FAR}_{em,th}$.

#	Superevent ID	EM Event ID	GW Group	EM Group	EM Pipeline	FAR_{gw}	FAR_{em}	FAR_c	Observation
1	S230811z	E428470	Burst	External	Fermi	6.41×10^{-6}	7.72×10^{-5}	3.99×10^{-3}	Alert threshold not met
2	S230827az	E433018	Burst	External	Fermi	1.94×10^{-6}	7.72×10^{-5}	6.08×10^{-8}	Alert threshold not met
3	S230903bg	E434978	Burst	External	Fermi	6.37×10^{-5}	9.65×10^{-5}	1.75×10^{-4}	Alert threshold not met
4	S230920ap	E439426	CBC	External	Fermi	1.55×10^{-5}	7.72×10^{-5}	1.85×10^{-7}	RAVEN_ALERT, E439426 was SAA event upon checking
5	S230924bl	E440512	CBC	External	Fermi	2.24×10^{-5}	5.79×10^{-5}	4.58×10^{-4}	Alert threshold not met
6	S231004f	E443145	CBC	External	Swift	2.94×10^{-6}	2.0×10^{-4}	1.17×10^{-7}	External event skymap not avail.

Table 3.4: Summary of O4a Low-Significant GRB Coincidences. Here, FAR_c is computed using spatio-temporal information as defined in Eq. (3.31) and has a unit of Hz. A time window of $\Delta t = 12$ seconds is used for Fermi and 30 seconds for Swift in processing low-significance GRBs. “Alert threshold not met” signifies that these joint coincidences did not pass a threshold of 1 per year, i.e., 3.17×10^{-8} Hz for Burst. RAVEN_ALERT for joint coincidences where the GW belongs to the CBC searches did not pass a threshold of 1 per month, i.e., 3.86×10^{-7} Hz.

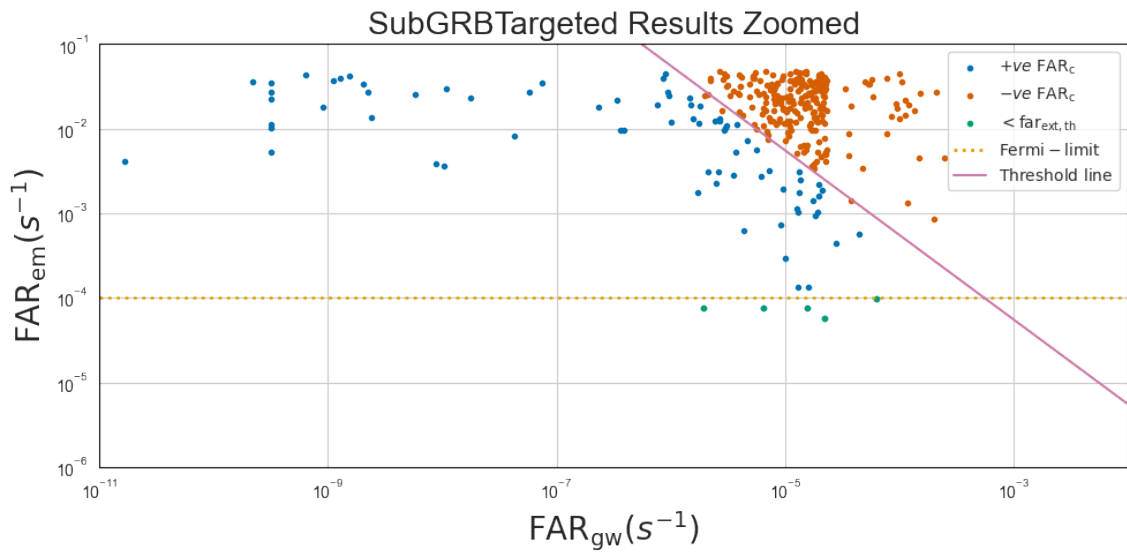


Figure 3.8: SubGRBTargeted Results: FAR Analysis (Zoomed). Green points mark the joint coincidences that consist of low-significance GRBs passing the Fermi-limit, as shown with the yellow dotted line and discussed in detail in Table 3.4. The magenta solid line represents a threshold using the max FAR_{gw} and FAR_{em} values as in Eq. (3.31). Both axes use a logarithmic scale.

Chapter 4

Combining GW and GRB afterglow observations

This chapter is reproduced in part from [Sarin et al. \(2024\)](#), which has been published in the Monthly Notices of the Royal Astronomical Society. An online record can be found at <https://doi.org/10.1093/mnras/stae1238>.

Two neutron stars orbiting each other emit some of their energy as gravitational waves. As they do, they lose energy, causing them to spiral closer together and move at speeds approaching the speed of light. When they get very close, within a few hundred kilometers, the gravitational waves become intense, allowing us to detect them hundreds of millions of light-years away using ground-based laser interferometric detectors ([Abbott et al., 2017f,c](#)). During the late inspiral/merger process, tidal forces deform the neutron stars, which then collide and release ejecta at high velocities. Depending on the mass of the remnant system, there is a possibility of forming a hypermassive neutron star or a black hole ([Friedman & Stergioulas, 2020](#); [Sarin & Lasky, 2021](#)). To conserve angular momentum during the infall of neutron-rich material ([Margalit et al., 2022](#)), a jet is produced, creating a short gamma-ray burst and its afterglow, which can be detected by electromagnetic wave observatories

(e.g., [Hallinan et al., 2017](#); [Lazzati et al., 2018](#); [Lyman et al., 2018](#); [Wu & MacFadyen, 2019](#)).

In brief: GRBs are among the strongest and brightest explosions in the universe, emitting the luminosity of the Sun’s lifetime in a few seconds. There are two types of GRBs: short GRBs and long GRBs. These highly relativistic jets are cosmological in origin, bipolar in nature, and are powered by compact central engines ([Kumar & Zhang, 2014](#); [Zhang, 2018](#); [Burns, 2020](#)).

The model ([Rees & Meszaros, 1994](#)), first developed by Martin Rees and Peter Mészáros in the early 1990s and later detailed ([Sari et al., 1998](#)) by Piran, Sari, and Narayan in the late 1990s, describes the production of GRBs through internal shocks within a relativistic outflow or “fireball” ejected from a central engine. In this model, shells of material with different velocities collide, producing internal shocks that convert kinetic energy to radiation, resulting in the initial burst of gamma rays. This process directly impacts the subsequent afterglow emission. As the fireball expands and interacts with the surrounding medium, it forms an external shock that produces the multi-wavelength afterglow. The energy and Lorentz factor of the fireball, determined during the prompt phase, influence the strength and evolution of the afterglow. Additionally, the composition and structure of the outflow, shaped by the prompt emission mechanism, affect how efficiently the remaining energy is converted into afterglow radiation across a wide range of wavelengths, from radio waves to X-rays.

During O4a (May 23, 2023 - January 16, 2024), the LVK Collaboration detected an interesting GW candidate, GW230529 ([Abac et al., 2024](#)), but it was poorly localized. The non-detection of EM counterparts ([Ronchini et al., 2024](#)) in O4a has redirected our focus to O4b, which started on April 10th, 2024. During O4b, there is a 73% probability of detecting at least one binary neutron star merger event ([emf, 2024](#)) before the run ends in June 2025. Research by [Essick \(2023\)](#); [Ray et al. \(2023\)](#) outlines a detailed analysis of such probability calculations. Additionally, the expected number of discoverable kilonovae

during LVK O4 is 1 to 2, with a 90% confidence limit, as reported by [Shah et al. \(2024\)](#).

Gravitational waveforms, which include both amplitude and phase information, are invaluable for determining various source properties of the binary system such as mass, spin, distance, inclination, sky position, and tidal information ([Yunes et al., 2022](#)). Meanwhile, electromagnetic waves emitted from gamma-ray burst afterglows following the binary coalescence provide additional crucial data, including redshift, sky location, emission energies, and jet models ([O'Connor et al., 2023](#)).

Joint modeling of these multi-messenger signals is essential for a comprehensive understanding of the events. This approach allows us to infer the dynamics of the merger, properties of the resulting remnant and its environment, and to provide independent information on source properties ([Margalit & Metzger, 2017](#); [Radice et al., 2018](#); [Coughlin et al., 2019](#); [Wang et al., 2023](#)). Additionally, joint modeling helps in constraining emission ([Corsi et al., 2024](#)) and jet structure models ([Biscoveanu et al., 2020](#); [Farah et al., 2020](#); [Ronchini et al., 2024](#)), making it a crucial aspect of the analysis.

However, accurately constraining a large number of parameters necessitates Bayesian modeling ([Thrane & Talbot, 2019](#)) that relies on stochastic sampling. As the number of parameters increases, the computational demands of such analyses grow significantly, posing a challenge for real-time and detailed studies. Despite these challenges, the ability to perform joint modeling provides a more holistic view of the events and enhances our understanding of the fundamental processes involved in binary neutron-star mergers and their aftermath. In this chapter, we present such an undertaking through a simulation study.

4.1 Joint inference basics

With the observation of a gravitational-wave signal by the LVK Collaboration and an electromagnetic signal from the afterglow emission, one can break the degeneracies associated

with a single observation alone (Gianfagna et al., 2023; Garcia-Cifuentes et al., 2024).

As afterglow modeling can be intricate across different EM spectra, one might want to test various hypotheses during the investigation. As confirmed by the coalescence of binary neutron stars detected in the gravitational-wave signal GW170817, followed by the prompt gamma-ray emission GRB170817A (Lamb & Kobayashi, 2018) and its afterglow (Wu & MacFadyen, 2019), one can put forward model priors to test jet structure and emission modeling. Hence, there is a desire for an interface to perform swift joint modeling of GRB afterglow parameters in conjunction with gravitational wave signal source parameters.

4.1.1 GW source model

Bayes' theorem is used to estimate the posterior distribution $p(\boldsymbol{\theta}|\{\mathbf{d}_i\})$ of the source parameters $\boldsymbol{\theta}$ based on the data \mathbf{d}_i from multiple detectors. The likelihood function $\mathcal{L}(\{\mathbf{d}_i\}|\boldsymbol{\theta})$ is modeled using a Gaussian-noise likelihood function, where the model signal $\mathbf{h}_i(\boldsymbol{\theta})$ is compared with the data from each detector. The frequency range for BNS signals is typically set between 20 Hz and 1024 Hz, and the non-constant part of the logarithm of the likelihood function is crucial for stochastic sampling during the parameter estimation of GW sources.

4.1.2 GRB afterglow model

The light-curve spectrum, consisting of the top-hat GRB afterglow model (Ryan et al., 2020), involves a few parameters listed in detail below:

t: This parameter represents the time since the GRB event or the jet launch. It is crucial for modeling the evolution of the afterglow and is typically measured in seconds, minutes, or days.

z: The redshift measures how much the wavelength of the light from the GRB has been stretched due to the expansion of the universe. It provides information about the

distance to the GRB provided with Eq. (4.1) and is dimensionless.

$\log_{10} E_0$: The logarithm of the isotropic energy measured in ergs during the prompt emission.

θ_{observer} : This is the angle between the jet axis and the observer's line of sight, also known as the viewing angle. It is measured in radians or degrees.

m_1 : The mass of the first object in the binary system, measured in solar masses (M_{\odot}). This could be a neutron star or black hole.

m_2 : The mass of the second object in the binary system, also measured in solar masses (M_{\odot}), and we require $m_2 \leq m_1$.

f_{fudge} : A factor used in the model to account for uncertainties or to fit the model more accurately to the observed data. It is dimensionless.

θ_c : The half-opening angle of the jet, describing the angular size of the jet's core. It is measured in radians or degrees.

$\log_{10} n_{\text{ism}}$: The logarithm of the number density (cm^{-3}) of the circumburst medium, which affects the interaction of the jet with the surrounding environment.

p : The power-law index of the electron energy distribution, which is crucial for determining the spectrum of the synchrotron emission from the afterglow. It is dimensionless.

$\log_{10} \epsilon_e$: The logarithm of the fraction of the energy in the electrons, which affects the synchrotron emission and thus the afterglow light curve.

$\log_{10} \epsilon_B$: The logarithm of the fraction of the energy in the magnetic field, which also affects the synchrotron emission.

ξ_e : The fraction of electrons that get accelerated. It is dimensionless.

Γ_0 : The initial Lorentz factor of the jet, describing the initial speed of the jet relative to the speed of light. It is critical for determining the dynamics of the jet and is dimensionless.

Using the magnitude of the detected spectrum, we can convert it to flux (Carroll & Ostlie, 2017; Levan, 2018). We assume a flat Λ CDM cosmology to convert redshift to luminosity distance using the following relation:

$$d_L(z) = \frac{c(1+z)}{H_0} \int_0^z \frac{dz'}{\sqrt{\Omega_m(1+z')^3 + (1-\Omega_m)}}, \quad (4.1)$$

where c and Ω_m correspond to the speed of light and matter density, respectively. We consider Λ CDM cosmology with $H_0 = 67.4 \text{ km s}^{-1}\text{Mpc}^{-1}$ and $\Omega_m = 0.315$ as the true cosmology (Aghanim et al., 2020).

The following table 4.1 lists the measurements and techniques for the wavelength of interest for our joint modeling.

Wavelength	Instruments	Measurements & Techniques
X-ray (0.01-10 nm)	Swift XRT, Chandra	Flux, spectrum, light curve analysis, spectroscopy
Radio (mm to m)	VLA, ALMA	Flux at various frequencies, light curve analysis, interferometry, spectral index analysis

Table 4.1: Probes and Techniques for GRB Afterglow Emission with X-ray and Radio Wavelengths (Carroll & Ostlie, 2017; Rhodes et al., 2020; Ronchini et al., 2022; Gianfagna et al., 2023).

The EM likelihood function is given by:

$$\mathcal{L}_{\text{EM}}(d_{\text{EM}}|\boldsymbol{\theta}) \propto \exp(-\chi^2/2), \quad (4.2)$$

where χ^2 is calculated by comparing the flux estimated from the assumed model with parameter $\boldsymbol{\theta}$ to the dataset d_{EM} .

4.1.3 Joint likelihood

We assume that the GW and EM datasets d_{GW} and d_{EM} are independent, and the joint likelihood (Fan et al., 2014; Biscoveanu et al., 2020; Gianfagna et al., 2023) is given by the product of the two likelihoods:

$$\mathcal{L}_{\text{GW+EM}}(d_{\text{GW}}, d_{\text{EM}}|\boldsymbol{\theta}) = \mathcal{L}_{\text{GW}}(d_{\text{GW}}|\boldsymbol{\theta}) \times \mathcal{L}_{\text{EM}}(d_{\text{EM}}|\boldsymbol{\theta}). \quad (4.3)$$

Now, the posterior distribution can be rewritten for the joint parameter inference given by:

$$p(\boldsymbol{\theta}|d_{\text{GW}}, d_{\text{EM}}) \equiv \frac{\mathcal{L}_{\text{GW+EM}}(d_{\text{GW}}, d_{\text{EM}}|\boldsymbol{\theta})\pi_{\text{GW+EM}}(\boldsymbol{\theta})}{\mathcal{Z}_{\boldsymbol{\theta}}}, \quad (4.4)$$

where $\pi_{\text{GW+EM}}(\boldsymbol{\theta})$ is the multi-dimensional prior probability distribution for our parameters of interest. $\mathcal{Z}_{\boldsymbol{\theta}}$ is the Bayesian evidence, obtained by marginalizing the joint likelihood over the GRB and GW parameters, and can be used to compare models:

$$\mathcal{Z}_{\boldsymbol{\theta}} = \int \mathcal{L}_{\text{GW+EM}}(d_{\text{GW}}, d_{\text{EM}}|\boldsymbol{\theta})\pi_{\text{GW+EM}}(\boldsymbol{\theta})d\boldsymbol{\theta}. \quad (4.5)$$

4.1.3.1 Relative binning likelihood technique

Relative binning (Zackay et al., 2018; Cornish, 2021; Krishna et al., 2023) is a method to accelerate the evaluation of the likelihood function presented in Eq. (2.9). This technique compares the waveform of an arbitrary parameter $\boldsymbol{\theta}$ to a reference waveform with parameter $\boldsymbol{\theta}_{\text{ref}}$. The ratio $r(f)$ between these waveforms is expressed as:

$$r(f) = \left| \frac{h(f; \boldsymbol{\theta})}{h(f; \boldsymbol{\theta}_{\text{ref}})} \right| e^{i[\arg(h(f; \boldsymbol{\theta})) - \arg(h(f; \boldsymbol{\theta}_{\text{ref}}))]} \quad (4.6)$$

This ratio can be approximated using piecewise linear functions across frequency bins:

$$r(f) \approx \begin{cases} r_0(b_1) + r_1(b_1)(f - f_m(b_1)), & f \in b_1 \\ r_0(b_2) + r_1(b_2)(f - f_m(b_2)), & f \in b_2 \\ \vdots \\ r_0(b_n) + r_1(b_n)(f - f_m(b_n)), & f \in b_n \end{cases} \quad (4.7)$$

Here, the frequency range is divided into bins $\{b_i\}$ with central frequencies $\{f_m(b_i)\}$. The accuracy of this approximation increases with the number of bins used. However, to optimize PE speed, the goal is to achieve sufficient accuracy with the minimum number of bins. The relative binning method is based on the assumption that the region of parameter space with significant likelihood overlaps with the area where waveforms differ only slightly from the best-fit waveform. This results in a smooth function $r(f)$ that can be well approximated with relatively few bins. Bin placement typically follows the approach outlined in Refs. (Zackay et al., 2018; Krishna et al., 2023).

4.2 Simulation study

This subsection describes the analysis of an EM afterglow of a GRB and the GW signal from a binary neutron star merger.

We consider a custom GRB afterglow model function that wraps around the tophat model within REDBACK¹ to include assumptions about jet energy and opening angle. This function is used to simulate the GRB afterglow over a specified time period with added noise, simulating observational data as shown in Figure 4.1. We set up a Gaussian likelihood for the simulated GRB afterglow model data and also priors for the EM model parameters, with some parameters fixed and others given uniform distributions.

In a similar manner, the GW signal is simulated using a binary neutron star IMRPhenomD_NRTidal waveform model, considering only one interferometer, i.e., LIGO Hanford, start-

¹<https://github.com/nikhil-sarin/redback>

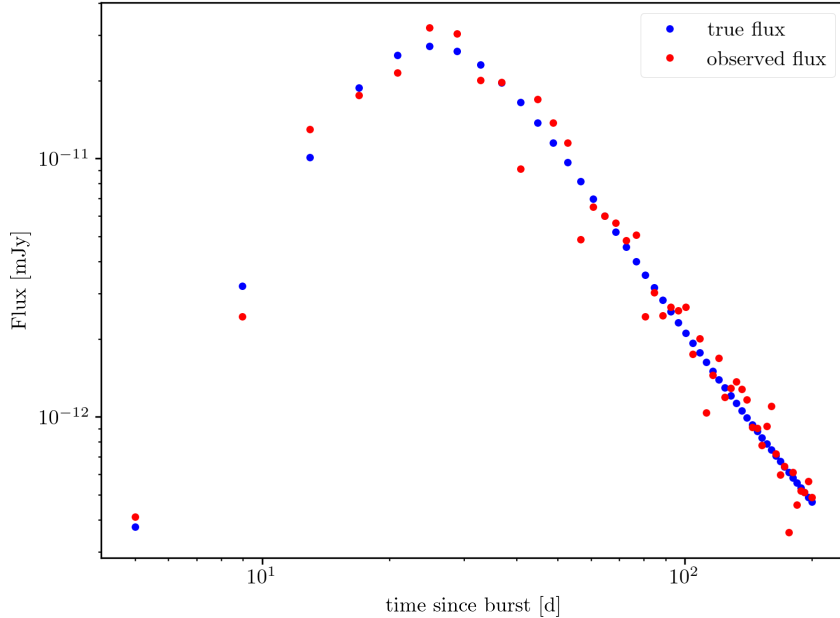


Figure 4.1: Simulated GRB afterglow lightcurve using the tophat model for a period of $\mathcal{O}(10^2)$ days.

ing at a frequency of 40 Hz. The GW signal is injected using `bilby` with a reference frequency of 50 Hz. The priors for the GW analysis are defined, with some parameters fixed and others following specific distributions. For instance, the individual masses m_1 and m_2 are sampled uniformly in the source frame. The chirp mass \mathcal{M} and mass ratio q are then derived from these sampled masses. The SNR of the GW signal is calculated to be 39.2, based on the assumed luminosity distance. The redshift is fixed in our analysis to break the known partial degeneracy between inclination angle and luminosity distance in GW observations. We also considered the spin and tidal deformation of colliding neutron stars. For more details on EM and GW priors, we refer to Table 4.2 along with the injected values. For parameters where no priors are provided, they are fixed in our analysis.

We then create a joint likelihood combining the EM and GW models. The joint inference is performed using the `dynesty` sampler within `bilby`, producing results for both the EM and GW components. The convergence of sampling is controlled by the number of

live points (n_{live}), and we used $n_{\text{live}} = 1000$. The stochastic sampling is parallelized with 8 processes for the simulation. The GW likelihood was computed using the relative binning algorithm for efficiency, as implemented in `bilby`. The results are shown with corner plots for the posterior distributions of the full parameters in Figure 4.4. In this work, we aimed to perform a joint GW-EM analysis by interfacing the EM and GW models. For more details on available transient EM models, we refer to [Sarin et al. \(2024\)](#).

Table 4.2: The injection and prior values for each parameter of the EM and GW signals are listed below. θ_{observer} and θ_{JN} are related and are treated as a single parameter.

Parameter	GW-only Injection	EM+GW Injection	Prior	Minimum	Maximum
$\log_{10} E_0$ [ergs]		51.653	Uniform	48	54
θ_{core} [Radian]		0.05	Uniform	0.01	0.05
$\log_{10} n_{\text{ism}}$ [cm^{-3}]		-1.301	Uniform	-6	0.3
p		2.5	Uniform	2	3
$\log_{10} \epsilon_e$		-3	Uniform	-5	0
$\log_{10} \epsilon_B$		-1.15	Uniform	-5	0
ξ_e		1	Delta	-	-
Γ_0		2000	Delta	-	-
θ_{observer} [Radian]		-	Uniform	0	0.8
θ_{JN} [Radian]	0.43	0.43	Uniform	0	0.8
d_L [Mpc]	43.4	43.4	Comoving	10	100
m_1 [M_{\odot}]	1.5	1.5	Constraint	0.5	5
m_2 [M_{\odot}]	1.3	1.3	Constraint	0.5	5
\mathcal{M} [M_{\odot}]	1.217	1.217	Gaussian	$\mu = 1.215$	$\sigma = 1$
q	0.867	0.867	Uniform	0.125	1
χ_1	0.02	0.02	Delta	-	-
χ_2	0.02	0.02	Delta	-	-
t_c [s]	1126259642.413	1126259642.413	Delta	-	-
ϕ_c [Radian]	1.3	1.3	Delta	-	-
RA [Radian]	1.375	1.375	Delta	-	-
DEC [Radian]	-1.2108	-1.2108	Delta	-	-
ψ [Radian]	2.659	2.659	Delta	-	-
Λ_1	400	400	Uniform	0	2000
Λ_2	450	450	Uniform	0	2000

4.3 Results & Conclusions

For our joint GW-EM analysis, we aimed to achieve two goals: (1) joint modeling with GW and GRB data to reduce computational costs, and (2) enhanced results due to multi-messenger signals. We were successful on both fronts. Figure 4.2 shows the inferred selected parameters of the BNS GW signal using only the GW data, while Figure 4.3 shows the same selected parameters inferred using both the GW and EM data. We observe improved results in the inferred parameters. Additionally, the tidal effects are probed more efficiently in higher frequency regimes. We will perform inference on $\tilde{\Lambda}$ instead of Λ_1 and Λ_2 . The improved results in θ_{observer} and d_L are clearly visible. For the full parameter inference with joint modeling, refer to Figure 4.4.

We direct the reader's attention to the implications of this work for performing analyses on joint datasets. Users can define their own model of interest and use the discussed framework to achieve improved results within a few hours, similar to the time taken in our joint analysis. Although the simulation studies performed here might not fully reflect realistic scenarios, we aim to conduct more realistic studies in the near future.

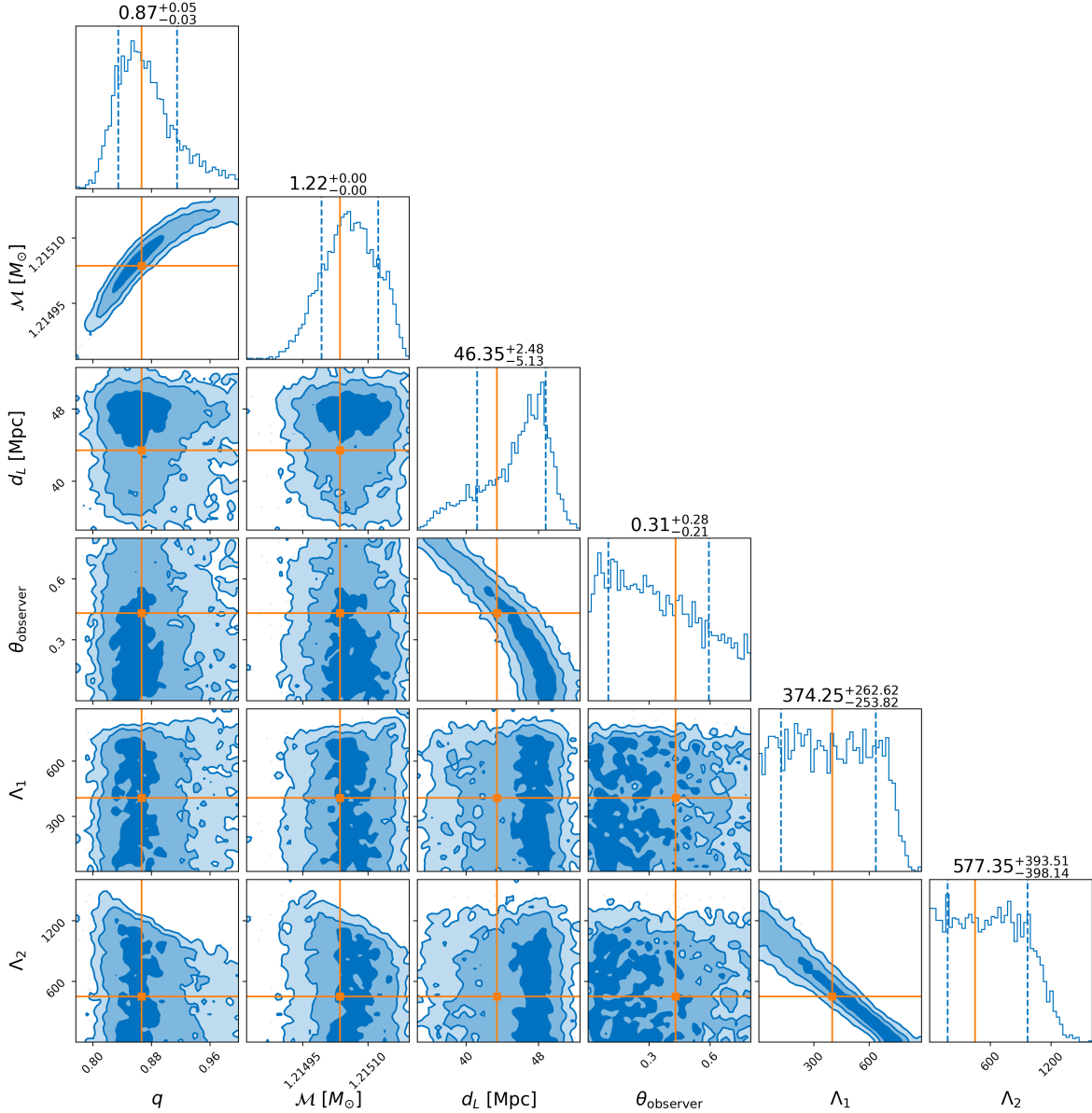
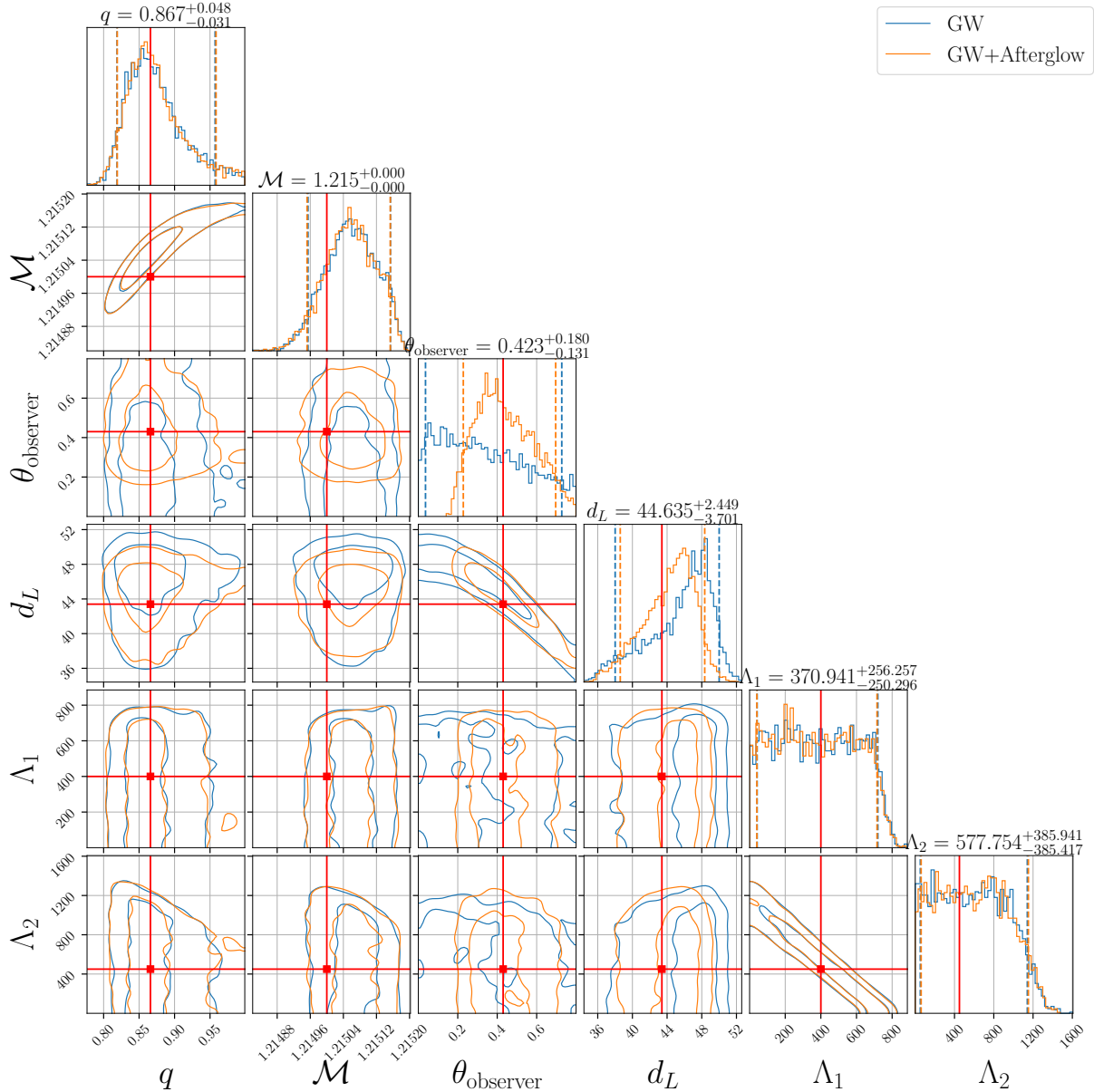


Figure 4.2: Corner plot showing one- and two-dimensional marginal posterior distributions of selected inferred parameters (q , \mathcal{M} , $\theta_{observer}$, d_L , Λ_1 , Λ_2) for the GW simulation using the relative binning technique. Diagonal panels show one-dimensional marginal posterior distributions, with vertical dashed blue lines indicating the 90% credible intervals. Off-diagonal panels show two-dimensional marginal posterior distributions, with solid blue contours indicating the 50% and 90% credible regions. Orange lines indicate the injection values. Above each diagonal plot, the median value and 90% credible interval for each parameter are displayed numerically.



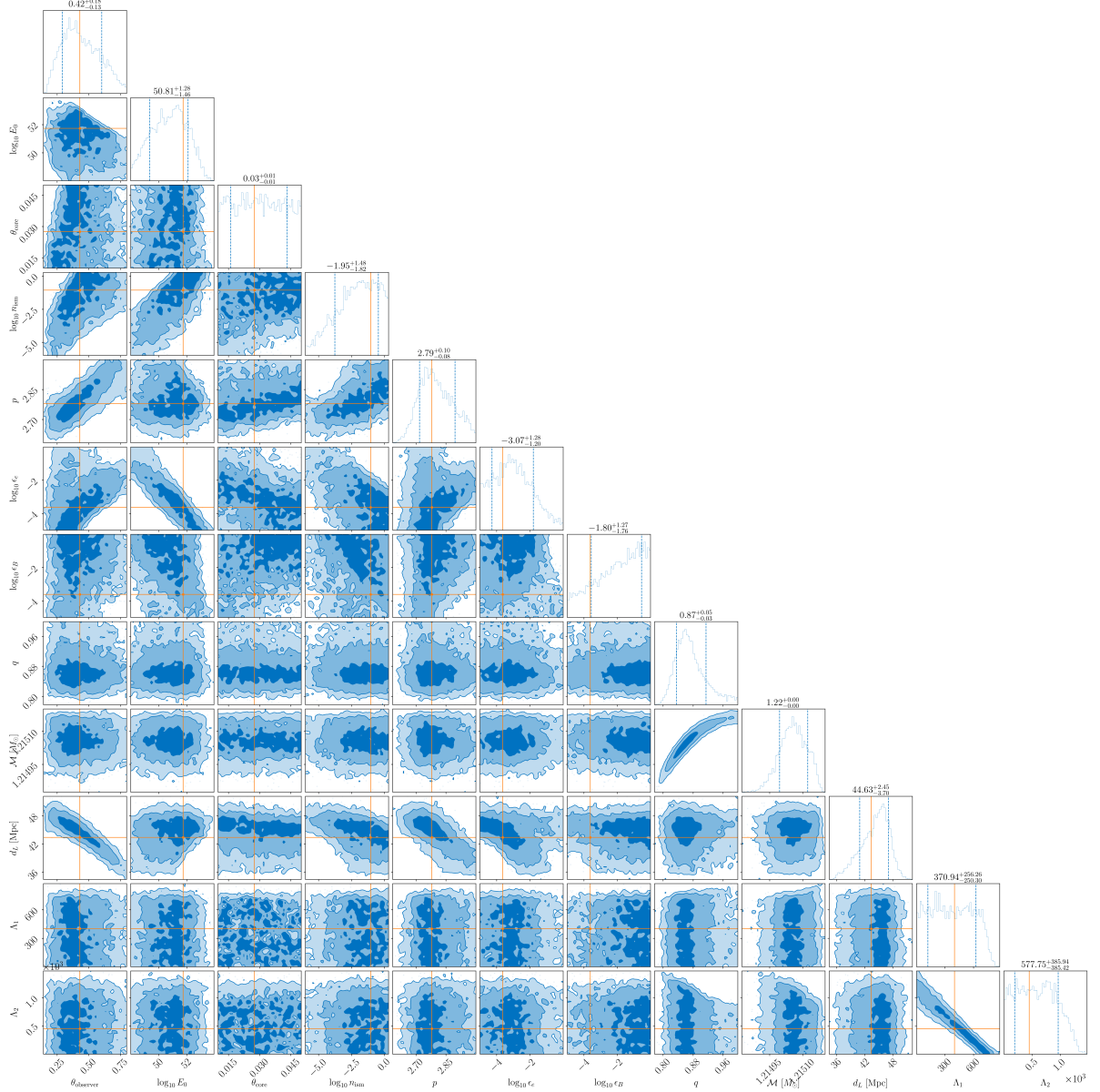


Figure 4.4: Corner plot showing one- and two-dimensional marginal posterior distributions of all inferred parameters for the GW-GRB afterglow simulation analyzed with the relative binning technique using combined GW and GRB data. Diagonal panels show one-dimensional marginal posterior distributions, with vertical dashed lines indicating the 90% credible intervals. Off-diagonal panels show two-dimensional marginal posterior distributions, with solid contours indicating the 50% and 90% credible regions. Orange lines indicate the injection values. For q and \mathcal{M} , orange lines are not shown since the simulations were performed using the values of the primary and secondary masses. Parameter labels are shown on the axes.

Chapter 5

Future Directions

The LVK Collaboration has already demonstrated the power of gravitational waves observations to learn about the coalescence of compact objects such as black holes and neutron stars. Gravitational-wave signals provide us with unique insights into cosmic events that are not accessible through electromagnetic observations alone. The LVK also discovered and extensively studied the first multimessenger source GW170817 observed in both gravitational waves and electromagnetic waves. Gravitational-wave observations have tested how compact binaries inspiral, merge, and settle down, capturing the dynamics through the phase evolution of the gravitational waveform. Gravitational waves have also been used to constrain strong-field gravity dynamics, providing information that is complementary to other measurements, such as those from pulsar binaries. In this dissertation, I have reported on improved techniques for testing general relativity, detecting multimessenger signals, and interpreting joint observations of GRB afterglows.

Still, there is much more to explore. We don't fully understand the population of GW sources, GRB sources, dense-matter physics, or GW emission from bursts and continuous sources. A larger number of multi-messenger events will greatly improve our understanding of such populations of GW and GRB sources, dense-matter physics, and the physical processes that give birth to energetic phenomena such as core-collapse supernovae, gamma-

ray bursts, and fast radio bursts.

In order to increase the frequency of either single or multi-messenger signal detections, we need to keep improving the detectors, analysis algorithms, refine our ranking statistics, and build fast inference techniques. Looking beyond this work, I am interested in pursuing the following two avenues.

5.1 Comprehensive O4 multi-messenger study with RAVEN

Continuing the work presented in Chapter 3, my collaborators and I are working on adding new instruments that report high-energy transients to the low-latency alert infrastructure. Additionally, we are in the process of generating simulation results to validate and improve on the ranking of low-significance GW and GRB candidates using their data products. As we outlined the performance of the RAVEN pipeline during O4a, there are a few issues that need to be addressed. We will continue this effort through the remainder of O4 and will be ready for the moment when nature gives us another GW-GRB event. Moreover, the improvements we are making will result in a robust multi-messenger search pipeline for future gravitational-wave observing runs.

5.2 Forward modeling of gravitational-wave observations

The death throes of massive stars, the collision of neutron-rich stars, or black-hole binaries in active galactic nuclei produce multi-messenger signals. The work I discussed in Chapter 4 marks the beginning of the joint modeling research avenue. In the future, I want to use these tools to seek a deeper understanding of the progenitors ([Abbott et al., 2017e](#)) and remnants ([DuPont & MacFadyen, 2024](#)) of multi-messenger sources.

Bibliography

- 2020, Data release for Tests of General Relativity with GWTC-2, <https://dcc.ligo.org/LIGO-P2000438/public>, doi:<https://doi.org/10.7935/903s-gx73>
- 2020, Gravitational Wave Open Science Center, GW190814, <https://www.gw-openscience.org/eventapi/html/GWTC-2/GW190814/v2>, doi:<https://doi.org/10.7935/zzw5-ak90>
- 2024, Probability of the Detection of BNS and NSBH Mergers in O4b, <https://emfollow.docs.ligo.org/userguide/capabilities.html#probability-of-the-detection-of-bns-and-nsbh-mergers-in-o4b>
- Aasi, J., et al. 2015, *Class. Quant. Grav.*, 32, 074001
- Abac, A. G., et al. 2024, arXiv:2404.04248
- Abbott, B., Abbott, R., Abbott, T., et al. 2019a, *Physical Review D*, 100, 104036
- Abbott, B. P., et al. 2016a, *Phys. Rev. Lett.*, 116, 061102
- . 2016b, *Phys. Rev. Lett.*, 116, 221101, [Erratum: *Phys.Rev.Lett.* 121, 129902 (2018)]
- . 2017a, *Nature*, 551, 85
- . 2017b, *Astrophys. J. Lett.*, 848, L13
- . 2017c, *Phys. Rev. Lett.*, 119, 161101
- . 2017d, *Astrophys. J. Lett.*, 848, L12
- . 2017e, *Astrophys. J. Lett.*, 850, L40
- . 2017f, *Annalen Phys.*, 529, 1600209
- . 2019b, *Phys. Rev. Lett.*, 123, 011102

- . 2019c, *Phys. Rev. D*, 100, 104036
- . 2020a, *Class. Quant. Grav.*, 37, 055002
- . 2020b, *Astrophys. J. Lett.*, 892, L3
- . 2021a, *Astrophys. J.*, 909, 218
- Abbott, R., et al. 2020c, *Astrophys. J. Lett.*, 896, L44
- . 2021b, *Astrophys. J. Lett.*, 915, L5
- . 2021c, *Phys. Rev. D*, 103, 122002
- . 2021d, arXiv:2112.06861
- . 2022, *Astrophys. J.*, 928, 186
- Acernese, F., et al. 2015, *Class. Quant. Grav.*, 32, 024001
- . 2019, *Phys. Rev. Lett.*, 123, 231108
- Adams, T., Buskulic, D., Germain, V., et al. 2016, *Class. Quant. Grav.*, 33, 175012
- Adhikari, N., & Morisaki, S. 2022, *Phys. Rev. D*, 106, 104053
- Agathos, M., Del Pozzo, W., Li, T. G. F., et al. 2014, *Phys. Rev. D*, 89, 082001
- Aghanim, N., et al. 2020, *Astron. Astrophys.*, 641, A6, [Erratum: *Astron. Astrophys.* 652, C4 (2021)]
- Agostini, M., et al. 2017, *Astrophys. J.*, 850, 21
- Ahumada, T., et al. 2021, *Nature Astron.*, 5, 917
- Ajith, P., et al. 2008, *Phys. Rev. D*, 77, 104017, [Erratum: *Phys. Rev. D* 79, 129901 (2009)]
- Allen, B., Anderson, W. G., Brady, P. R., Brown, D. A., & Creighton, J. D. 2012, *Physical Review D*, 85, 122006
- Antonioli, P., et al. 2004, *New J. Phys.*, 6, 114
- Arun, K. G., Iyer, B. R., Qusailah, M. S. S., & Sathyaprakash, B. S. 2006, *Phys. Rev. D*, 74, 024006
- Ashton, G., Burns, E., Dal Canton, T., et al. 2018, *The Astrophysical Journal*, 860, 6
- Ashton, G., et al. 2019, *Astrophys. J. Suppl.*, 241, 27
- Atteia, J. L., Cordier, B., & Wei, J. 2023, in 16th Marcel Grossmann Meeting on Recent

Developments in Theoretical and Experimental General Relativity, Astrophysics and Relativistic Field Theories

- Aubin, F., et al. 2021, *Class. Quant. Grav.*, 38, 095004
- Banagiri, S., Berry, C. P. L., Cabourn Davies, G. S., Tsukada, L., & Doctor, Z. 2023, *Phys. Rev. D*, 108, 083043
- Barthelmy, S. D., et al. 2005, *Space Sci. Rev.*, 120, 143
- Bartos, I., Veske, D., Keivani, A., et al. 2019, *Phys. Rev. D*, 100, 083017
- Berbel, M., Miravet-Tenés, M., Chaudhary, S. S., et al. 2024, *Class. Quant. Grav.*, 41, 085012
- Bhattacharjee, S., Banerjee, S., Bhalerao, V., et al. 2024, *Mon. Not. Roy. Astron. Soc.*, 528, 4255
- Biscoveanu, S., Thrane, E., & Vitale, S. 2020, *Astrophys. J.*, 893, 38
- Blanchet, L. 2014, *Living Rev. Rel.*, 17, 2
- Blanchet, L., & Sathyaprakash, B. S. 1995, *Phys. Rev. Lett.*, 74, 1067
- Bloom, J. S., et al. 2002, *Astrophys. J. Lett.*, 572, L45
- Buikema, A., et al. 2020, *Phys. Rev. D*, 102, 062003
- Buonanno, A., Iyer, B., Ochsner, E., Pan, Y., & Sathyaprakash, B. S. 2009, *Phys. Rev. D*, 80, 084043
- Burns, E. 2020, *Living Rev. Rel.*, 23, 4
- Burns, E., et al. 2023, *Astrophys. J. Lett.*, 946, L31
- Buskulic, D. 2010, *Class. Quant. Grav.*, 27, 194013
- Canizares, P., Field, S. E., Gair, J., et al. 2015, *Phys. Rev. Lett.*, 114, 071104
- Cannon, K., et al. 2012, *Astrophys. J.*, 748, 136
- Cano, Z., Wang, S.-Q., Dai, Z.-G., & Wu, X.-F. 2017, *Adv. Astron.*, 2017, 8929054
- Carroll, B. W., & Ostlie, D. A. 2017, *An introduction to modern astrophysics* (Cambridge University Press)
- Chatterjee, D., Ghosh, S., Brady, P. R., et al. 2020, *Astrophys. J.*, 896, 54

Chaudhary, S. S., et al. 2024, *Proc. Nat. Acad. Sci.*, 121, e2316474121

Cho, M.-A. 2019, PhD thesis, University of Maryland, College Park

Chornock, R., et al. 2017, *Astrophys. J. Lett.*, 848, L19

Christensen, N., & Meyer, R. 2022, *Rev. Mod. Phys.*, 94, 025001

Chu, Q., et al. 2022, *Phys. Rev. D*, 105, 024023

Coleman Miller, M., & Yunes, N. 2021, *Gravitational Waves in Physics and Astrophysics* (IOP)

Collaboration, L. S., Collaboration, V., et al. 2017, *GRB Coordinates Network*, 21509, 1

Connaughton, V., Blackburn, L., Briggs, M., et al. 2017, *GRB Coordinates Network*, 21506, 1

Cornish, N. J. 2021, *Phys. Rev. D*, 104, 104054

Corsi, A., Barsotti, L., Berti, E., et al. 2024, *Frontiers in Astronomy and Space Sciences*, 11, 1386748

Costa, E., et al. 1997, *Nature*, 387, 783

Coughlin, M. W., Dietrich, T., Margalit, B., & Metzger, B. D. 2019, *Mon. Not. Roy. Astron. Soc.*, 489, L91

Creighton, J. D. E., & Anderson, W. G. 2011, *Gravitational-wave physics and astronomy: An introduction to theory, experiment and data analysis* (John Wiley & Sons)

Cutler, C., & Flanagan, E. E. 1994, *Phys. Rev. D*, 49, 2658

Dal Canton, T., Nitz, A. H., Gadre, B., et al. 2021, *Astrophys. J.*, 923, 254

Dhurkunde, R., & Nitz, A. H. 2023, *arXiv:2311.00242*

Dimple, Misra, K., & Arun, K. G. 2023, *Astrophys. J. Lett.*, 949, L22

Drago, M., et al. 2021, *SoftwareX*, 14, 100678

DuPont, M., & MacFadyen, A. 2024, *arXiv:2405.20329*

Eardley, D. M. 1975, *The Astrophysical Journal*, 196, L59

Einstein, A. 1915, *Sitzungsber. Preuss. Akad. Wiss. Berlin (Math. Phys.)*, 1915, 844

—. 1916, *Sitzungsber. Preuss. Akad. Wiss. Berlin (Math. Phys.)*, 1916, 1

—. 1918, *Sitzungsber. Preuss. Akad. Wiss. Berlin*, 154, 1918

Essick, R. 2023, *Phys. Rev. D*, 108, 043011

Ewing, B., et al. 2024, *Phys. Rev. D*, 109, 042008

Fan, X., Messenger, C., & Heng, I. S. 2014, *Astrophys. J.*, 795, 43

Farah, A., Essick, R., Doctor, Z., Fishbach, M., & Holz, D. E. 2020, *The Astrophysical Journal*, 895, 108

Fernández, R., Kasen, D., Metzger, B. D., & Quataert, E. 2015, *Mon. Not. Roy. Astron. Soc.*, 446, 750

Finn, L. S. 1997, in 2nd Edoardo Amaldi Conference on Gravitational Waves, 180–191

Fong, H. K. Y. 2018, PhD thesis, Toronto U.

Friedman, J. L., & Stergioulas, N. 2020, *International Journal of Modern Physics D*, 29, 2041015

Fruchter, A. S., et al. 2006, *Nature*, 441, 463

Garcia-Cifuentes, K., Becerra, R. L., De Colle, F., & Vargas, F. 2024, *Monthly Notices of the Royal Astronomical Society*, 527, 6752

Ghodla, S. 2024, *Mon. Not. Roy. Astron. Soc.*, 532, 439

Gianfagna, G., Piro, L., Pannarale, F., et al. 2023, *Mon. Not. Roy. Astron. Soc.*, 523, 4771

Goldstein, A., et al. 2017a, *Astrophys. J. Lett.*, 848, L14

Goldstein, A. e., Veres, P., von Kienlin, A., et al. 2017b, *GRB Coordinates Network*, 21528, 1

Gompertz, B. P., et al. 2023, *Nature Astron.*, 7, 67

Graur, O. 2022, *Supernova* (MIT Press)

Hallinan, G., et al. 2017, *Science*, 358, 1579

Hastings, W. K. 1970, *Biometrika*, 57, 97

Howell, E., Ackley, K., Rowlinson, A., & Coward, D. 2019, *Monthly Notices of the Royal Astronomical Society*, 485, 1435

Husa, S., Khan, S., Hannam, M., et al. 2016, *Phys. Rev. D*, 93, 044006

- Isi, M., Giesler, M., Farr, W. M., Scheel, M. A., & Teukolsky, S. A. 2019, *Phys. Rev. Lett.*, 123, 111102
- Jaranowski, P., & Krolak, A. 2009, *Analysis of gravitational-wave data* (Cambridge: Cambridge Univ. Press), doi:10.1017/CBO9780511605482
- Kapadia, S. J., et al. 2020, *Class. Quant. Grav.*, 37, 045007
- Karakas, B., Matur, R., & Ruffert, M. 2024, arXiv:2405.13687
- Kasen, D., Metzger, B., Barnes, J., Quataert, E., & Ramirez-Ruiz, E. 2017, *Nature*, 551, 80
- Khan, S., Chatziioannou, K., Hannam, M., & Ohme, F. 2019, *Phys. Rev. D*, 100, 024059
- Khan, S., Husa, S., Hannam, M., et al. 2016, *Phys. Rev. D*, 93, 044007
- Khan, S., Ohme, F., Chatziioannou, K., & Hannam, M. 2020, *Phys. Rev. D*, 101, 024056
- Klimenko, S., Yakushin, I., Mercer, A., & Mitselmakher, G. 2008, *Class. Quant. Grav.*, 25, 114029
- Klimenko, S., et al. 2016, *Phys. Rev. D*, 93, 042004
- Kochanek, C. S., & Piran, T. 1993, *Astrophys. J. Lett.*, 417, L17
- Kouveliotou, C., Meegan, C. A., Fishman, G. J., et al. 1993, *Astrophys. J. Lett.*, 413, L101
- Krishna, K., Vijaykumar, A., Ganguly, A., et al. 2023, arXiv:2312.06009
- Kumar, P., & Zhang, B. 2014, *Phys. Rept.*, 561, 1
- Lamb, G. P., & Kobayashi, S. 2018, *Mon. Not. Roy. Astron. Soc.*, 478, 733
- Lazzati, D., Perna, R., Morsony, B. J., et al. 2018, *Phys. Rev. Lett.*, 120, 241103
- Levan, A. 2018, *Gamma-ray bursts* (IoP Publishing)
- Levan, A. J., et al. 2024, *Nature*, 626, 737
- Li, T. G. F., Del Pozzo, W., Vitale, S., et al. 2012, *Phys. Rev. D*, 85, 082003
- Lien, A., et al. 2016, *Astrophys. J.*, 829, 7
- LIGO Scientific Collaboration. 2018, *LIGO Algorithm Library - LALSuite*, free software (GPL), doi:10.7935/GT1W-FZ16
- Lyman, J. D., et al. 2018, *Nature Astron.*, 2, 751

- Maggiore, M. 2007, *Gravitational Waves. Vol. 1: Theory and Experiments*, Oxford Master Series in Physics (Oxford University Press)
- . 2018, *Gravitational Waves. Vol. 2: Astrophysics and Cosmology* (Oxford University Press)
- Mapelli, M. 2020, *Frontiers in Astronomy and Space Sciences*, 7, 38
- Margalit, B., Jermyn, A. S., Metzger, B. D., Roberts, L. F., & Quataert, E. 2022, *Astrophys. J.*, 939, 51
- Margalit, B., & Metzger, B. D. 2017, *Astrophys. J. Lett.*, 850, L19
- Marion, F. 2003, in *Rencontres de Moriond Gravitational Waves and Experimental Gravity*, ed. T. T. V. J. Dumarchez J., Moriond Workshops (Les Arcs, France: The GIOI publishers), 145–150
- Meegan, C., et al. 2009, *Astrophys. J.*, 702, 791
- Meegan, C. A., Fishman, G. J., Wilson, R. B., et al. 1992, *Nature*, 355, 143
- Messick, C., et al. 2017, *Phys. Rev. D*, 95, 042001
- Mészáros, P. 2019, *Mem. Soc. Ast. It.*, 90, 57
- Metropolis, N., Rosenbluth, A., Rosenbluth, M., Teller, A., & Teller, E. 1953, *J. Chem. Phys.*, 21, 1087
- Mishra, C. K., Arun, K. G., Iyer, B. R., & Sathyaprakash, B. S. 2010, *Phys. Rev. D*, 82, 064010
- Misner, C. W., Thorne, K. S., & Wheeler, J. A. 1973, *Gravitation* (Macmillan)
- Morisaki, S. 2021, *Phys. Rev. D*, 104, 044062
- Morisaki, S., & Raymond, V. 2020, *Phys. Rev. D*, 102, 104020
- Moroianu, A., Wen, L., James, C. W., et al. 2023, *Nature Astron.*, 7, 579
- Narayan, R., Paczynski, B., & Piran, T. 1992, *Astrophys. J. Lett.*, 395, L83
- Nitz, A. H., Nielsen, A. B., & Capano, C. D. 2019, *Astrophys. J. Lett.*, 876, L4
- O’Shaughnessy, R., Farr, B., Ochsner, E., et al. 2014, *Phys. Rev. D*, 89, 064048
- O’Connor, B., et al. 2023, *Sci. Adv.*, 9, adi1405

Perkins, S., & Yunes, N. 2022, *Phys. Rev. D*, 105, 124047

Pian, E., et al. 2017, *Nature*, 551, 67

Pillas, M. 2023, PhD thesis, Laboratoire de Physique des 2 Infinis Irène Joliot-Curie, France

Pillas, M., Dal Canton, T., Stachie, C., et al. 2023, *Astrophys. J.*, 956, 56

Piotrkowski, B., Baylor, A., & Hernandez, I. M. 2022, *Class. Quant. Grav.*, 39, 085010

Piotrkowski, B. J. 2022, PhD thesis, University of Wisconsin-Milwaukee

Piran, T. 2004, *Rev. Mod. Phys.*, 76, 1143

Poisson, E., & Will, C. M. 1995, *Phys. Rev. D*, 52, 848

Radice, D., Perego, A., Zappa, F., & Bernuzzi, S. 2018, *Astrophys. J. Lett.*, 852, L29

Ray, A., Camilo, M., Creighton, J., Ghosh, S., & Morisaki, S. 2023, *Phys. Rev. D*, 107, 043035

Rees, M. J., & Meszaros, P. 1994, *Astrophys. J. Lett.*, 430, L93

Rhodes, L., van der Horst, A., Fender, R., et al. 2020, *Monthly Notices of the Royal Astronomical Society*, 496, 3326

Robinet, F., Arnaud, N., Leroy, N., et al. 2020, *SoftwareX*, 12, 100620

Romero-Shaw, I. M., et al. 2020, *Mon. Not. Roy. Astron. Soc.*, 499, 3295

Ronchini, S., Branchesi, M., Oganessian, G., et al. 2022, *Astronomy & Astrophysics*, 665, A97

Ronchini, S., et al. 2024, *Astrophys. J. Lett.*, 970, L20

Rossi, A., et al. 2022, *Astrophys. J.*, 932, 1

Rosswog, S., Diener, P., Torsello, F., Tauris, T. M., & Sarin, N. 2024, *Mon. Not. Roy. Astron. Soc.*, 530, 2336

Ruiz, M., Shapiro, S. L., & Tsokaros, A. 2018, *Phys. Rev. D*, 98, 123017

Ryan, G., Van Eerten, H., Piro, L., & Troja, E. 2020, *The Astrophysical Journal*, 896, 166

Sachdev, S., et al. 2019, arXiv:1901.08580

Saleem, M., Datta, S., Arun, K. G., & Sathyaprakash, B. S. 2022, *Phys. Rev. D*, 105, 084062

Sampson, L., Cornish, N., & Yunes, N. 2013, *Phys. Rev. D*, 87, 102001

Santamaria, L., et al. 2010, *Phys. Rev. D*, 82, 064016

Sari, R., Piran, T., & Narayan, R. 1998, *Astrophys. J. Lett.*, 497, L17

Sarin, N., & Lasky, P. D. 2021, *Gen. Rel. Grav.*, 53, 59

Sarin, N., Hübner, M., Omand, C. M., et al. 2024, *Mon. Not. Roy. Astron. Soc.*, 531, 1203

Sathyaprakash, B. S., & Dhurandhar, S. V. 1991, *Phys. Rev. D*, 44, 3819

Savchenko, V., et al. 2017a, *Astrophys. J. Lett.*, 848, L15

Savchenko, V., Mereghetti, S., Ferrigno, C., et al. 2017b, *GRB Coordinates Network*, 21507, 1

Schaffner-Bielich, J. 2020, *Compact star physics* (Cambridge University Press)

Schutz, B. 2022, *A first course in general relativity* (Cambridge university press)

Shah, V. G., Narayan, G., Perkins, H. M. L., et al. 2024, *Mon. Not. Roy. Astron. Soc.*, 528, 1109

Shoom, A. A., Gupta, P. K., Krishnan, B., Nielsen, A. B., & Capano, C. D. 2023, *Gen. Rel. Grav.*, 55, 55

Singer, L. P., & Price, L. R. 2016, *Phys. Rev. D*, 93, 024013

Skilling, J. 2006, *Bayesian Anal.*, 1, 833

Smith, R., Field, S. E., Blackburn, K., et al. 2016, *Phys. Rev. D*, 94, 044031

Speagle, J. S. 2020, *Mon. Not. Roy. Astron. Soc.*, 493, 3132

Stachie, C., et al. 2020, *Class. Quant. Grav.*, 37, 175001

Svinkin, D., Hurley, K., von Kienlin, A., et al. 2017, *GRB Coordinates Network*, 21515, 1

Takeda, H., Morisaki, S., & Nishizawa, A. 2021, *Phys. Rev. D*, 103, 064037

Tauris, T. M., & van den Heuvel, E. P. J. 2023, *Physics of Binary Star Evolution: From Stars to X-ray Binaries and Gravitational Wave Sources*, Princeton Series in Astrophysics (Princeton University Press), doi:10.1515/9780691239262

Tavani, M., et al. 2009, *Astron. Astrophys.*, 502, 995

Thrane, E., & Talbot, C. 2019, *Publ. Astron. Soc. Austral.*, 36, e010, [Erratum:

- Publ.Astron.Soc.Austral. 37, e036 (2020)]
- Timmes, F., Woosley, S., & Weaver, T. A. 1995, arXiv preprint astro-ph/9510136
- Totani, T. 2013, Pub. Astron. Soc. Jpn., 65, L12
- Troja, E., et al. 2022, Nature, 612, 228
- Tse, M., et al. 2019, Phys. Rev. Lett., 123, 231107
- Urban, A. L. 2016, PhD thesis, University of Wisconsin-Milwaukee
- Usman, S. A., et al. 2016, Class. Quant. Grav., 33, 215004
- Van Den Broeck, C., & Sengupta, A. S. 2007a, Class. Quant. Grav., 24, 1089
- . 2007b, Class. Quant. Grav., 24, 155
- Veitch, J., et al. 2015, Phys. Rev. D, 91, 042003
- Veske, D., Márka, Z., Bartos, I., & Márka, S. 2021, Astrophys. J., 908, 216
- Vinciguerra, S., Veitch, J., & Mandel, I. 2017, Class. Quant. Grav., 34, 115006
- von Kienlin, A., et al. 2020, Astrophys. J., 893, 46
- Wang, Y.-Y., Tang, S.-P., Jin, Z.-P., & Fan, Y.-Z. 2023, The Astrophysical Journal, 943, 13
- Watson, D., et al. 2019, Nature, 574, 497
- Will, C. M. 2011, Proc. Nat. Acad. Sci., 108, 5938
- . 2014, Living Rev. Rel., 17, 4
- Winkler, C., et al. 2003, Astron. Astrophys., 411, L1
- Wu, Y., & MacFadyen, A. 2019, Astrophys. J. Lett., 880, L23
- Yunes, N., Miller, M. C., & Yagi, K. 2022, Nature Rev. Phys., 4, 237
- Yunes, N., & Pretorius, F. 2009, Phys. Rev. D, 80, 122003
- Yunes, N., Yagi, K., & Pretorius, F. 2016, Phys. Rev. D, 94, 084002
- Zackay, B., Dai, L., & Venumadhav, T. 2018, arXiv:1806.08792
- Zhang, B. 2018, The physics of gamma-ray bursts (Cambridge University Press)
- . 2019, Front. Phys. (Beijing), 14, 64402
- Zheng, Y., Cavaglià, M., Quitzow-James, R., & Mogushi, K. 2021, Significance, 18

Naresh Adhikari

Department of Physics, University of Wisconsin-Milwaukee, P.O. Box 413, Milwaukee WI, 53201

✉ naresh@uwm.edu

Education

Ph.D. in Physics , University of Wisconsin-Milwaukee, Wisconsin, USA	<i>August 2024</i>
Advisor: Professor Patrick Brady	
Master of Science in Physics , Bowling Green State University, Ohio, USA	<i>August 2019</i>
Master of Science in Physics , Tribhuvan University, Kirtipur, Nepal	<i>July 2017</i>
Bachelor of Science in Physics , Tribhuvan University, Kirtipur, Nepal	<i>December 2012</i>

Research Experience

Research Assistant, University of Wisconsin-Milwaukee, Milwaukee, Wisconsin *06/20 - 08/24*

- Developed and tested a rapid analysis technique for parametrized tests of General Relativity using Gravitational Waves (GW); published as first author in a peer-reviewed journal.
- Tested and deployed a low-latency multi-messenger search pipeline combining Gravitational-Wave and Gamma-Ray Burst (GRB) events; incorporated feature enhancements to rank joint candidates within one minute; manuscript in preparation.
- Developed and tested a joint inference algorithm for GW and GRB datasets; contributed to an open-source Python package and published as contributing author on an article.

Graduate Student, Bowling Green State University, Bowling Green, Ohio *01/18 - 07/19*

- Executed and analyzed experimental studies in wide bandgap semiconductor physics, correlating them with optical, transport, and defect studies, resulting in the publication of two journal papers under the supervision of Professor Farida Selim.
- 1+ year of experience in positron annihilation spectroscopy data analysis.

Graduate Student, Tribhuvan University, Kirtipur, Kathmandu *01/17 - 07/17*

- Defended an independent research project for the master's thesis, titled 'A Study of Linear Perturbations of the Schwarzschild Black Hole,' under the supervision of Professor Udayaraj Khanal.

Work Experience

Teaching Assistant, University of Wisconsin-Milwaukee, Milwaukee, Wisconsin *08/19 - 12/23*

Teaching Assistant, Bowling Green State University, Bowling Green, Ohio *08/17 - 05/19*

Technical Skills

Computer:

Python, LaTeX, Linux/Unix, HTCondor, Git, Flask, Celery, Mathematica, Origin, Fortran, C/C++, CUDA, Sentry, Flower, TensorFlow, scikit-learn.

Project: Bilby, bilby-tgr, ligo-raven, GWCelery, REDBACK

Laboratory:

Spectroscopy: Positron Annihilation Lifetime, Digital Coincidence Doppler Broadening, UV-Visual, Thermoluminescence; Hall Effect, Annealing

Certifications: Issued by NVIDIA Deep Learning Institute:

Fundamentals of Deep Learning (Feb 2022),

Fundamentals of Accelerated Computing with CUDA C/C++ (Mar 2022),

Fundamentals of Accelerated Data Science with RAPIDS (Jun 2022)

Honors and Awards

Chancellor’s Graduate Success Fund (UW-Milwaukee)	<i>Fall 2022</i>
Physics Fellowship (UW-Milwaukee)	<i>Spring 2022</i>
Research Excellence Award in Physics (UW-Milwaukee)	<i>Spring 2020 - Spring 2024</i>
Chancellor’s Graduate Student Award in Physics (UW-Milwaukee)	<i>Fall 2019 - Fall 2023</i>
J. Robert and Gretchen Overman Scholarship (BGSU)	<i>Summer 2019</i>
Helen and Barney Wood Scholarship (BGSU)	<i>Fall 2018-Spring 2019</i>
B.P. Koirala Memorial Award for Master’s Thesis (Ministry of Education, Science & Technology, Nepal)	<i>Spring 2017</i>

Publications

First and short author publications

1. Ronchini, S., Bala, S., Wood, J., et al., “Constraining possible γ -ray burst emission from GW230529 using Swift-BAT and Fermi-GBM,” *The Astrophysical Journal Letters*, 970(1), L20 (2024).
2. Sarin, N., Hübner, M., Omand, C., et al., “Redback: A Bayesian inference software package for electromagnetic transients,” *Monthly Notices of the Royal Astronomical Society*, 531(1), 1203-1227 (2024).
3. Chaudhary, S. S., Toivonen, A., Waratkar, G., et al., “Low-latency gravitational wave alert products and their performance in anticipation of the fourth LIGO-Virgo-KAGRA observing run,” *Proceedings of the National Academy of Sciences*, 121(18), e2316474121 (2024).
4. **Adhikari, N.**, & Morisaki, S., “Accelerating gravitational-wave parametrized tests of general relativity using a multiband decomposition of likelihood,” *Physical Review D*, 106(10), 104053 (2022).
5. Rana, D., Agarwal, S., Islam, M., et al., “Light-driven permanent transition from insulator to conductor,” *Physical Review B*, 104(24), 245208 (2021).
6. Islam, M. M., **Adhikari, N.**, Hernandez, A., et al., “Direct measurement of the density and energy level of compensating acceptors and their impact on the conductivity of n-type Ga₂O₃ films,” *Journal of Applied Physics*, 127(14), 145701 (2020).

Contributing

1. Raman, Gayathri, et al. “Swift-BAT GUANO follow-up of gravitational-wave triggers in the third LIGO-Virgo-KAGRA observing run.” arXiv preprint arXiv:2407.12867 (2024).
2. Abbott, R., et al. “Search for gravitational waves associated with fast radio bursts detected by CHIME/FRB during the LIGO–Virgo observing run O3b.” Manuscript under internal review.

Presentations

Enabling Multi-Messenger Astronomy through Low-Latency GW-GRB Coincidence Ranking, February 2024, Nevada Center for Astrophysics Symposium, University of Nevada Las Vegas, USA
Enabling Multi-Messenger Astronomy through Low-Latency GW-GRB Coincidence Ranking and Inference, November 2023, 33rd Midwest Relativity Meeting, University of Chicago, Chicago, USA

RAVEN: LIGO-Virgo-KAGRA gravitational wave focused multi-messenger pipeline, July 2023, EMIT School in Multi-messenger Astronomy, Vanderbilt University, Nashville, USA

RAVEN: LIGO-Virgo-KAGRA gravitational wave focused multi-messenger pipeline, April 2023, APS April 2023 Meeting, Minneapolis, Minnesota, USA

Accelerating gravitational-wave parameterized tests of General Relativity using a multiband decomposition of likelihood, September 2022, Poster presentation (online), LIGO-Virgo-KAGRA collaboration Meeting, Cardiff University, UK

Rapid tests of general relativity with gravitational waves using multi banding, November 2021, 31st Midwest Relativity Meeting, University of Illinois, Urbana-Champaign, USA

Correlation between native defects, conductivity, and green luminescence in ZnO single

crystals, August 2018, 18th International Conference in Positron Annihilation, Orlando, USA
Annual Spring Meeting of the APS Ohio-Region Section and the AAPT Michigan Section,
March 2018, Michigan, USA

Activities and Interests

Milwaukee Astronomical Society, 2022 - Present

American Physical Society, Association of Nepali Physicists in America, 2017 - Present

Supervision

Master students: Rabina Kadariya, Santosh Bhandari, Patan Multiple Campus, Tribhuvan University, Nepal *Jul 2021 - Feb 2022*

Undergraduate students:

Sagar Chaudhary (Oklahoma State University, Fall 2024), Bibek Lal Karn (University of Mississippi, Fall 2024), Sudip Chaudhary, Trichandra Campus, Tribhuvan University, Nepal *Jul 2021 - Jul 2022*

Community Involvement

Organizer, Physics Journal Club and Seminar Coordination, Milwaukee, WI *09/23 - 02/24*

Member, Coffeeshop Astrophysics Group, Milwaukee, WI *02/20 - 02/21*

Subject Expert, Nicolet Science and Engineering Fair, Glendale, WI *02/20 - 02/20*

Volunteer, Maker Faire Milwaukee, Milwaukee, WI *09/19 - 09/19*

Volunteer, Northwest Ohio Science Olympiad, Bowling Green, OH *03/19 - 03/19*

Group Leader, Cross-Cultural Conversation Connection, Bowling Green, OH *01/18 - 05/18*

Leadership Experience

Further details of this contribution are documented at <https://laac.docs.ligo.org/rewards/>.

Alternative Metrics

During the LIGO-Virgo-KAGRA's fourth observing run, issued multiple update alerts in role as a low-latency parameter estimation expert liaison.

GCN Circular 34770

GCN Circular 34761

GCN Circular 34746

GCN Circular 34745

GCN Circular 34270